Internal Report
DESY F35D-94-04
Univ. of Iowa 94-009
May 1994

A Measurement of the Proton Structure Function and a First Determination of the Gluon Distribution with the ZEUS Detector at HERA

by

Maria Teresa P. Roco

A MEASUREMENT OF THE PROTON STRUCTURE FUNCTION AND A FIRST DETERMINATION OF THE GLUON DISTRIBUTION WITH THE ZEUS DETECTOR AT HERA

by

Maria Teresa P. Roco

ABSTRACT

The first electron-proton collider at HERA opens a new domain where deep inelastic scattering off proton constituents carrying a small fraction x of the proton momentum can be studied. In 1992 HERA provided collisions between 26.7 *GeV* electrons and 820 *GeV* protons resulting in a center of mass energy of 296 *GeV*. This new energy range allows the measurement of the proton structure in a previously unexplored kinematic region down to $x \sim 10^{-4}$. The methods and results of an independent measurement of the proton structure function F_2 at low x and a first determination of the gluon distribution are presented. The results show a steeply rising F_2 towards smaller values of x. A strong rise in the density of the gluons is also observed with decreasing x. At fixed values of x, the dependence of F_2 on the square of the momentum transfer are observed to be in accord with QCD expectations.

A MEASUREMENT OF THE PROTON STRUCTURE FUNCTION AND
A FIRST DETERMINATION OF THE GLUON DISTRIBUTION
WITH THE ZEUS DETECTOR AT HERA

by

Maria Teresa P. Roco

University of Iowa

ACKNOWLEDGEMENTS

There are quite a number of people who helped me get to this point in my life. I would like to take this opportunity to express my gratitude to all of them. I am very grateful to Dr. Usha Mallik for her guidance and support through these years. She has made it possible for me to participate in the calorimeter testbeam effort at Fermilab and then later to join the ZEUS experiment at DESY. More importantly, she has greatly influenced me to become a responsible and mature person. She has been a good adviser and a good friend.

Special thanks go to Dr. Allen Caldwell and Dr. Halina Abramowicz. Working with both of them has been an inspiring and enjoyable learning experience.

I would also like to thank Richard Talaga for his support and advice for the period when things were not going so well. I would also like to thank Tim Dubbs.

Thanks to my fellow Iowa students Song-Ming Wang and Jiatai Wu. Thanks to Minzu Wang for reading this thesis and for his helpful comments and suggestions. Thanks to Tim Bienz and Dr. Edward McCliment for giving me good advise when I needed it.

I am most grateful to my parents who have always been kind, patient, loving and understanding. They have always been encouraging and supportive. Thanks to my sisters Dingky, Bubbie, Baby and my brother Dongky - I wish them all the best.

And last but not least, I would like give special thanks to Frank Chlebana for his patience, support, understanding, and great sense of humor. He has made these last (stressful) years the best years of my life.

TABLE OF CONTENTS

LIST OF TABLES

LIST OF FIGURES

CHAPTER 1

INTRODUCTION

Deep inelastic lepton-nucleon scattering has played an important role in our present understanding of the structure of matter. Early fixed target experiments [1] have established the partonic structure of the nucleon and contributed to the development of Quantum Chromodynamics (QCD), the theory that describes the strong interactions of quarks and gluons collectively known as partons. The first electron-proton collider HERA [2] opens a new domain where deep inelastic scattering off proton constituents carrying a small momentum fraction x can be studied. In 1992 HERA provided collisions between 26.7 *GeV* electrons and 820 *GeV* protons resulting in a center of mass energy of 296 *GeV*. This new energy range allowed the two experiments H1 [3] and ZEUS [4] to probe the proton structure down to $x \sim 10^{-4}$, which is two orders of magnitude smaller than previously measured in fixed target experiments.

Deep inelastic scattering in the small x region has been the focus of much theoretical interest. In this yet unexplored kinematic region, the model of quasi-free noninteracting partons leads to steeply rising structure functions due to the rapidly growing densities of gluons and sea quarks in the nucleon as $x \to 0$. If the quark and gluon densities become so large that the partons have significant spatial overlap, the partons inside the nucleon can no longer be treated as noninteracting. The parton model is no longer valid and several new physical phenomena are then expected to occur. Parton interactions within the nucleon including scattering and recombination have to be taken into account. Such interactions would lead to a saturation of the quark and gluon densities, which would be observed as a plateau in the nucleon structure function at small x.

This thesis presents a measurement of the proton structure function F_2 at low x obtained from an independent analysis of the deep inelastic neutral current scattering data collected with the ZEUS detector in its first year of data taking at HERA in 1992. It begins with a short outline of the history of lepton proton scattering relevant to the development

of the QCD improved parton model. A short overview is presented on the new phenomena expected in the small x domain where the transition between the perturbative and nonperturbative regions occurs. A comparison of the assumptions and methods used in different parton parametrizations at small x are also discussed.

An overview of the HERA injection scheme and the general design parameters are given in Sec. 2. A description of the detector components with an emphasis on the ZEUS calorimeter is given in Sec. 3. The Monte Carlo simulation is described in Sec. 4.

The proton structure function measurement is based on the inclusive neutral current cross section. The precision of this measurement is largely determined by how well the event kinematics is reconstructed. For neutral current events, the kinematic variables can be determined from the scattered electron alone, from the hadronic energy flow, or a combination of both. The kinematics at HERA and the different reconstruction methods are discussed in Sec. 5.

Energetic particles which escape undetected down the beam pipe or lose energy while traversing the inactive material in front of the calorimeter lead to a substantial error in the energy measurements. Hadronic energy losses are shown to be large in the low x region when jets are emitted in the backward direction. A description of the method used to correct for the hadronic energy losses due to these effects is presented in Sec. 6.

The data obtained during the Fall 1992 running period correspond to an integrated luminosity of 24.73 nb^{-1}. The selection criteria that was used to obtain a well measured sample of deep inelastic neutral current events are discussed in Sec. 7. Deep inelastic events are characterized by a significant energy flow at small angles close to the proton beam direction. The observation of a substantial fraction of events in which there was no significant hadronic energy outside of the produced current jet region is also discussed.

The results of the proton structure function F_2 measurement is presented in Sec. 8. The results of the gluon distribution determination from F_2 scaling violation is also presented. A discussion of the checks performed to obtain an estimate of the systematic errors is given.

1.1 The Prediction of Quarks

In the early 1950s Hofstadter and his collaborators investigated the elastic scattering of electrons from the proton at the Mark III linear accelerator in the High Energy Physics Laboratory (HEPL) at Stanford. Their results [5] provided the first direct experimental evidence for the composite structure of hadrons[1]. At the time there was no detailed model describing the internal structure of hadrons. The majority of the physics community considered hadrons to be 'soft' objects with a slightly diffused internal structure and no underlying point-like constituents. Hadrons were thought to be equally fundamental - each particle is a composite of the others. This theory, referred to as the bootstrap model [6], was at the time widely accepted. Theories describing hadrons as particles composed of fundamental constituents, on the other hand, were not as well received.

In 1961 M. Gell-Mann introduced a scheme referred to as the Eightfold Way [7], that allowed one to group baryons and mesons with the same spin according to their charge and strangeness[2]. The eight lightest spin 1/2 baryons including the proton and the neutron form the baryon octet. Similarly, the meson octet consists of the eight lightest spin 0 mesons. The baryon decuplet consists of ten heavier spin 3/2 baryons. At the time, only nine of these were experimentally known. The discovery of the Ω^-, precisely as predicted by Gell-Mann, led to the wide acceptance of the Eightfold Way.

A deeper understanding of the Eightfold Way came only in 1964 when Gell-Mann and Zweig independently proposed that hadrons are composed of elementary constituents called 'quarks' [8]. There are three fundamental types of quarks: up (u), down (d) and strange (s), which can be combined to reproduce the multiplet structure of all the observed hadrons in the Eightfold Way. This quark model asserts that each baryon consists of three quarks (later referred to as valence quarks), and each meson is composed of a quark-antiquark pair. By assigning fractional electron charges to the quarks ($+2e/3$, $-1e/3$, $-1e/3$

1. Particles affected by the strong nuclear force consists of the mesons (π, K, η, ...) and the baryons (p, n, Λ, ...) known collectively as hadrons. Leptons (e, μ, ν), on the other hand, do not participate in strong interactions, and hence can be used to probe the nuclear structure.

2. Strangeness is a property assigned to each particle (like charge, lepton number, baryon number).

for u, d, and s respectively where e is the charge of the electron), the charges of all hadrons come out correctly. The initial success of the quark model initiated extensive searches for quarks, all without success.

The failure of several years of quark searches eventually resulted in the widespread skepticism about the quark model. The notion of confinement, where quarks are confined within hadrons, was introduced by those who supported the quark model. In 1964 O. W. Greenberg [9] proposed that quarks also come in three colors 'red', 'green', and 'blue', which simply denote three new quantum numbers assigned to quarks, in addition to their charge and flavor. The color hypothesis presents the quark model in a way that is consistent with the Pauli Exclusion principle, which states that no two identical fermions can occupy the same state[1]. The color hypothesis also characterizes particular quark combinations such that only 'colorless'[2] particles can occur in nature. With this Ansatz, individual quarks, as well as particles consisting of two or four quarks (antiquarks) could not be observed.

The first of a long series of deep inelastic electron scattering experiments [1] began in late 1967 at the two mile accelerator at the Stanford Linear Accelerator Center (SLAC). Electron beams having energies up to 20 GeV were used to probe the nucleon structure to very small distances than had previously been possible. Their results provided evidence that the proton is composed of point-like constituents [10] whose properties were identical to those of the quarks proposed by Gell-Mann in 1964.

1.2 Scaling and the Parton Model

1.2.1 Parameters and Definitions

The parameters relevant to the scattering of electrons from a nucleon target are shown in Figure 1-1, where E_e is the incident electron beam energy, E_e' is the outgoing electron energy and θ_e is the angle of the outgoing electron relative to the incident beam

1. The Δ^{++} baryon, for example, is supposed to consists of three identical u quarks.

2. If the total amount of each color adds up to zero (red + anti-red, ...), or all three colors are present in equal amounts (red + green + blue), the particle is said to be colorless.

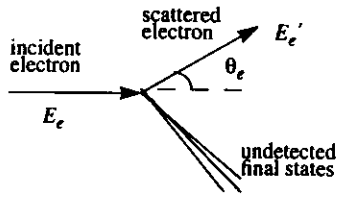

Figure 1-1 Kinematics of electron scattering from a nucleon target at early fixed target experiments at SLAC.

direction. The energy imparted to the undetected recoiling hadronic system is given by

$$\nu = E_e - E'_e. \tag{1-1}$$

The four-momentum q, transferred to the target nucleon is determined directly from measurements of the incident and scattered electrons. Ignoring the electron mass, it is given by

$$-q^2 = Q^2 = 2E_eE'_e(1 - \cos\theta_e). \tag{1-2}$$

If p is the four-momentum of the nucleon in the laboratory frame, two useful variables are

$$\omega = \frac{2p \cdot q}{q^2} \tag{1-3}$$

$$x = \frac{1}{\omega}. \tag{1-4}$$

The invariant mass (also referred to as missing mass) of the recoiling hadronic final state can be obtained as

$$W^2 = (p+q)^2 = M^2 + 2M\nu - Q^2, \tag{1-5}$$

where M is the nucleon mass. Assuming single photon exchange the differential cross section for the inelastic scattering of unpolarized electrons from the unpolarized nucleon target is related to two structure functions W_1, and W_2 [1],

$$\frac{d^2\sigma}{dQ^2d\nu} = \frac{4\pi\alpha^2}{Q^4}\frac{E'_e}{E_e}\left[W_2(\nu, Q^2)\left(\cos\frac{\theta_e}{2}\right)^2 + 2W_1(\nu, Q^2)\left(\sin\frac{\theta_e}{2}\right)^2\right]. \quad (1\text{-}6)$$

From Eq. (1-6) it can be seen that W_2 dominates the cross section at small scattering angles, while W_1 becomes important for large scattering angles. This expression can be rewritten in terms of the Mott cross section, σ_{Mott}, for the elastic scattering of an electron from a point-like spinless object,

$$\frac{d^2\sigma}{dQ^2d\nu} = \sigma_{Mott}\left[W_2(\nu, Q^2) + 2W_1(\nu, Q^2)\left(\tan\frac{\theta}{2}\right)^2\right]. \quad (1\text{-}7)$$

The structure functions measure the departure from a point-like proton structure, and contain all the information that can be obtained about the proton from the scattering of unpolarized electrons.

The differential cross section is also related to the cross sections for the absorption of transversely (σ_T) and longitudinally polarized (σ_L) virtual photons as

$$\frac{d^2\sigma}{dQ^2d\nu} = \Gamma(\varepsilon\sigma_L + \sigma_T). \quad (1\text{-}8)$$

The flux of the transverse virtual photons is given by Γ, and ε measures the degree of longitudinal polarization. The absorption cross sections are related to the structure functions by

$$\sigma_L = \frac{4\pi^2\alpha}{\sqrt{\nu^2 - Q^2}}\left[W_2\left(1 + \frac{\nu^2}{Q^2}\right) - W_1\right] \quad (1\text{-}9)$$

$$\sigma_T = \frac{4\pi^2\alpha}{\sqrt{\nu^2 - Q^2}}W_1 \quad (1\text{-}10)$$

The ratio of the absorption cross sections defines the quantity R in

$$R \equiv \frac{\sigma_L}{\sigma_T} = \frac{W_2}{W_1}\left(1 + \frac{\nu^2}{Q^2}\right) - 1. \quad (1\text{-}11)$$

Its measurement in the early SLAC experiments played a crucial role in identifying the spin of the nucleon constituents.

1.2.2 Early SLAC Results: Evidence of Scaling

Based on his theoretical analyses made prior to the SLAC measurements, J. D. Bjorken suggested that the deep inelastic electron proton scattering process might give an indication of whether there were any point-like constituents inside the proton. His ideas were not well received by the physics community until the first results from the SLAC inelastic measurements were presented in 1968.

Two prominent and unexpected features were suggested by the initial SLAC inelastic measurements. The first was that the measured inelastic cross sections decreased much more slowly with Q^2 compared to the elastic scattering cross sections at constant W as illustrated in Figure 1-2.

The second feature was that the data appeared to 'scale'. This was earlier conjectured by Bjorken during the analysis of the inelastic data. He predicted that in the limit of large ν and Q^2, with the variable ω defined in Eq. (1-3) held fixed, the quantities $2M_pW_1$ and νW_2 (M_p is the proton mass) would depend only on ω:

$$\begin{aligned} 2MW_1(\nu, Q^2) &= F_1(\omega) \\ \nu W_2(\nu, Q^2) &= F_2(\omega). \end{aligned} \quad (1\text{-}12)$$

This phenomenon was referred to as 'scaling' in the variable[1] ω. Figure 1-3 shows the early SLAC data on νW_2 for $\omega = 4$ as a function of Q^2. It was then immediately apparent that Bjorken's scaling hypothesis was correct, the data within errors showed no Q^2 dependence. The implications of the early SLAC results, presented for the first time at the 1968 Vienna conference, were summed up in W. Panofsky's concluding remark [10]:

> "... Therefore theoretical speculations are focused on the possibility that these data might give evidence on the behavior of point-like, charged structures within the nucleon."

1. The variable $x = 1/\omega$ instead of ω came into use in after the initial inelastic measurements.

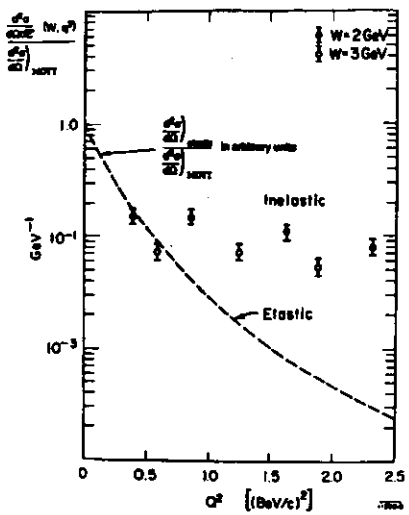

Figure 1-2 The measured inelastic cross sections normalized to the elastic Mott cross section is shown as a function of Q^2 for two values of W. The expectation for the elastic cross section is shown for comparison [1].

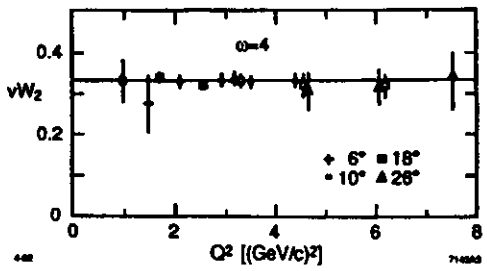

Figure 1-3 Evidence of scaling: νW_2 plotted as a function of Q^2 at ω=4 for different values of the electron scattering angle [1].

1.2.3 The Parton Model

R. Feynman's interpretation of the weak Q^2 dependence of the inelastic cross section and the scaling behavior is embodied in his formulation of the 'parton' model. In this model, he assumed that protons are composed of point-like constituents he called partons. A natural consequence of high energy electrons scattering elastically from charged, point-like partons is the scaling behavior predicted by Bjorken. The struck parton is assumed to be quasi-free during its interaction with the electron. He interpreted the structure function F_2 introduced in Eq. (1-12) as the momentum distribution of the partons, $q_i(x)$, weighted by the squares of their charges,

$$F_2(x) = x\sum_i e_i^2\, q_i(x), \tag{1-13}$$

where e_i is the charge of the ith parton.

Based on these ideas, a more specific formulation was developed in which the partons were interpreted as quarks [11]. In 1968 C. Callan and D. Gross [12] showed that the quantity R defined in Eq. (1-11) is related to the spins of the proton constituents. The kinematic variations of R would provide an important test of the parton model. They showed that the scaling functions are related such that

$$2xF_1(x) = F_2(x), \tag{1-14}$$

indicating that the proton constituents carry spin 1/2. The experimental verification of scaling and the Callan Gross relation in Eq. (1-14) provided the first strong evidence for the existence of quarks, and ultimately led to the identification of the partons with quarks.

In the naive parton model the proton (neutron) is composed of three valence quarks uud (udd) that dominate the scattering at high values of x, in a background of quark-antiquark pairs $u\bar{u}$, $d\bar{d}$, and $s\bar{s}$, referred to as the sea, which gives the main contribution to scattering at low x. In addition, neutral bosons[1] called 'gluons' were

1. Particles are also classified according to their spins: those carrying integral spins are called bosons, while those with half integral spins are called fermions.

introduced, which are responsible for the binding of the constituent quarks inside the nucleon.

The u and d quark distributions have contributions arising from both the valence and sea quarks denoted by the subscripts v and s respectively in

$$\begin{aligned} u(x) &= u_v(x) + u_s(x) \\ d(x) &= d_v(x) + d_s(x). \end{aligned} \tag{1-15}$$

In terms of these distributions, the proton structure function $F^p{}_2$ in Eq. (1-13) can then be written as

$$F_2^p(x) = x[e_u^2(u(x) + \bar{u}(x)) + e_d^2(d(x) + \bar{d}(x))] \tag{1-16}$$

neglecting the strange sea contribution, and where $\bar{u}(x)$ and $\bar{d}(x)$ are the momentum distributions for the anti-up and anti-down quarks. The neutron structure function would be different from Eq. (1-16) since the neutron has a different quark content. The integral of the sum of the proton and neutron structure functions given by

$$\frac{1}{2}\int_0^1 \left[F_2^p(x) + F_2^n(x)\right] = \frac{e_u^2 + e_d^2}{2}\int_0^1 x\left[u_p(x) + \bar{u}(x) + d_p(x) + \bar{d}(x)\right] \tag{1-17}$$

relates the measurable structure functions to the mean square charge of the constituents. The integral on the right hand side is the total momentum fraction carried by the quarks and antiquarks, and should equal to 1 assuming that they carry the nucleon's total momentum. The right hand side would then equal to

$$\frac{e_u^2 + e_d{}^2}{2} = \frac{\left[(2/3)^2 + (1/3)^2\right]}{2}. \tag{1-18}$$

The evaluation of this sum from the results of the SLAC proton and neutron inelastic experiments over the entire kinematic range gave a factor of two smaller than expected. This suggested that the quarks carry only half of the nucleon's momentum, the other half is carried by the gluons. In this case, the fractional charge assignments of the quarks are consistent with the results.

1.3 The QCD Improved Parton Model

By the early 1970s a coherent picture of the nucleon based on a comprehensive theory of Quantum Chromodynamics (QCD) was developed. This theory provides a description of the binding of the quarks inside the nucleon. It is based on the concept of color which was introduced a few years earlier to make the quark model consistent with the Pauli Exclusion principle and to explain why single and certain multiquark configurations do not occur in nature. The strong interactions of the quarks are mediated by the massless gluons, which are also colored objects like the quarks. An important difference between electromagnetic and strong interactions is that unlike the photons, gluons can couple strongly with other gluons. This leads to a 'running' coupling constant, α_s, which increases at large distances (comparable to the proton radius) and decreases at short distances such that the partons behave essentially as free noninteracting particles inside the nucleon. This property, referred to as asymptotic freedom, allows one to compute the color interactions at large momentum transfers using perturbative techniques.

The naive parton model completely ignores the gluon contribution to deep inelastic scattering. Processes wherein gluons are radiated from quarks were neglected. Moreover, the contribution arising from gluons producing quark-antiquark pairs was also neglected. Modifications to the simple parton picture based on QCD was necessary to account for certain features of the experimental data which could not otherwise be explained in a simple parton model. In the QCD improved parton model, the parton distributions acquire a Q^2 dependence $q_i(x) \rightarrow q_i(x,Q^2)$, dictated by the QCD Dokshitzer-Gribov-Lipatov-Altarelli-Parisi (DGLAP) evolution equations [13]:

$$\frac{dq_i(x,Q^2)}{d\ln Q^2} = \frac{\alpha_s(Q^2)}{2\pi}\int_x^1 \frac{dz}{z}\left[P_{qq}\left(\frac{x}{z}\right)q_i(z,Q^2) + P_{qg}\left(\frac{x}{z}\right)g(z,Q^2)\right] \tag{1-19}$$

$$\frac{dg(x,Q^2)}{d\ln Q^2} = \frac{\alpha_s(Q^2)}{2\pi}\int_x^1 \frac{dz}{z}\left[\sum_j P_{gq}\left(\frac{x}{z}\right)q_j(z,Q^2) + P_{gg}\left(\frac{x}{z}\right)g(z,Q^2)\right]. \tag{1-20}$$

In these equations $q_i(x,Q^2)$ denotes a quark or antiquark distribution, and $g(x,Q^2)$ denotes the gluon distribution. The splitting functions $P_{ab}(x/z)$ describes the probability for a

parton b carrying a momentum fraction z to emit another parton a with a fraction x/z of the parent parton momentum.

The inclusion of the gluon processes has two important consequences. First, the struck quark will no longer be collinear with the exchanged virtual photon since the gluon emission can result in the quark recoiling against the radiated gluons. This can be observed experimentally since there would be two hadronic jets produced in the interaction. Second, the parton distributions are no longer functions of just the variable x, but of Q^2 as well. This implies that the measured structure functions will no longer scale.

Scaling violation is a major prediction of QCD. Deviations from the scaling behavior, referred to as scale breaking, were observed as more detailed and substantially more accurate studies came during the next round of SLAC inelastic experiments. Improved data revealed a slight variation of the structure functions with increasing Q^2 at higher values of x ($x > 0.3$) [1], as illustrated in Figure 1-4. The experimental verification of scale breaking provided a strong confirmation of the quark model as described by QCD.

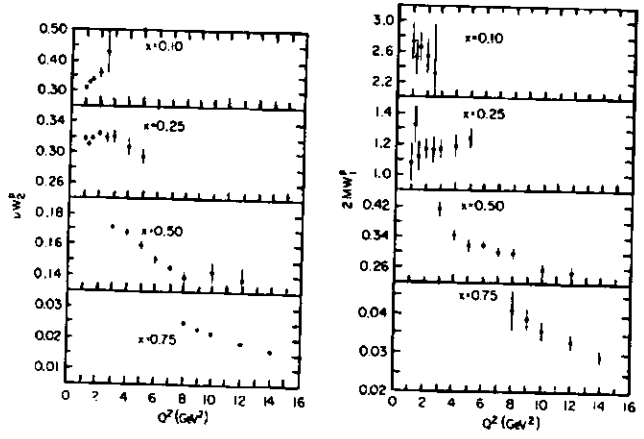

Figure 1-4 Scale breaking: SLAC measurements of the proton structure functions νW_2 and $2M_pW_1$ show a Q^2 dependence at different values of x [1].

1.4 Structure Functions at Low x

In the low x region ($x \sim 10^{-3}$) the dominant contribution to the inelastic scattering process arises from the interactions of the virtual photon with sea quarks. The measured structure functions thus reflect the low x behavior of the sea quark distributions. In the standard QCD framework only decay processes which cause the parton density to increase are taken into account. The growing parton density result in a steeply rising structure function F_2 as $x \to 0$ at large values of Q^2 ($Q^2 \geq 4\ GeV^2$) as described by QCD evolution equations. If the parton density becomes so large that the partons have significant overlap, they can no longer be treated as noninteracting. The growth must eventually be suppressed by interaction processes, such as recombination and annihilation, which might 'saturate' the number of partons or even decrease their density as $x \to 0$. The saturation of the parton densities would be observed as a plateau in F_2 at low x.

The parton interactions arising from their overlapping spatial configurations result in a nonlinear correction to the standard QCD evolution equations, referred to as screening corrections[14]:

$$\frac{dxg(x,Q^2)}{dlnQ^2} = \frac{3\alpha_s(Q^2)}{\pi}\int_x^1 \frac{dz}{z}\left[zg(z,Q^2)\right] - \frac{9}{16R^2}\left[\frac{3\alpha_s(Q^2)}{Q}\right]^2\int_x^1 \frac{dz}{z}\left[zg(z,Q^2)\right]^2 \quad (1\text{-}21)$$

This is the simplest form of the Gribov-Levin-Ryskin (GLR) equation [15] for the gluon density ($xg(x,Q^2)$) evolution. The first term was obtained from the DGLAP equation given in Eq. (1-20) with the assumption that the dominant lowest order contribution to gluon production comes from the diagram in Figure 1-5b, and that the quark contribution in Figure 1-5a can be neglected. In addition, only the most singular term ~ $6/z$ in the splitting function P_{gg} was kept in the limit $z \to 0$. The nonlinear term in the GLR equation leads to a much weaker rise in the gluon density at small x values compared to the standard linear QCD evolution. The size of the screening corrections depend on the parameter R whose value is expected to be between the size of the valence quark ~ $2\ GeV^{-1}$ and the size of the proton ~ $5\ GeV^{-1}$ depending on whether the saturation occurs locally close to the valence quarks (hot spots scenario [16]) or uniformly over the full transverse size of the nucleon. The GLR equation is expected to hold when the quantity W^{sat},

$$W^{sat} = \frac{27\pi\alpha_s(Q^2)}{16R^2Q^2}xg(x,Q^2), \quad (1\text{-}22)$$

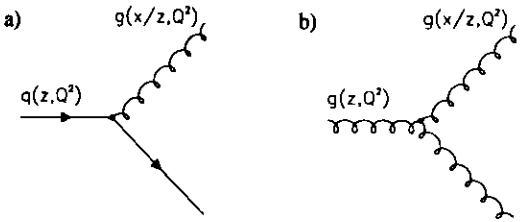

Figure 1-5 Lowest order QCD diagrams for gluon production. Diagrams a) and b) are described by the first and second terms respectively in the DGLAP gluon evolution equation.

obtained from the ratio of the integrands of the nonlinear term and the linear term on the right hand side of Eq. (1-21), satisfies the inequality $W^{sat} \leq \alpha_s(Q^2)$ [14].

The regions of validity of the various evolution equations are shown for both the DGLAP and GLR equations in Figure 1-6. The region of low to intermediate Q^2 is described by the Balitsky-Fadin-Kuraev-Lipatov (BFKL) equation [17]. In the small x region, the singular behavior of the gluon and sea quark distributions is expected:

$$xg\ (x\bar{q}) \sim x^{-\lambda}, \tag{1-23}$$

and is referred to as the Lipatov behavior. This singular behavior will eventually be tamed by shadowing effects. The correction to the BFKL equation is given by the addition of the non-linear term given in Eq. (1-21). A number of interesting and more detailed theoretical reviews on low x physics are given in [14] [18] [19] [20].

1.5 Parton Parametrizations

Parton distribution functions describe how the nucleon's momentum is shared between its constituent quarks and gluons. The structure functions measured in deep inelastic lepton-nucleon scattering experiments can be expressed in terms of these distributions. It is important to have a reliable and precise set of parton distributions at small x ($x < 10^{-2}$) in order to make reliable predictions for any given hadronic process at current and future colliders. In addition, they would provide tests for perturbative QCD and give an insight into the new phenomena expected to become manifest at small x.

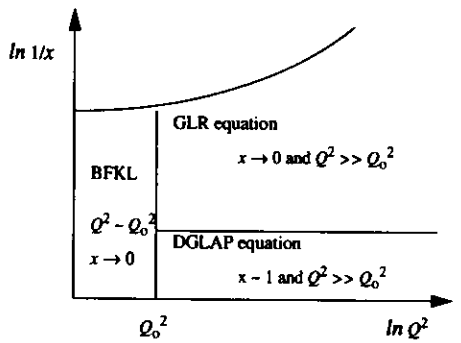

Figure 1-6 The regions of validity of the various evolution equations.

In practice, the parton distributions are generally determined from global fits to a wide range of precision deep inelastic and related data accumulated from early and recent fixed target experiments. The structure functions are expressed in terms of parton distributions parametrized at a sufficiently large reference scale $Q_0^2 \sim 4\ GeV^2$, and calculated at some higher Q^2 using the QCD DGLAP evolution equations [13]. A global fit is then performed to determine the best values for the parameters of the starting distributions. For $x < 10^{-2}$ these distributions are extrapolated by implementing some theoretically motivated guesses concerning the small x behavior of the gluons and sea quarks. The main uncertainty in the extrapolation of the different parton parametrizations to the small x region arises from the lack of knowledge about the gluon distribution and the fact that deep inelastic scattering experiments to date hardly constrain this quantity. A few of the more recent parton parametrizations discussed here are in good agreement with present experimental results, however, they disagree substantially in their predictions for the low x region depending on how flat or steep an input for xg and $x\bar{q}$ has been chosen as $x \to 0$. The predicted structure function $F_2(x,Q^2)$ extrapolated to the low x region obtained from these parametrizations is shown in Figure 1-7 for $Q^2 = 15\ GeV^2$.

The Martin, Roberts and Stirling sets [21] MRS D_0' and MRS D_-', shown in Figure 1-7 as the full and top dashed curves respectively, are based on a global structure function analysis which incorporates the precision measurements of the muon (NMC) [22] and neutrino (CCFR) [23] deep inelastic experiments, as well as the data from

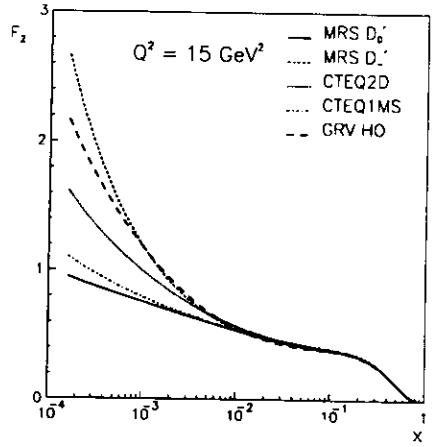

Figure 1-7 The structure function F_2 extrapolated to the small x region obtained from recent parton parametrizations is shown for $Q^2 = 15\ GeV^2$.

BCDMS [24], WA70 [25] and E605 [26]. The MRS starting distributions can be described by simple parametrizations requiring about 15 parameters. The parametrized gluon and sea quark distributions at the reference scale ${Q_o}^2 = 4\ GeV^2$ are required to satisfy xg, $x\bar{q} \sim x^{-\lambda}$ as $x \to 0$. In the D_0' set a constant gluon distribution is assumed ($\lambda = 0$). In contrast, the D_-' set assumes a singular Lipatov behavior for the gluon distribution where $\lambda = 1/2$, leading to a strong rise in the predicted structure function F_2 in the small x region. Motivated by the recent NMC measurement of the Gottfried sum[1] [27], both sets assume a flavor asymmetric non strange sea distribution by allowing $\bar{u}$ and $\bar{d}$ to be different [28],

$$(\bar{u} - \bar{d}) \sim x^{-1/2}(1-x)^a \tag{1-24}$$

where a is a fit parameter. The parametrization for the strange sea distribution is given by

1. The expectation for the Gottfried sum $\int_0^1 \frac{dx}{x}(F_2^p - F_2^n) = \frac{1}{3}\int_0^1 dx\,(u_v - d_v) + \frac{2}{3}\int_0^1 dx(\bar{u} - \bar{d})$ is 1/3 which implies $u = d$.

$$s = \frac{1}{2}\left(\frac{\bar{u} + \bar{d}}{2}\right) \tag{1-25}$$

at ${Q_o}^2$, where the factor of 2 suppression is motivated by the CCFR dimuon results in [29].

An independent parton distribution analysis has recently been presented by the CTEQ[1] collaboration [30] based on essentially the same data sets mentioned earlier. The global fits involve more complicated parametric forms with about 30 parameters and therefore fewer theoretical assumptions are imposed. The small x behavior is essentially determined by the lowest x points of the fixed target data. A flavor asymmetric sea is also allowed by freely and independently parametrizing $\bar{u}$, $\bar{d}$ and s, with no strange sea suppression in contrast to the MRS sets. The predicted F_2 for the original CTEQ1 analysis is shown as the dashed dotted lines in Figure 1-7, while the latest CTEQ2 set, which includes recently published results of the HERA experiments H1 [31] and ZEUS [32], is shown as the dotted curve. In the CTEQ2 set the gluon and sea quark distributions are assumed to have a general form $\sim x^{-a}$ where a is a free parameter fitted to the data.

Glück, Reya, Vogt (GRV) presented an alternative approach in [33] wherein 'valence-like' distributions at a very low reference scale ${Q_o}^2 = 0.3\ GeV^2$ are evolved and fitted to MRS [34] valence quark distributions at higher Q^2. Finite valence-like gluon and non strange sea quark distributions ($\bar{u}$, $\bar{d}$ with $\bar{u} = \bar{d}$) at ${Q_o}^2$ are allowed which satisfy energy momentum conservation [35]

$$\int x\,[v(x, Q_o^2) + G(x, Q_o^2) + 4\bar{u}(x, Q_o^2)]\,dx = 1. \tag{1-26}$$

The strange sea contribution is assumed to vanish at ${Q_o}^2$. Like the conventional fit methods, the valence quark distribution is also required to vanish as $x \to 0$ at ${Q_o}^2$. The predicted F_2 shown in Figure 1-7 is similar to the MRS D_-' set. This strong rise seen for the GRV prediction is a result of the perturbative DGLAP evolution of the valence-like input at ${Q_o}^2$. The GRV predictions have been shown to be in agreement with the recent small x data from NMC [36].

1. CTEQ is an acronym for Coordinated Theoretical/Experimental Project on QCD Analysis and Phenomenology

CHAPTER 2

HERA

The Hadron Electron Ring Accelerator (HERA) [2], located at the DESY (Deutsches Elektronen-Synchrotron) laboratory in Hamburg, is the world's first electron proton (*ep*) collider. Two different magnet systems, one superconducting and one conventional, guide the electron and proton beams respectively, around separate storage rings 6.3 *km* in circumference. HERA can provide polarized electron/positron beams[1] and a massively increased energy scale. Electrons and protons with nominal energies $E_e = 30\ GeV$ and $E_p = 820\ GeV$ collide head on. The resulting center-of-mass energy is $\sqrt{s} = (4E_eE_p)^{1/2} = 314\ GeV$. This is equivalent to a 50 *TeV* electron beam impinging on a fixed target. The beams cross at four interaction regions, two of which are occupied by H1 and ZEUS. The layout of the HERA collider is shown in Figure 2-1. The preaccelerators DESY II/III and PETRA used in the injection scheme are shown in the lower left side.

An enlarged view of the injection scheme is shown in Figure 2-2. The injection system uses the rebuilt synchrotron DESY III and the storage ring PETRA. Negatively charged hydrogen ions are accelerated in a 50 *MeV* linear accelerator. Upon injection into the DESY III synchrotron the ions are stripped. The protons are captured into bunches spaced 28.8 *m* apart[2] and accelerated to 7.5 *GeV*. They are then transferred to PETRA II where they are accelerated to 40 *GeV* before being injected into HERA. A maximum number of 70 bunches can be accumulated in PETRA II. The electron (positron) injection begins with the linear accelerator (Linac II) where energies of up to 450 *MeV* is attainable. Electrons are injected into a storage ring (PIA) and accumulated into a single 60 *mA* bunch. They are injected into DESY II, accelerated up to 7 *GeV*, and transferred to the PETRA II storage ring. This process is repeated at a rate of 12.5 *Hz* until 70 bunches

1. The electron beam was unpolarized in the 1992 running period.

2. This corresponds to the HERA bunch spacing of 96 *ns*.

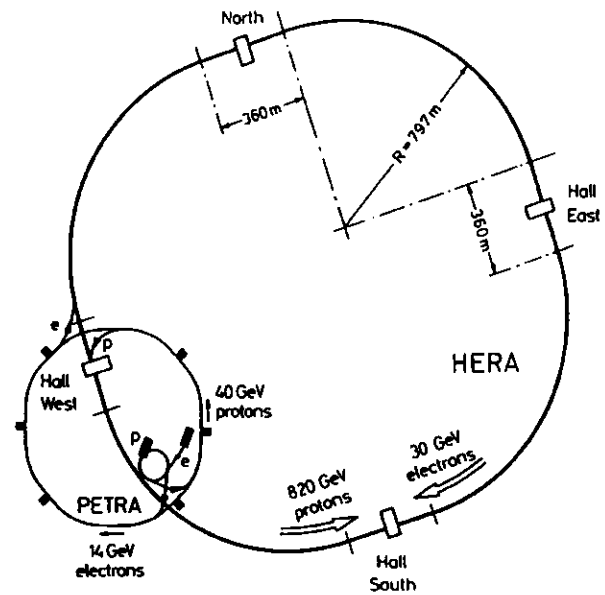

Figure 2-1 Layout of the electron-proton collider HERA. The two interaction regions at Halls North and South are occupied by H1 and ZEUS,respectively.

spaced 28.8 *m* apart have been accumulated. The electrons are then accelerated to 14 *GeV* and injected into the electron storage ring of HERA.

In October 1991 *ep* interactions were first observed at HERA. The two experiments, ZEUS and H1, started data taking in the summer of 1992. The nominal electron beam energy was limited to 26.67 *GeV* since not all the accelerator cavities were installed. An integrated luminosity of about $3\ nb^{-1}$ was delivered during this initial running period. After a brief shutdown a second data taking period during the Fall of 1992 followed. HERA operated with nine colliding electron and proton bunches at the nominal energies of 26.67 *GeV* and 820 *GeV* respectively. One additional unpaired (pilot) electron and proton bunch provided an estimate of the beam associated background. An integrated luminosity of ~ $30\ nb^{-1}$ was delivered in 1992.

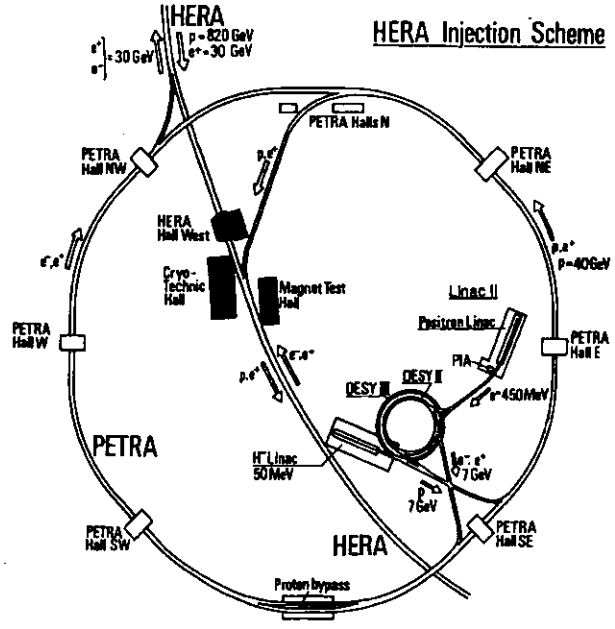

Figure 2-2 Layout of the HERA injection scheme.

The major differences between HERA and other conventional colliders are the asymmetric beam energies and the short beam crossing interval of 96 *ns*. The first condition dictates an asymmetric detector geometry, while the latter condition requires a detector equipped with sophisticated trigger and readout systems. Some general HERA design parameters [37] are listed in Table 2-1, with the 1992 values enclosed in brackets.

Parameter	Units	electron	proton
Nominal energy	*GeV*	30 [26.7]	820 [820]
ep CM energy	*GeV*	314 [296]	
Energy range	*GeV*	10-33	300-820
Injection energy	*GeV*	14	40
Filling time	*min*	15 [60]	20 [300]
Circumference	*m*	6336	
Crossing angle	*mrad*	0	
Luminosity	$cm^{-2}s^{-1}$	1.5×10^{31} [~ 1×10^{29}]	
No. of colliding bunches	-	~ 200 [9]	
Time between crossings	*ns*	96	
Circulating current	*mA*	58 [.5 -2]	163 [.5 -2]
Magnetic Field	*T*	.165	4.65
Horizontal beam size, σ_x	*mm*	.26 [.30]	.29 [.40]
Vertical beam size, σ_y	*mm*	.07 [.07]	.07 [.10]
Longitudinal beam size, σ_z	*mm*	8	400

Table 2-1 Some HERA general design parameters, with the Fall 1992 values enclosed in brackets.

CHAPTER 3

THE ZEUS DETECTOR

At HERA the momenta and the angles of the final state particles produced in *ep* collisions impose detector requirements on calorimetry, tracking devices and particle identification. The large momentum imbalance between the incident protons and electrons results in event topologies where most particles are produced within a narrow cone around the proton beam direction. The center-of-mass system, boosted in the forward direction in the laboratory frame, manifests itself in the asymmetric detector. The detector also has to be able to cope with the short bunch crossing interval of 96 *ns*.

The ZEUS detector at HERA was designed to achieve the best possible energy measurement of electrons and jets in deep inelastic neutral current (NC) and charged current (CC) events. In particular, the precise reconstruction of the kinematic quantities x, y, and Q^2 over a large range, which is of crucial importance to the structure function measurement, puts an emphasis on calorimetry and tracking. The measurement of the energy and position of the scattered electron in the final state of NC events requires a good tracking system and a calorimeter with a good electromagnetic energy resolution. For CC events, a large missing transverse momentum is carried away by the undetected neutrino in the final state. Hence the measurement of the hadronic final state is vital and requires a calorimeter with the a good hadronic energy resolution and which covers as much of the 4π solid angle as possible. The calorimeter information is enhanced by tracking and particle identification measurements carried out by other detector components.

Cross sectional views of the ZEUS detector parallel and perpendicular to the beam axis are shown in Figure 3-1. The direction of the proton beam defines the positive z axis, the positive y-axis points up and the positive x axis points towards the center of the HERA machine. Polar angles are measured with respect to the proton beam axis. The detector components are described in the following sections.

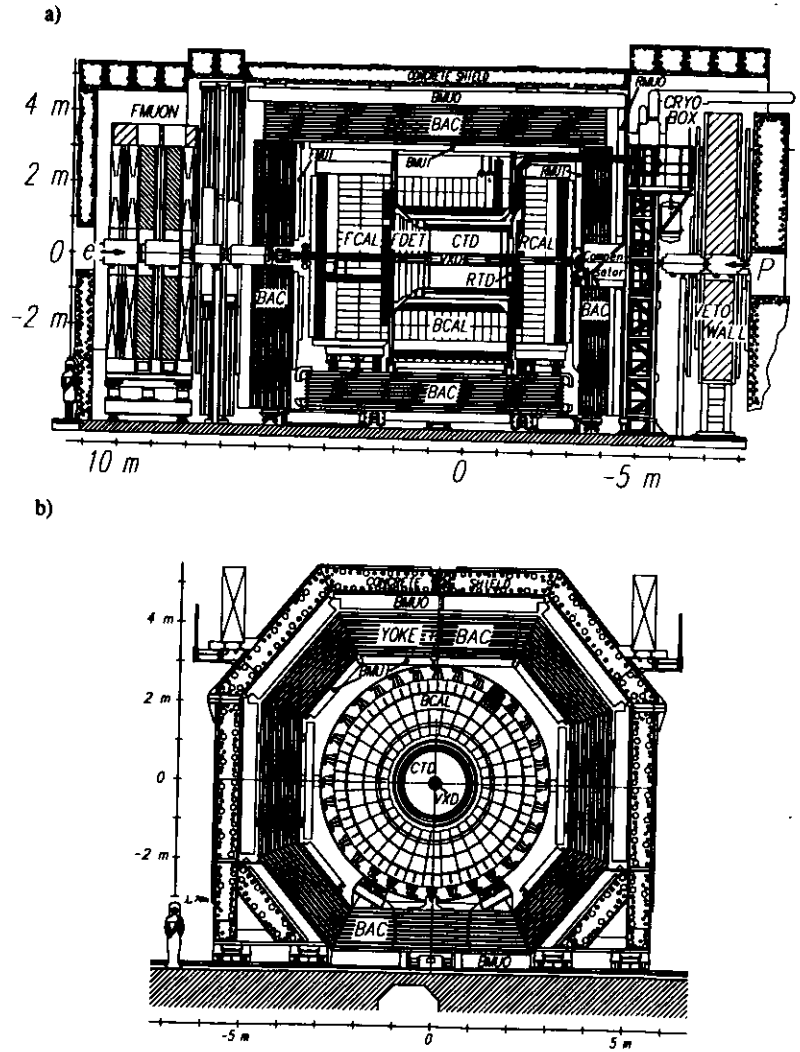

Figure 3-1 Cross sectional views of the ZEUS detector. a) Parallel and b) perpendicular to the beam axis.

3.1 Tracking System

The essential requirements of the tracking system include a good transverse momentum resolution of $\sigma(p_T) \sim (0.003)p_T$, particle recognition using the energy loss (dE / dx) measurements, tracking close to the beam line, and precise vertex determination. The inner detector components are shown in Figure 3-2 and are listed below.

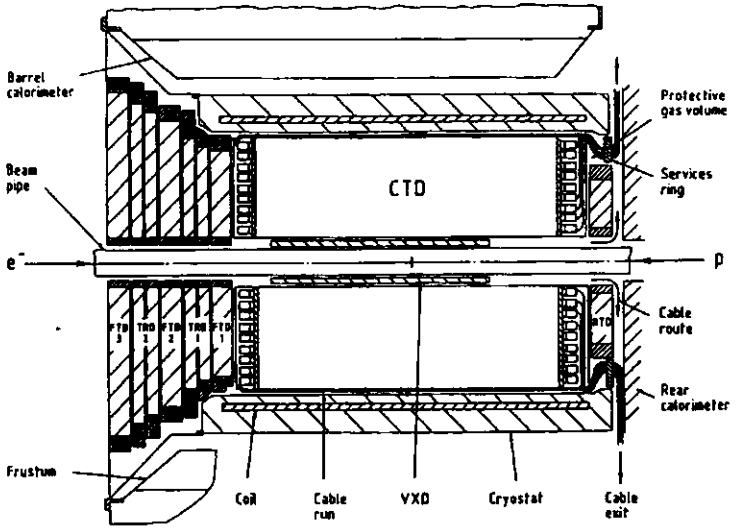

Figure 3-2 A cross sectional view of the inner tracking detector along the beam axis.

• Vertex detector (VXD): Its primary tasks include the detection of short-lived particles by reconstructing secondary vertices, and the improvement of the momentum and angular resolution of charged particles measured in the central tracking region. It is a cylindrical drift chamber, with an inner/outer radius of 9.9/15.9 *cm*, consisting of wires running parallel to the beam enclosed in a carbon fiber vessel. It has 120 drift cells, each with twelve sense wires 1.6 *m* long running parallel to the beam. Field wires alternating with the sense wires are 3 *mm* apart. A spatial resolution of 30 μm has been achieved.

• Central tracking detector (CTD): Charged particle trajectories are reconstructed in the polar region of $15° < \theta < 164°$ surrounding the interaction region. The CTD is a cylindrical drift chamber 2.41 *m* in length and has an inner/outer radius of 16.2/85 *cm*. The layout of the wires in the CTD is shown in Figure 3-3. Nine cylindrical layers referred to

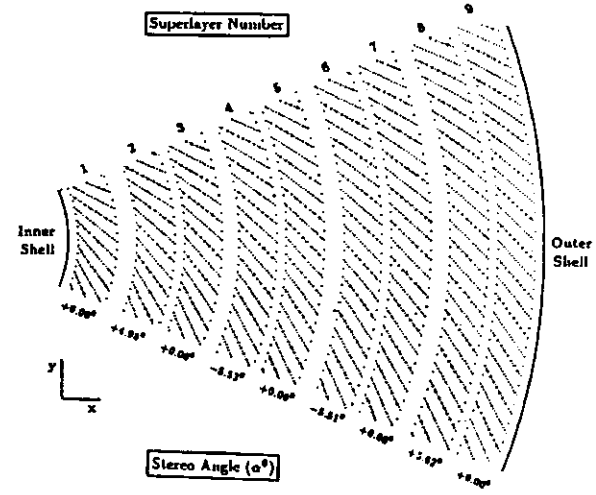

Figure 3-3 The layout of the wires in the CTD (an octant is shown). The sense wires are indicated by the larger dots.

as superlayers has eight sense wire layers in each. The odd numbered superlayers run parallel to the beam and the even ones are tilted by a stereo angle of up to $\pm 6°$ to determine the z-position of the hits. The design position resolution in the r-ϕ plane (perpendicular to the beam axis) is 100-120 μm and 1-1.4 *mm* in the z direction using the stereo wires for a fully operational CTD. The z resolution was ~ 4 *cm* when using only the z-by-timing readout in 1992. For particles traversing all nine superlayers[1] at 90° the design momentum resolution is $\sigma(p)/p = (0.0021)p \oplus 0.003$ [38].

1. During the Fall 1992 running period only three superlayers 1,3 and 5 were operational. These superlayers were equipped with z-by-timing readout to determine the z-position of the hit using the time difference between the signals arriving at the two ends of the wires.

• Forward and rear tracking detectors (FTD, RTD): Additional tracking detectors are located in the forward and the rear directions. The FTD, which consists of three planar drift chambers, provides tracking with a polar angle coverage of $7.5° < \theta < 28°$ in the forward direction. The RTD is a single planar chamber covering $160° < \theta < 170°$. Each of the chambers of the RTD and FTD consists of three layers of drift cells perpendicular to the beam axis with fixed wire orientations of 0°, +60°, and -60°. The transition radiation[1] detector (TRD) was designed for optimal electron identification in the momentum range of 1-30 *GeV* in the forward direction. With an angular coverage of $7° < \theta < 26°$, the TRD consists of four 10 *cm* deep modules, each holding a radiator followed by a drift chamber. Two TRD modules are positioned are positioned in each of the two 21 *cm* wide gaps between three FTD chambers.

3.2 Magnet System

A superconducting solenoid (coil) is installed inside a 2.8 *m* long cryostat and encloses the central tracking region at an inner radius of 92.5 *cm*. To reduce the degradation of particle energy measurements in the calorimeter, the thickness of the coil was minimized to ~ 0.9 radiation lengths (X_0). The coil can provide a maximum magnetic field[2] of 1.8 *T* which enables simultaneous tracking and charged particle transverse momentum measurements. The magnetic field's influence on the beams is compensated by another superconducting coil (compensator) installed behind the rear calorimeter.

3.3 Iron Yoke and Backing Calorimeter

The iron yoke provides a return path for the magnetic field flux produced by the solenoids. The yoke can be magnetized up to 1.6 *T* by normal conducting coils to allow an independent momentum measurement of the muons traversing the barrel muon chambers. It has a shape of an octagonal cylinder and surrounds most of the detector components. It consists of 7.30 *cm* thick iron plates with multi-wire proportional chambers interspersed in the 3.7 *cm* gaps between the plates. These chambers and the iron slabs of the yoke form

1. Transition radiation is generated by charged particles passing through the boundary of two materials with different dielectric constants.

2. The magnetic field was ~ 1.43 *T* during the 1992 running period.

the backing calorimeter (BAC) which is used to measure the hadronic energy leakage for those events which are not fully contained in the calorimeter. The BAC has a hadronic energy resolution of ~100%/$\sqrt{E}$.

3.4 Muon detection

An important element of the QCD studies and searches for new physics at HERA is lepton identification. In addition to the electron identification provided by the tracking system and the calorimeter, it is essential to have an excellent muon detection coverage over the maximum solid angle. This is achieved by a muon detector which is divided into three sections:

• Forward muon detector (FMUON): It is situated in the forward hemisphere to identify high momentum muons down to very small angles close to the beam axis where the momentum resolution of the inner tracking detector deteriorates. It consists of two iron toroids sandwiched between the drift chamber planes and the time of flight counters. Each toroid is magnetized to an internal magnetic field of 1.7 *T* by normal conducting coils. Together with the iron yoke they provide the necessary bending power for precise momentum measurements.

• Barrel and rear muon detectors (BMUON, RMUON): The main task of these components is to identify muon tracks penetrating the calorimeter and the iron yoke. It consists of muon chambers placed inside (BMUI, RMUI) and outside (BMUO, RMUO) the yoke. The muon trajectory is measured by four planes to provide position and direction information both inside and outside the yoke. The angular acceptance is $\theta > 34°$ and the position resolution is better than 1 *mm*.

3.5 Small Angle Detectors

3.5.1 Luminosity Monitor

The luminosity monitor (LUMI) measures the luminosity (as discussed later in Sec. 7.1) by detecting bremsstrahlung photons from the process $ep \rightarrow e\gamma p$. The scattered electrons are deflected by the magnets from the nominal orbit since they have energies lower than the nominal beam energy. These electrons leave the beam pipe through an exit

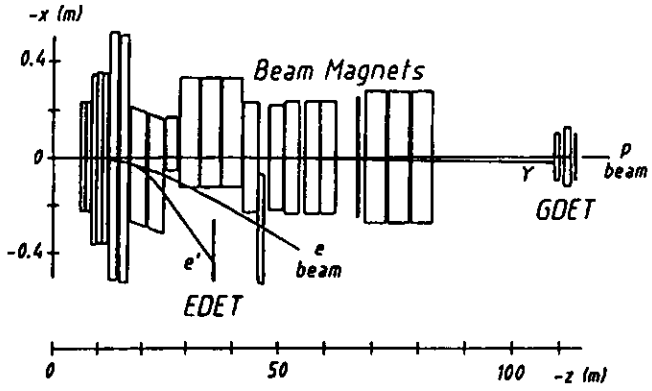

Figure 3-4 The electron and photon branches (EDET and GDET) of the luminosity monitor located at 35 and 108 *m*, respectively downstream from the IP.

window located 27 *m* downstream of the interaction point (IP), and are detected in an electromagnetic calorimeter (denoted by EDET in Figure 3-4) at z = -35 *m*. The bremsstrahlung photons continue undeflected and leave the beam pipe through an exit window 92 *m* away from the IP. They are detected in the photon calorimeter γ cal (denoted by GDET in Figure 3-4) installed at = -108 *m*. The lead scintillator calorimeter has a depth of 22 X_0 and has an energy resolution of $\sigma(E_\gamma)/E_\gamma = 18.5\%/\sqrt{E_\gamma}$ where E_γ is the photon energy in *GeV*. A carbon filter is placed in front of the γ cal to absorb the large flux of low energy photons (< 50 *MeV*) from synchrotron radiation. To veto events wherein the photon converts into an e^+e^- pair, a Cherenkov counter is placed between the γ cal and the carbon filter. The geometric acceptance for the photons is independent of the photon energy and is ~ 98%. The electron calorimeter is 21 X_0 deep and has a similar energy resolution as the γcal. However, the geometric acceptance is energy dependent and is over 70% for electrons with energy E_e' in the range $0.35\,E_e < E_e' < 0.65\,E_e$, where E_e is the nominal electron beam energy.

3.5.2 Leading Proton Spectrometer

Due to the large momentum imbalance between the electron and proton beams at HERA, the proton debris in *ep* collisions is emitted at very small forward angles down the beam pipe. The leading proton spectrometer (LPS) allows the measurement of forward scattered protons, with small transverse momenta $p_T < 1$ *GeV/c* and fractional momenta $p/p_{beam} = 0.3 - 1$, generated by processes such as diffractive photoproduction, photon gluon fusion, as well as neutral and charged current interactions. A high precision spectrometer makes it possible to gain access to this very forward region. It consists of an array of six Roman pots[1] used together with the bending magnets of the HERA ring. Six silicon strip detector planes are mounted on each pot. The LPS was not instrumented during the 1992 running period.

3.6 C5 Collimator

The beam pipe in the ZEUS region is equipped with masks and collimators to reduce the high rates of synchrotron radiation and beam-gas or beam-wall interactions. The C5 collimator, installed behind the rear calorimeter, consists of four scintillator counters which provide accurate timing information for both electron and proton beams useful for the rejection of proton beam-gas events.

3.7 Vetowall

The vetowall (VETO) shields the detector from the proton beam halo particles and vetoes beam-gas interactions. Situated behind the rear calorimeter 7.5 *m* upstream of the IP, it consists of an 87 *cm* thick iron wall equipped with two plates of scintillator counters placed on both sides of the wall, perpendicular to the beam axis. It is 800 *cm* wide and 760 *cm* high with a square hole 95×95 cm^2 for the beam pipe and HERA magnets. Early MC studies [39] on beam-wall interactions (beam protons scraping the beam pipe) suggested that there would be more beam-wall activity in the region closer to the HERA ring. Consequently, the layout of these counters was chosen to be asymmetric as shown in Figure 3-5. An event is considered a beam-gas interaction if there is a

1. A Roman pot is a detector placed inside a movable section of the vacuum chamber. The deflection of particles in the magnetic field produced by the machine quadrupoles is measured to determine their momenta. At HERA this apparatus will be useful to tag quasi-elastically scattered protons in diffractive processes.

coincidence between the corresponding counters in either the inner[1] or outer trigger regions on either side of the iron wall.

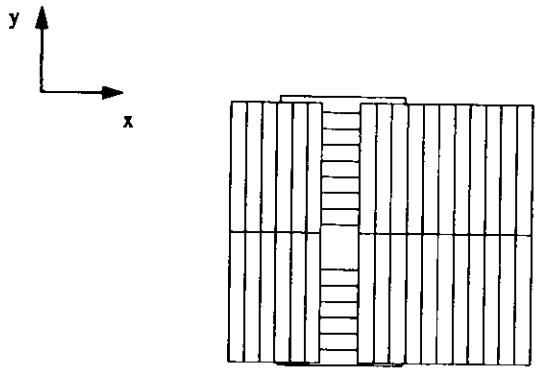

Figure 3-5 Layout of the scintillator counters on the sides of the vetowall perpendicular to the beam axis.

3.8 High Resolution Calorimeter

Calorimetry has greatly influenced the scope of high energy physics experiments. The attractive capabilities of calorimeters have been essential to precision measurements of particle energies and position. Ideally, a calorimeter has to have a sufficient depth to stop all incoming particles. For calorimeters the depth increases logarithmically with the incident particle energy, whereas for magnetic spectrometers the depth varies as $\sqrt{E}$ [40]. A calorimeter is sensitive to both charged and neutral particles. Its different response to muons, electrons and hadrons can be exploited for particle identification. Muons incident on a calorimeter lose energy mainly through ionization. High energy electrons/positrons and photons incident on a calorimeter generate 'electromagnetic showers', which result from a cascade process of creating lower energy charged secondaries through bremsstrahlung and pair production. 'Hadronic showers' are more complicated than

1. The inner trigger region consists of the three scintillation counters closest to the beam hole, and the rest of the counters form the outer trigger region.

electromagnetic showers. This is largely due to the greater variety and more complex nature of hadronic processes. The response of calorimeters to muons, electrons and hadrons are discussed in more detail in the following section.

3.8.1 Overview of Calorimetry

A calorimeter is a device to measure the energy of impinging particles. It consists of an absorbing material in which the incident energy is dissipated by shower processes and an active material which produces a detectable signal, in the form of light or ionization charge, which is proportional to the absorbed energy. When the absorbing material acts as both the absorber and active material, the calorimeter is said to be homogeneous. A homogeneous calorimeter is often used in the measurement of electromagnetic showers. However, it does not have enough stopping power for hadronic showers to be fully contained within a compact volume. A sampling calorimeter, on the other hand, makes use of alternating layers of heavy absorbing material (e.g. lead, iron, or uranium) and lighter signal producing material (e.g. gas, liquid argon, silicon diodes or plastic scintillators). This type of calorimeter design leads to a "sampling" of a fraction of the energy in the active material with uncertainties in the energy measurements or sampling fluctuations.

There are large differences in the shower development of various types of particles. Muons predominantly lose energy by ionization. As they traverse the detector muons lose an almost fixed amount of energy which only depends on the type and amount of material, and which may be small compared to their actual energies. In first approximation muons are then treated as minimum ionizing particles (mips). At higher energies processes including ionization, bremsstrahlung, and pair production contribute such that the average ionization energy becomes energy dependent. This effect is shown in Figure 3-6 where the mean energy loss for muons in polystyrene (plastic scintillator) and uranium is plotted as a function of energy. The energy loss for minimum ionizing particles (mips) as well as the most probable ionization loss of muons in uranium are shown for comparison.

The interactions of electrons, positrons and photons incident on the calorimeter give rise to electromagnetic showers. High energy photons can produce electron-positron pairs. At lower energies the dominant process for photon energy loss is by the photo-

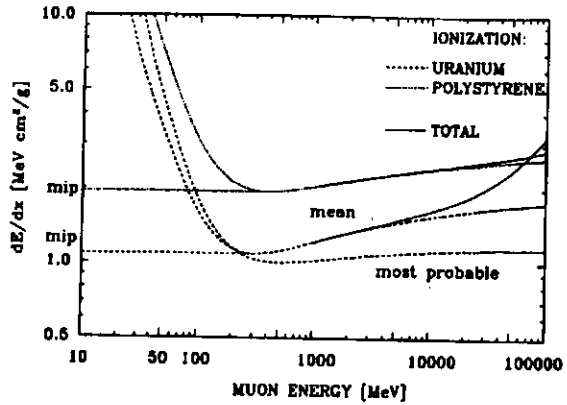

Figure 3-6 Mean energy loss of muons in polystyrene and uranium shown as a function of energy. Full lines represent the total energy loss including ionization, bremsstrahlung, and pair production. For comparison the energy loss of minimum ionizing particles (mips) and the most probable ionization loss of muons in uranium are also shown [41].

electric effect. The dominant process for high energy electrons and positrons is bremsstrahlung in which the energy loss is proportional to Z^2, where Z is the atomic number of the absorber. For low energy electrons and positrons ionization is dominant and the energy loss is proportional to Z *log* Z. Figure 3-7a shows the contributions of different processes to the photon cross section in lead as a function of energy and Figure 3-7b shows the fractional energy loss per radiation length as a function of electron or positron energy. The energy at which radiative and ionization losses are equal is called the critical energy. For the electrons the critical energy is [42]

$$E_c = \frac{800}{Z+1.2}\ [MeV]. \tag{3-1}$$

The absorption of electromagnetic showers is characterized by the quantity [42]

$$X_o = \frac{716.4}{Z(Z+1)\ln(\frac{287}{\sqrt{Z}})} A\ [gm\ cm^{-2}] \tag{3-2}$$

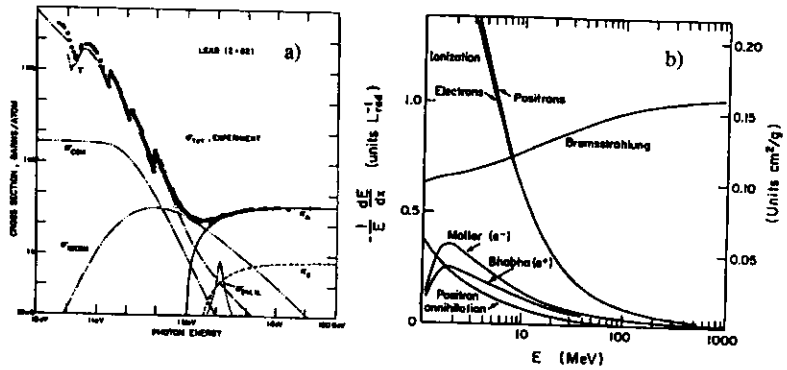

Figure 3-7 The contributions of different processes to the photon cross section in lead as a function of energy. a) The photo-electric effect (τ) is the dominant mechanism for energy loss at low photon energies ~ 1 *KeV*, and pair production (κ) at energies > 1*MeV*. b) The fractional energy loss per radiation length for electrons and positrons in lead is shown as a function of energy. The critical energy, E_c, is the point of intersection of the bremsstrahlung and ionization curves [42].

where A is the atomic mass of the absorbing material. The longitudinal development of the shower is determined by the high energy part of the shower and scales as the radiation length of the material. For an incident electron with energy E, the depth at which the shower maximum[1] occurs is given by

$$t_{max} = ln(\frac{E}{E_c}) + C_i \tag{3-3}$$

where $C_\gamma = +0.5$ for photons and $C_e = -0.5$ for electrons. A depth of approximately 2.5 t_{max} is required to contain 98% of the electromagnetic shower at HERA energies [40]. The transverse shower development scales with the Molière radius

$$R_M = \frac{E_s}{E_c} X_o \tag{3-4}$$

1. This corresponds to the maximum number of particles in the electromagnetic shower given by [43] $N_{max} \approx 0.31\,(E/E_c)/\sqrt{ln\,(E/E_c) - 0.25}$.

where $E_s = 21.2\ MeV$. The Molière radius gives the lateral spread of the electron shower with critical energy, E_c, after traversing 1 X_0. On average about 90% of the energy is contained within 1 R_M and 99% within 3 R_M [43].

A charged hadron incident on a calorimeter will lose its energy by ionization before any hadronic interaction occurs. The successive inelastic hadronic interactions of the secondary particles with the nuclei of the absorbing material initiates the development of the hadron shower. A hadron shower has an electromagnetic component from neutral mesons such as π^0 and η decaying into photons. The hadronic component consists of protons, pions ($\pi^+\pi^-$), kaons (K^+K^-), neutrons, muons and neutrinos from meson decays. A substantial amount of the available energy is lost in the form of nuclear binding energy, breakup and excitation of the nuclei, minimum ionizing particles, and escaped neutrinos which will not be detected (invisible energy). Hadronic interactions with the nuclei of the absorbing material at energies above 50 *MeV* induce a spallation process, i.e. a series of independent particle collisions with the target nuclei and subsequent deexcitations by emission and evaporation of particles. At each deexcitation the spallation process is accompanied by nuclear fission of heavy nuclei. As the development of hadronic showers is based largely on nuclear interactions. The scale for the longitudinal development is determined by the nuclear interaction length, λ, which approximately scales with the nuclear radius as [42]

$$\lambda = \lambda_{INT} = 35\ A^{1/3}\ [g/cm^2] \tag{3-5}$$

Measured from the face of the calorimeter, the maximum of a hadron shower is [42]

$$t_{max}(\lambda) = 0.2\ ln(E) + 0.7 \tag{3-6}$$

where E is the incident energy of the primary hadron in *GeV*. The approximate depth necessary for almost full containment of the shower is [40]

$$L_{0.95}(\lambda) = t_{max} + 2.5\ \lambda\ (E)^{0.13}. \tag{3-7}$$

Both parametrizations describe the available data to within 10% for energies up to a few hundred *GeV*. For the lateral containment of a hadron shower, a cylinder with radius $R_{0.95} \leq \lambda$ is required. This radius does not scale with λ and decreases for materials with higher Z [40].

The total energy of the incident particle is proportional to the track length of the shower it produces. This energy is randomly subdivided into visible and invisible components in the active and passive layers respectively. This leads to the sampling fluctuations of the measured fraction of the total energy. The electromagnetic and hadronic energy resolution of sampling calorimeters is dominated by sampling fluctuations resulting in a fractional resolution which scales as $1/\sqrt{E}$, where E is the incident particle energy. Deviations from $1/\sqrt{E}$ occur because of noise effects, non-uniformities, calibration errors, pedestal fluctuations, energy leakage, and the unequal calorimeter response to electrons and hadrons ($e/h \neq 1$). Results of these effects are included by a constant term b in $\sigma/E = a/\sqrt{E} \oplus b$. Due to the substantial amount of invisible energy lost by strongly interacting hadrons in the passive layers, the calorimeter response to electrons is larger compared to hadrons. In order to optimize the hadronic energy resolution, the fluctuations in the invisible energy as well as the relative fluctuations between the electromagnetic and hadronic components of the shower have to be minimized. This is achieved in compensating calorimeters by equalizing the efficiencies of converting the energy deposits to measurable signals for the electromagnetic and hadronic components, $e/h = 1$.

3.8.2 The ZEUS Calorimeter

The ZEUS calorimeter consists of alternating layers of 3.3 *mm* thick depleted uranium[1] (DU) as the high Z passive absorber and 2.6 *mm* plastic scintillator as the active material. Cladding the DU plates with a thin layer of lighter material such as stainless steel prevents[2] low energy photons produced in the absorber from reaching the active layers. This effectively lowers the e/h ratio. On the other hand, neutrons produced in hadronic showers lose relatively more ionization energy in the scintillator. The ratio of the thickness of absorber to active material was chosen to achieve full compensation and the best energy resolution. Using uranium as the passive material helps in compensating for the losses in hadronic showers and ensures sufficient energy containment within a reasonable depth.

1. The DU is an alloy of 98.4% ^{238}U, 1.4% Nb, and $\leq 0.2\%$ ^{235}U.

2. The steel cladding around the absorber plates reduces the DU natural radioactivity to a level that does not present a troublesome background to energy measurements, but does provide a stable calibration monitor.

As shown in Figure 3-8 the calorimeter encloses the solenoid and inner tracking detectors, and is divided into three parts covering three overlapping polar angle regions.

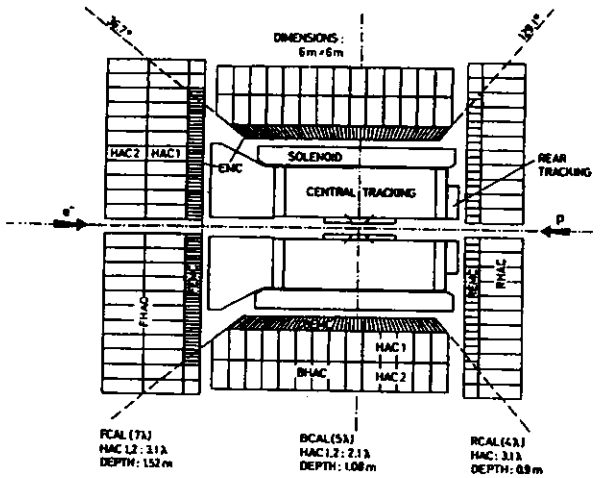

Figure 3-8 The high resolution calorimeter completely surrounds the inner tracking detectors and the solenoid. It is divided into three components: FCAL, BCAL, and RCAL covering the polar angles as shown.

- The forward calorimeter (FCAL) extends from $2.2° \leq \theta \leq 39.9°$.
- The barrel calorimeter (BCAL) extends from $36.7° \leq \theta \leq 129.1°$.
- The rear calorimeter (RCAL) extends from $128.1° \leq \theta \leq 176.5°$.

The FCAL and RCAL each consists of 23 modules placed vertically forms a wall facing the IP. The BCAL has 32 wedge-shaped modules placed symmetrically around the beam axis, each spanning 11.25° in azimuth. In the FCAL, BCAL, and RCAL each module is subdivided into towers of transverse dimensions typically $20 \times 20\ cm^2$, which are further segmented longitudinally into an electromagnetic (EMC) and one or two hadronic (HAC)

calorimeter sections. Each tower in the FCAL and BCAL generally consists of four $5 \times 20\ cm^2$ EMC cells, a HAC1 and a HAC2 cell. In the RCAL each tower consists of two 10×20 EMC cells and a HAC cell. A finer segmentation for the FEMCs is important since there is more energy deposited in the forward direction due to the boosted center of mass of the system. Each cell is read out by two photomultiplier tubes (PMTs)[1] to provide redundancy as well as a more accurate position measurement within the cell. At normal incidence the EMC section has a depth of about 25 X_0 or 1λ. The depth of the HAC varies depending on the polar angle. In the FCAL and BCAL, the HAC sections (HAC1 and HAC2) have a combined depth of 6λ and 4λ respectively. In the RCAL there is only one HAC section with a depth of 3λ. The total depths for the FCAL, BCAL and RCAL are then 7λ, 5λ, and 4λ respectively. These depths were chosen to contain at least 95% of the energy of 90% of the jets with maximum energy allowed by the kinematics at HERA [43]. Further details on the mechanical design and construction of the ZEUS calorimeter can be found in [44]. An electromagnetic energy resolution of $\sigma/E = 18\%/\sqrt{E}$, a hadronic energy resolution of $35\%/\sqrt{E}$ and an e/h ratio = 1.0 ± 0.02 have been achieved [45].

3.8.3 Calorimeter Readout

Particles passing through the calorimeter deposit energy in the scintillator. This energy appears as light which is detected by the PMTs. The PMT output pulses are sampled, shaped, amplified and stored in analog form in the 'analog cards' which are physically mounted on the calorimeter modules [46]. The shaped signals are sampled every 96 *ns* and stored in the analog pipelines. The signal is split into a high and a low gain channel by input impedances. The ratio of each high and low gain scales is set differently for each calorimeter section to account for the asymmetric collider geometry and to achieve an adequate energy measurement over the full dynamic energy range at HERA. To allow the detector components to participate in the first level of triggering, a pipeline delay of 5 μs has been chosen. Each pipeline chip can hold 58 samples, so that it can store up to 5.6 μs of data. If an event is triggered a one-event analog buffer stores up to eight samples from each pipeline, and provides them to the 'digital cards'. Each digital card digitizes signals from two analog cards. The event buffer in a digital card can store up to 35 events. Energies and times represented by each PMT pulse are calculated by the

1. The ZEUS calorimeter contains of 11836 PMTs or 5918 cells.

digital signal processor which resides on the digital card. The digital signal processor uses a large number of calibration constants to correct the digitized data for PMT timing offsets due to different propagation lengths, as well as any variation in the pedestal voltages and the gain factors of every single pipeline and buffer cell. The reconstructed times and energies are then passed to a transputer network which formats the data and makes it available to the next level of triggering.

3.8.4 Calibration

A large number of calibration parameters affect the response of the calorimeter readout, from the light production in the scintillator to the analog signal at the front-end electronics. These parameters, called calibration constants, are monitored periodically by performing regular checks.

The calibration of the front-end electronics is validated by injecting a specific amount of charge to each channel using a digital-to-analog converter. A correct reconstructed charge ensures the proper functioning of the readout chain and helps in identifying dead or problematic channels. Random triggers also provide the means of checking whether the calibration constants still correct properly for the distortions of the signals by the readout electronics. These triggers are generated when there is no signal produced in the detector. For these 'empty' events, the measured energy should be zero.

Light generated from a nitrogen laser is injected through a network of optical fibers mounted on the modules into the transition piece in each PMT. The laser calibration system monitors the stability of the gain and linearity of each PMT.

An important calibration tool is the current generated by the natural radioactivity of the depleted uranium, referred to as the uranium noise (UNO). By adjusting the high voltage (HV) setting of the PMTs, the UNO current can be set to a predetermined nominal value such that the charges collected from different PMTs are set on the same energy scale. This scale determines the conversion of the collected charges from the PMTs to the deposited energy.

An initial testbeam experiment was performed for testing and calibrating the ZEUS calorimeter modules at CERN and at FNAL [45]. The primary aim was to test the

performance of the calorimeter in a real beam environment, to measure the uniformity of the response of the different calorimeter sections, to measure the calorimeter resolution, and to determine the precision of the overall calibration over a large energy range. A number of modules were calibrated using electron, muon, and hadron beams. To investigate the uniformity of the EMC towers, the beam was aimed at normal incidence at the centers of each EMC tower along a module. The average EMC tower to tower uniformity using a 50 *GeV* electron beam is ~ 1 % as shown in Figure 3-9 for a particular BCAL module. The uniformity of the response within an EMC tower was investigated by aiming an electron beam at the tower while moving the module in very small steps, and

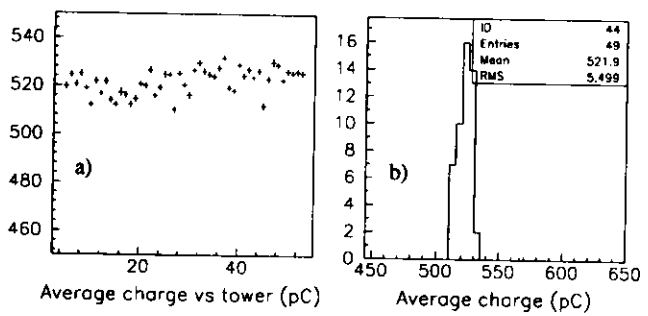

Figure 3-9 Results from the Fermilab testbeam. a) The collected charge in each of the EMC towers in a BCAL module in the FNAL testbeam is shown versus tower number using a 50 *GeV* electron beam at normal incidence. b) The rms of the charge distribution indicates a tower to tower uniformity at the 1% level.

thus effectively scanning across the face of individual towers with the beam. Similarly, the response of the EMC towers across the inter-tower boundaries and inter-module gaps were determined. The charge collected from 40 *GeV* electrons starting from the midpoint of one tower to the midpoint of the next tower is shown in Figure 3-10a. A gap of 1 *mm* between scintillator plates is responsible for the ~10% drop in the calorimeter response across the boundary between the EMC towers. The corresponding deterioration of the energy resolution is shown in Figure 3-10b. The module to module variation is shown to be within 1% [45]. The linearity of the calorimeter response to both electrons and hadrons at

varying beam energies between 6 - 110 GeV is also shown to be within 1% [45]. Testbeam results therefore indicate that the absolute calibration of the calorimeter is understood to better than 1%.

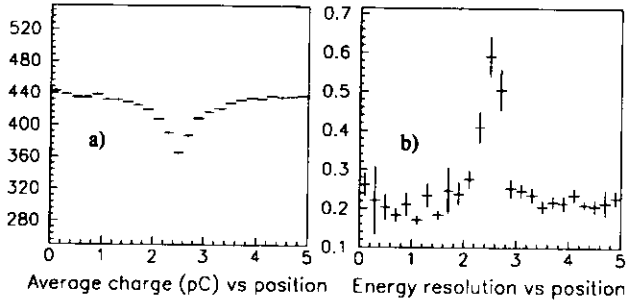

Figure 3-10 Results from the Fermilab testbeam. a) The average charge (pC) as a function of position from the midpoint of one EMC tower to the midpoint of the next EMC tower in the BCAL. A ~10% drop in the response is due to the 1 mm gap between the EMC towers. b) The energy resolution is shown to deteriorate across the boundary between two EMC towers.

3.8.5 Time Measurement

Time measurements are used to select DIS events and to reject background arising from cosmics and upstream proton beam-gas interactions. The calorimeter calibration was chosen such that the nominal time of deep inelastic ep interactions originating from the interaction point is t ~ 0. The calorimeter provides a time resolution ≤ 1 ns.

Times in the FCAL, BCAL and RCAL are the energy weighted average of the measured times of the PMTs with energy deposits $E_i > 200$ MeV,

$$\bar{t} = \frac{\sum_{PMT} w_i t_i}{\sum_{PMT} w_i}, \tag{3-8}$$

where w_i is defined as

$$w_i = \begin{cases} 0 & E_i < 200MeV \\ E_i & 200MeV \leq E_i \leq 2GeV \\ 2 & E_i > 2\ GeV. \end{cases} \tag{3-9}$$

The time distributions for ep events are shown in Figure 3-11. A time resolution less than 1 ns is measured in the RCAL. The FCAL time distribution is wider than that of the RCAL because the proton bunch length is substantially larger than the electron bunch length. This excellent time resolution provides a powerful tool in the rejection of cosmic and upstream proton beam-gas background. This is discussed in Sec. 7.4.

3.8.6 Noise

The noise on the calorimeter comes from two sources: electronic noise and uranium noise (UNO). The UNO in normal data taking differs from the UNO signal used for calibration. For calibration purposes, the mean UNO is obtained by integrating the noise signal over a period of 20 ms which is long compared to the sampling interval of 96 ns. The contribution of noise to the measured energy is caused by the fluctuations of the UNO signal in the calorimeter cells.

The measured energies in the FCAL, BCAL, RCAL are shown in Figure 3-12 for random triggers. The empty events should result in a zero reconstructed mean energy in the calorimeter. In Figure 3-12 the plots show that on average the calorimeter energies differ from zero by less than 50 MeV for the PMT output sums. This is an indication of the accuracy of the determination of the calorimeter calibration constants.

3.9 Hadron Electron Separator

The calorimeter's electromagnetic and hadronic sections are well suited to identify isolated electrons in neutral current events. The identification of electrons inside the jets is a more difficult problem since the electron signal is much smaller compared to the hadrons. In this case, the combined information from the calorimeter, tracking detectors and the transition radiation detector in the FCAL is insufficient. The hadron electron separator (HES) provides an additional device for improved electron identification. It consists of one or two planes of arrays of 3×3 cm^2 silicon diodes. This granularity is

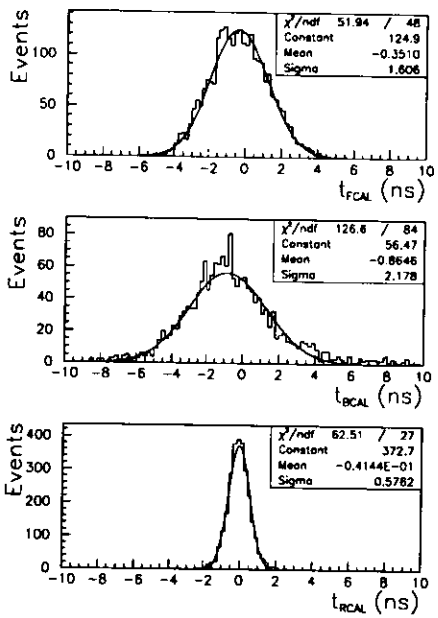

Figure 3-11 Plot showing the measured times in the FCAL, BCAL and RCAL in *ns*. The RCAL time resolution is 0.6 *ns* while the time resolution in the FCAL is wider reflecting the length of the proton bunch.

finer than the calorimeter segmentation, and provides a tool for a improved position resolution of showers. The HES planes may be inserted at 3.3 X_0 inside the RCAL and BCAL, 3.3 X_0 and 6.3 X_0 in the FCAL. At this depth, electromagnetic showers give a large signal in one or more HES diodes. Hadrons, on the other hand, usually interact at greater depths, and thus behave like minimum ionizing particles in the HES. A few RCAL modules were equipped with HES during the Fall 1992 running period and placed in the RCAL (RHES). In this analysis, the information from the RHES is used in the reconstruction of the scattered electron's position as described in Sec. 7.2.

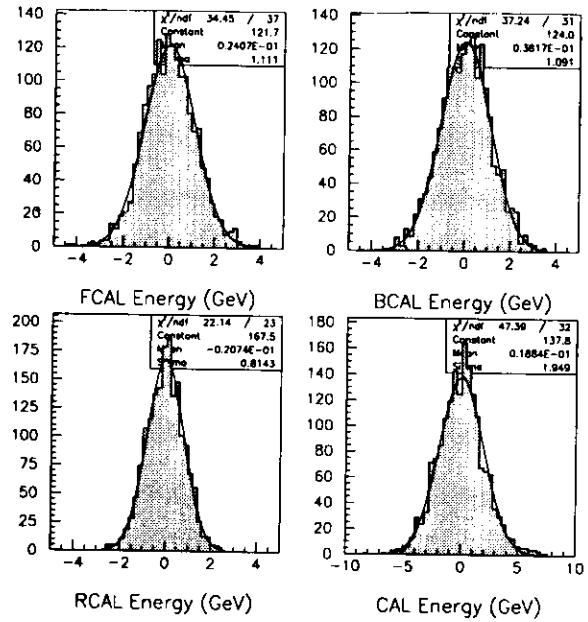

Figure 3-12 The measured energies in the FCAL, BCAL, RCAL are shown for a random trigger run. These plots show that on average these energies differ from zero by less than 50 *MeV*.

3.10 ZEUS Trigger and Data Acquisition Systems

Bunch crossings at HERA occur every 96 *ns* which is equivalent to 10^7 crossings per second. The total interaction rate, which is dominated by upstream beam-gas interactions, was estimated to be of the order of 50 *KHz*. A three-level trigger system is used to reduce this rate to a few *Hz*.

Each detector component has its own front-end readout electronics and processing environment which independently transfers data to the central data acquisition (CDAQ) system. A pictorial overview of the CDAQ and three-level trigger systems is shown in Figure 3-13 [47].

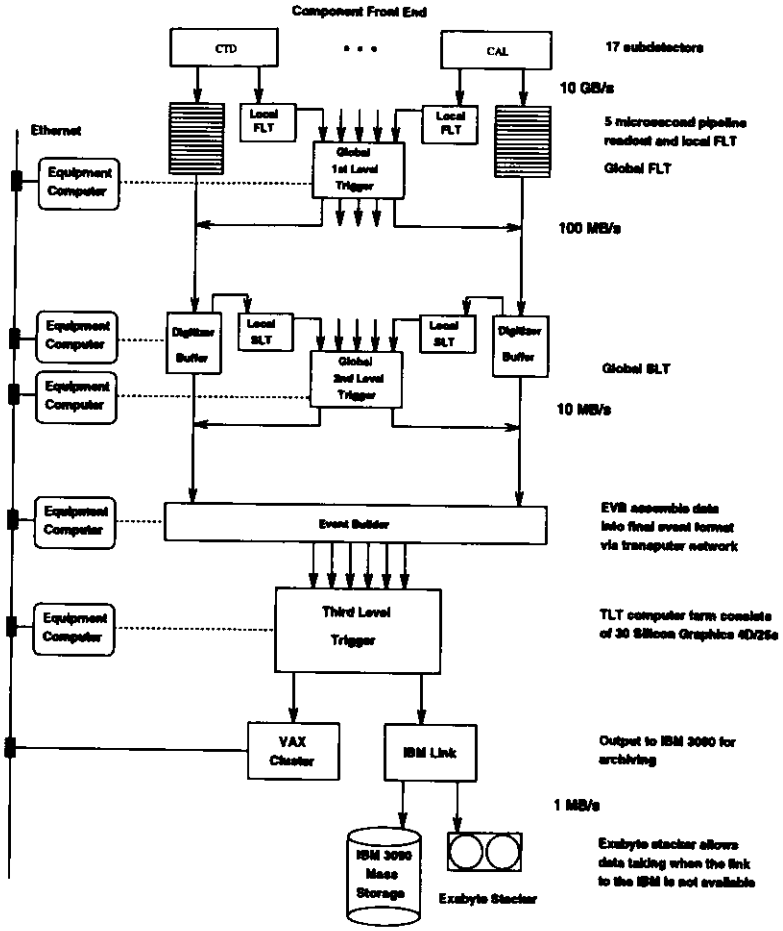

Figure 3-13 Outline of the ZEUS trigger and data acquisition [47].

The first level trigger system is a hardware trigger. It is designed to reduce the input rate to 1 *KHz*. The data from the components are stored in pipeline buffers until a decision has been issued at the first level trigger. Each component can have its own local first level trigger (FLT) which must make a trigger decision within 5 μs after the bunch crossing. The decisions from these local trigger systems are collected and passed to the global first level trigger (GFLT) which makes a decision on the global information. The GFLT decides whether to accept or reject the event.

If the event is accepted, the event is passed to the second level trigger (SLT). Each component can also have its own SLT system. The SLT is software-based and runs on a network of transputers. It is designed to reduce the rate from the GFLT input of 1 *KHz* to 100 *Hz*. Local second level trigger decisions are passed to the global second level trigger (GSLT) which decides whether to accept or reject the event.

If the event is accepted, the digitized data from each component is merged into a single data stream by the Event Builder. The data is passed to the third level trigger (TLT) which is also software-based. The TLT consists of a farm of Silicon Graphics (SGI) workstations. It is designed to reduce the rate from the GSLT input of 100 *Hz* to a few *Hz*. The output is limited by the rate at which data can be transferred to the DESY main site and written to tape. A small fraction of the accepted events are also monitored on-line.

CHAPTER 4

MONTE CARLO SIMULATION

In high energy physics, Monte Carlo simulation is a necessary tool which allows one to make a direct comparison between theory and experiment. In many cases numerical methods are also possible, however, Monte Carlo simulation is often preferable due to its generality, flexibility, and applicability to complex processes.

To a first approximation, the basic lepton-quark scattering processes are well understood. However, modifications to this simple picture arising from quark confinement and higher order QCD corrections result in a complicated evaluation of such processes. The main objective of a Monte Carlo (MC) event generator is therefore to generate events which describe as closely as possible the observed events in the detector.

In general, MC generators can be grouped into two classes: event generator programs which simulate the physical processes based on a theoretical model and detector simulation programs which simulate the detector behavior. In the planning stage of an experiment, Monte Carlo event generators are used mainly to study the kind as well as the rate of events one may expect. In addition, event generators aid in the design and optimization of the experimental apparatus. In the running stage of an experiment, event and detector simulation programs are used mainly a) to devise analysis strategies that can be used on real data for optimized signal-to-background conditions, b) to estimate detector acceptance corrections to be applied on the raw data for the extraction of the true physics signal, and c) to provide a framework within which the experimental measurements can be described in terms of a basic underlying theory. The following sections give a brief description of the event and detector simulation programs used in this analysis.

4.1 DIS sample

A Monte Carlo (MC) sample consisting of about 50k deep inelastic neutral current (NC) scattering events were generated at $Q^2 > 4\ GeV^2$ with the Morfin-Tung parton

parametrizations [48] using HERACLES [49]. This program, which includes first order electromagnetic and weak radiative corrections, has been shown to give reliable results for very small x down to $x = 10^{-4}$ and large y up to $y = 0.99$. In high energy processes the description of the hadronic final state requires calculations of multiple parton emissions in QCD, referred to as QCD cascades. This is necessary for a proper simulation of general event properties such as energy flows and particle multiplicities. The hadronic final state was simulated using ARIADNE [50] for the QCD cascade. ARIADNE is based on the color dipole formulation of QCD [51], where gluon emission is treated as radiation from the color dipole formed between the point-like struck quark and the extended proton remnant. ARIADNE simulates the gluon emission, and the following cascade process where gluons emit further (softer) gluons or split into quark-antiquark pairs. The final state quarks and gluons in ARIADNE are used as input to JETSET [52]. This program simulates the production of colorless hadrons from the partons produced in the QCD cascade, referred to as the 'hadronization' process, according to the LUND model [53]. In this model, the colored quarks are connected by 'strings' with 'kinks' representing the gluons. After a high energy collision, the struck quark rapidly moves away from the rest of the partons within the nucleon, thus stretching the string. Hadrons are then formed when the string expands and fragments into shorter pieces which do not have sufficient energy to break further.

The output from the event simulation is passed through the ZEUS detector simulation program MOZART[1] in which the outgoing stable particles are traced through the detector and the response of the detector is simulated. It is based on the general detector simulation package GEANT [54] and incorporates the best description of the experimental condition of the ZEUS detector and trigger.

4.1.1 Dead Material Simulation

In the ZEUS detector the depth of the inactive material in front of the calorimeter as simulated in the MC is shown in Figure 4-1 as a function of the polar angle. The inactive material causes particles coming from the interaction point (IP) to lose energy

1. MOnte Carlo for ZEUS Analysis Reconstruction and Triggering.

before reaching the calorimeter. An increase in fluctuations due to variations in the amount of energy lost in the inactive material leads to a degraded energy resolution.

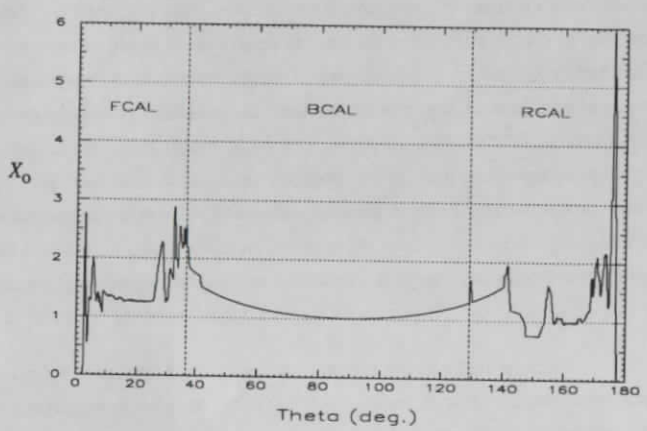

Figure 4-1 The inactive material in the detector in radiation lengths (X_0) as a function of the polar angle as simulated in the MC.

The distributions of the measured energy and angle of the scattered electron from the data and the MC simulation are shown in Figure 4-2 for a direct comparison. The scattering angle is well simulated in the MC as good agreement is seen in Figure 4-2b. However, there is a significant disagreement in the electron energy distribution between data and MC as illustrated in Figure 4-2a. The measured energy spectrum in the data is slightly broader and shifted to lower energies. This is attributed to the energy loss due to some inactive material in front of the calorimeter which is improperly described in the MC. Figure 4-3 shows the electron energy distributions in the left and right sides of the calorimeter. The energy spectrum in the right side is shifted to lower energies which indicates that there is more dead material on this side of the calorimeter than is simulated in the MC. The difference in the electron energy distribution between the two sides of the calorimeter in the data is not reproduced in the MC simulation. This effect is isolated to a region around the beam pipe and is attributed to the inaccurate description of the vertex detector readout cables in the MC.

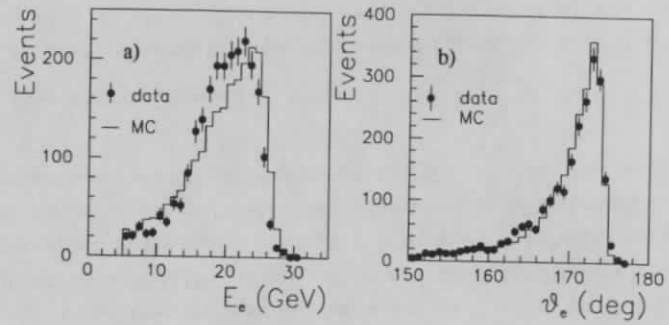

Figure 4-2 Data and MC comparison. Distributions of the a) the scattered electron energy and b) angle.

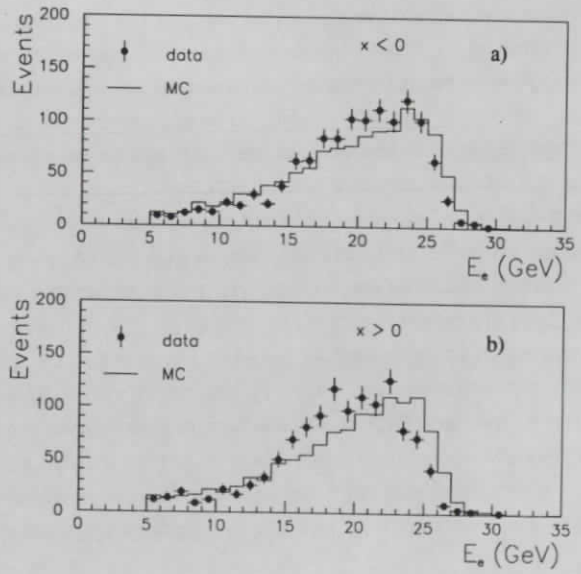

Figure 4-3 Electron energy distributions in the data and MC. a) The left side ($x < 0$) and b) right side ($x > 0$) of the calorimeter are shown.

4.2 Photoproduction Sample

Neutral current *ep* scattering at very small Q^2 ($Q^2 \sim 0$) is understood to proceed via the emission of a quasi-real photon which subsequently interacts with the proton's constituents. This process, commonly referred to as photoproduction, is the main source of background for deep inelastic scattering (DIS) events. In photoproduction events, the electron is scattered through a small angle and goes down the beam pipe. However, the presence of another electromagnetic energy deposit from a photon or a low energy charged pion in the calorimeter may be falsely reconstructed as an electron. To estimate the background due to photoproduction (see Sec. 7.5.1), the program PYTHIA [55] was used to generate events with $Q^2 < 2\ GeV^2$. In PYTHIA the spectrum of the scattered electron was generated down to $Q^2 \sim 0$ using the ALLM [56] parametrization of the total photoproduction cross section. Results obtained from the measurement of the total photoproduction cross section at HERA are given in [57].

CHAPTER 5

RECONSTRUCTION OF x, y, Q^2 IN NEUTRAL CURRENT EVENTS

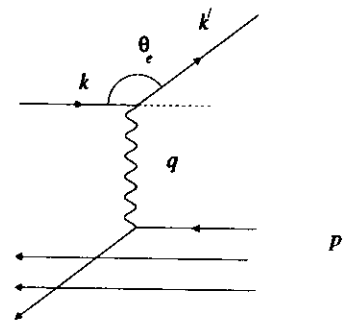

Figure 5-1 The basic diagram for the inelastic electron proton scattering process, where k, and k' denote the four-momenta of the incoming and outgoing electron, p and q that of the initial proton and exchanged boson respectively. The angle of the scattered electron is denoted by θ_e.

The inelastic electron proton scattering process is illustrated in Figure 5-1, where the variables k and k' represent the four-momenta of the incoming and the scattered electron respectively, and p that of the initial proton. The incident electron impinges on the proton and interacts with one of its constituent quarks via a virtual photon exchange. The struck quark fragments into a jet of hadrons, usually known as the "current" or "target" jet, while the spectator partons give rise to a "fragmentation" or "remnant" jet which goes in the direction of the incoming proton. The scattered electron and the current jet emerge back to back in the azimuthal direction and balances each other in transverse momentum.

Taking the direction of the initial proton as the positive z axis and assuming that the lepton and proton rest masses are negligible with respect to the energies measured in

the laboratory frame, the four-momenta are defined as

$$k = \begin{bmatrix} E_e \\ 0 \\ 0 \\ -E_e \end{bmatrix} \qquad k' = \begin{bmatrix} E_e' \\ 0 \\ E_e' \sin\theta_e \\ E_e' \cos\theta_e \end{bmatrix} \qquad p = \begin{bmatrix} E_p \\ 0 \\ 0 \\ E_p \end{bmatrix} \tag{5-1}$$

for the incoming electron, scattered electron and the incident proton respectively. E_e, E'_e are the initial and final electron energies and E_p is the incident proton energy. The outgoing electron is scattered at an angle θ_e relative to the incoming proton direction. The square of the total center-of-mass energy is

$$s \equiv (k+p)^2 = m_e^2 + m_p^2 + 2k \cdot p \approx 4E_e E_p. \tag{5-2}$$

Assuming azimuthal symmetry, the overall event kinematics in Figure 5-1 can be specified by two independent Lorentz variables. These variables are usually chosen to be any two of x, y, and Q^2. The dimensionless variables x and y are defined as[1]

$$x = \frac{-q^2}{2p \cdot q} \tag{5-3}$$

$$y = \frac{p \cdot q}{k \cdot p}, \tag{5-4}$$

where y can be viewed as the normalized energy loss of the scattered electron in the proton rest frame, and the variable x can be interpreted as the fraction of the initial proton momentum carried by the struck quark in a frame where the proton has infinite momentum[2]. The square of the momentum transferred between the electron and proton,

$$Q^2 = -q^2 = -(k-k')^2 = sxy, \tag{5-5}$$

describes the resolution by which the exchanged photon probes the structure of the proton.

1. Note: The earlier definition of x in Eq. (1-4) corresponds to the z axis in the e^- beam direction.

2. In this frame, the proton energy is much greater than its mass so that the proton as well as its constituent partons can be considered massless particles.

At design energies of $E_e = 30\ GeV$ and $E_p = 820\ GeV$, HERA covers a wide x, Q^2 range. The maximum attainable Q^2 extends up to $10^5\ GeV^2$ corresponding to a spatial resolution of about $10^{-18}\ cm.$, and x down to 10^{-5} can be probed.

5.1 The reconstruction of x, y, Q^2

A precise reconstruction of the kinematical quantities x, Q^2 in Figure 5-1 is crucial in the measurement of the proton structure function. The conventional method used in fixed target experiments determines x, Q^2 from the final state electron energy and scattering angle. Another possibility is to determine x, Q^2 from the hadronic flow using jet measurements or using the Jacquet-Blondel method [58]. These reconstruction methods are discussed in the following sections. Combining the final state electron and hadronic flow information, the measurable kinematic phase space can be extended and x, Q^2 determined to better accuracy. There are a number of ways to do this combination, in particular, the mixed method which combines the excellent Q^2 determination from the electron method with the hadronic y Jacquet-Blondel measurement, and the double angle method which is insensitive to the energy calibration of the detector. The different reconstruction methods as well as the choice of which one is best suited for the structure function measurement will be discussed in the following sections.

5.1.1 Electron method

The Lorentz invariant kinematical variables x, y and Q^2 can be determined by measuring the scattered electron energy and angle, E'_e and θ_e. The square of the four-momentum transfer Q^2 defined at the lepton vertex is

$$Q^2 = -q^2 = -(k-k')^2 \approx 2E_e E'_e (1+\cos\theta_e). \tag{5-6}$$

Using the definitions in Eq. (5-1) to Eq. (5-6), the variables x and y expressed in terms of E'_e and θ_e are

$$x = \frac{E'_e \left(\cos\frac{\theta_e}{2}\right)^2}{E_p \left[1 - \frac{E'_e}{E_e}\left(\sin\frac{\theta_e}{2}\right)^2\right]} \tag{5-7}$$

$$y = 1 - \frac{E'_e}{E_e}\left(\sin\frac{\theta_e}{2}\right)^2 . \tag{5-8}$$

The square of the four-momentum transfer given in Eq. (5-8) can be expressed in terms of the scattered electron energy E'_e as

$$Q^2 = Q^2(x, E'_e) = \frac{sx\left(1 - \frac{E'_e}{E_e}\right)}{\left(1 - x\frac{E_p}{E_e}\right)} \tag{5-9}$$

and in terms of the scattered electron angle θ_e as

$$Q^2 = Q^2(x, \theta_e) = \frac{sx}{1 + x\frac{E_p}{E_e}\left(\tan\frac{\theta_e}{2}\right)^2}. \tag{5-10}$$

The scattered electron energy and angle contours are shown in Figure 5-2 for the x and Q^2 phase space available at HERA given the incident electron and proton energies $E_e = 26.7\ GeV$ and $E_p = 820\ GeV$. The lines of constant y values at 1.0, 0.1 and 0.02 are shown as the dashed lines. It is apparent from Eq. (5-8) that small electron scattering energies give high y values. Electron energy measurements deteriorate at lower energies due to degrading calorimeter resolutions. Electrons scattered in the rear direction (BCAL-RCAL boundary shown as the dashed dotted line for $\theta_e = 129.1°$ in Figure 5-2b populate the $Q^2 < 10^3\ GeV^2$ region. The RCAL beam pipe (dashed dotted line at $\theta_e \geq 176.5°$) sets a lower limit on the Q^2 acceptance at about $3\ GeV^2$.

The x and Q^2 dependence on the measurement errors of the outgoing electron energy E'_e and scattering angle θ_e are given by

$$\frac{\delta x}{x} = \frac{1}{y}\frac{\delta E'_e}{E'_e} \oplus \left[\tan\frac{\theta_e}{2} + \left(\frac{1}{y} - 1\right)\cot\frac{\theta_e}{2}\right]\delta\theta_e \tag{5-11}$$

$$\frac{\delta Q^2}{Q^2} = \frac{\delta E'_e}{E'_e} \oplus \left(\tan\frac{\theta_e}{2}\right)\delta\theta_e, \tag{5-12}$$

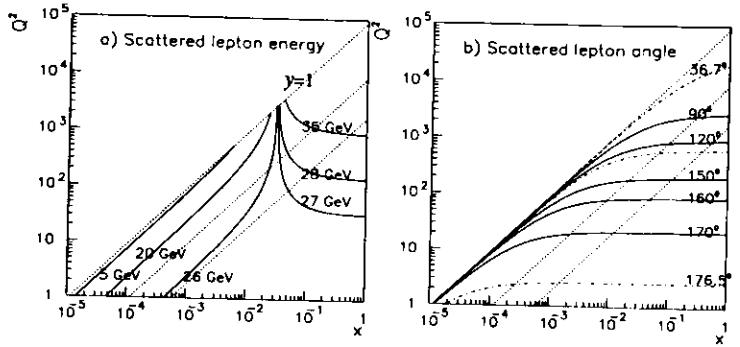

Figure 5-2 Electron reconstruction method. a) Contours of constant scattered electron energies and b) angles in the x and Q^2 phase space for electron and proton beam energies E_e=26.7 *GeV* and E_p=820 *GeV* respectively. The dashed lines are lines of constant y values 1.0, 0.1 and 0.02. The dashed-dotted lines represent the FCAL/BCAL boundary at θ=36.7°, BCAL/RCAL boundary at θ=129.1°, and the RCAL beam pipe at θ=176.5° respectively.

where $\oplus$ implies a quadratic sum. For y reasonably close to 1, the x measurement is well determined. The resolution in x deteriorates with decreasing y and diverges at $y \sim 0$ due to the $1/y$ factor in the energy error term in Eq. (5-11). A miscalibration of the scattered electron energy is amplified by this $1/y$ factor. Hence, a reasonable x measurement based on the scattered electron information alone cannot extend below $y \sim 0.1$ assuming that the electron energy scale is known to within 1%. The resolution in Q^2 is very good except at large scattering angles when the second term in Eq. (5-12) dominates.

The electron energy scale at ZEUS is understood at a few percent level primarily because of the less than exact knowledge of the inactive material between the beam pipe and the calorimeter (see Sec. 4.1). Although the Q^2 resolution is still reasonable, the resolution in x is poor. Given this understanding of the electron energy scale, this reconstruction method is then not suited for the structure function measurement.

5.1.2 Jacquet-Blondel method

From the measurement of outgoing hadrons in the current jet, with the assumption that the struck quark carries a momentum fraction xp and that the mass of the hadrons in the current jet is negligible, the four-momentum transfer squared is,

$$Q^2 = -(xp - p_J)^2 = 2xE_pE_J(1 - \cos\gamma_J). \tag{5-13}$$

Here E_J, p_J and γ_J are the energy, four-momentum and the direction of the current jet respectively. The variables x and y can then be determined by

$$y = \frac{E_J}{E_e}\left(\sin\frac{\gamma_J}{2}\right)^2 \tag{5-14}$$

$$x = \frac{E_J\left(\cos\frac{\gamma_J}{2}\right)^2}{E_p\left[1 - \frac{E_J}{E_e}\left(\sin\frac{\gamma_J}{2}\right)^2\right]}. \tag{5-15}$$

It should be noted that at small values of x and y, the jet masses are no longer negligible and would lead to a systematic bias in the calculation of the kinematical variables [59].

In the x and Q^2 phase space, the constant jet energy and jet angle contours are

$$Q^2(x, E_J) = \frac{sx\left(1 - \frac{E_J}{xE_p}\right)}{\left(1 - \frac{E_e}{xE_p}\right)} \tag{5-16}$$

$$Q^2(x, \gamma_J) = \frac{sx}{1 + \frac{E_e}{xE_p}\left(\cot\frac{\theta_J}{2}\right)^2} \tag{5-17}$$

as shown in Figure 5-3. A minimum jet energy requirement of a few GeV would exclude a region in the x, Q^2 phase space around $x \sim 10^{-3}$ and Q^2 below 10 GeV^2. The effect of the forward beam hole (for $\gamma_J < 5°$) gives the main acceptance limit such that jet measurements cannot extend into the small y and high x region.

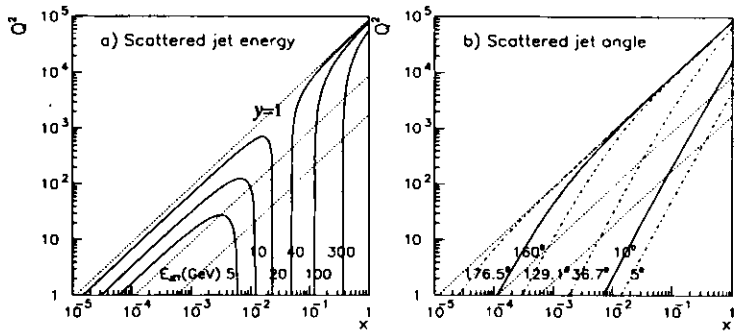

Figure 5-3 Kinematics reconstructed from hadron information. a) Contours of constant scattered jet energies and b) angles in the x and Q^2 phase space for electron and proton beam energies E_e=26.7 GeV and E_p=820 GeV respectively. The dashed lines are lines of constant y values 1.0, 0.1 and 0.02.

As in case of the electron measurement, the reconstruction errors arise from two main effects namely the size of the beam hole, the uncertainties in the measurement of the energies and angles of the outgoing particles. The resolution in x and Q^2 using the current jet information diverges at y ~ 1 as seen in the following equations,

$$\frac{\delta x}{x} = \frac{1}{1-y}\frac{\delta E_J}{E_J} \oplus \left[2\cot\gamma_J + \frac{2y-1}{1-y}\cot\frac{\gamma_J}{2}\right]\delta\gamma_J \tag{5-18}$$

$$\frac{\delta Q^2}{Q^2} = \frac{2-y}{1-y}\frac{\delta E_J}{E_J} \oplus \left[2\cot\gamma_J + \frac{y}{1-y}\cot\frac{\gamma_J}{2}\right]\delta\gamma_J. \tag{5-19}$$

Ignoring the precision of the angular measurements, the resolution in Q^2 degrades as y becomes small since the beam hole losses increase and the energy error term in Eq. (5-18) and Eq. (5-19) becomes large.

A method to determine x and Q^2 from the hadronic system was proposed by F. Jacquet and A. Blondel [58] and is based on ep kinematics only. The four-momentum X

that describes all outgoing hadrons can be written as

$$X = \begin{bmatrix} E_H \\ \sum p_x \\ \sum p_y \\ \sum p_z \end{bmatrix}, \tag{5-20}$$

where E_H is the total hadronic energy. From Eq. (5-6) and Eq. (5-8), a useful relation is

$$Q^2 = \frac{p_T^2}{1-y} = \frac{\left(\sum_{hadrons} E_i \sin\gamma_i\right)^2}{1-y}. \tag{5-21}$$

For the hadronic vertex, p_T is just the total hadronic transverse momentum summed over all the final state hadrons. The four-momentum transfer at the hadronic vertex is $q = X\text{-}p$, and from Eq. (5-8), y can be expressed as

$$y_{JB} = \frac{p \cdot (X-p)}{k \cdot p} = \frac{E_H - \sum p_z}{2E_e}, \tag{5-22}$$

and x can be determined using the relation

$$Q^2 = sxy. \tag{5-23}$$

The model-independent Jacquet-Blondel method does not make any assumption on the internal structure of the proton. It makes no distinction between hadrons coming from different jets and works for multijet events, hence one does not have to deal with the problem of jet definition. In Eq. (5-21), γ_i is the polar angle of the ith hadron. For a given energy, the y contribution of a hadron close to the forward beam pipe increases as γ^2. Thus, the influence of target jet particle losses in the forward beam hole is small.

5.1.3 Mixed Method

In this method, the strengths of both the electron and hadronic methods are combined. The electron gives an excellent Q^2 determination in Eq. (5-13) even at small y

since it is based mainly on the scattered electron angle determination. The electron Q^2 measurement is complemented by the y measurement from the hadrons in Eq. (5-22). Using the relation in Eq. (5-23),

$$x_{mixed} = \frac{Q^2_{elec}}{sy_{JB}}. \tag{5-24}$$

The systematic shifts of $Q^2{}_{elec}$ and y_{JB} are only linearly dependent on the measurement errors of the scattered electron energy and hadronic energy respectively. From Eq. (5-24), the systematics on the electron and hadronic energy scales (ε_e and ε_h), in the worst case, can add up such that $\delta x_{mixed} = \varepsilon_e + \varepsilon_h$.

5.1.4 Double Angle Method

This approach [60] is motivated by the observation that angles are more accurately measured than energies in the ZEUS detector. For the bare quark-lepton kinematics in Figure 5-1, the conservation of energy and momentum requires

$$\begin{aligned} xp + E_e &= E'_e + E_J \\ xp - E_e &= E'_e \cos\theta_e + E_J \cos\gamma \\ E_e \sin\theta_e &= E_J \sin\gamma \end{aligned} \tag{5-25}$$

assuming that the rest masses of the quarks and the electron are negligible. The final electron energy can be obtained from Eq. (5-25) in terms of the angles θ_e and γ,

$$E'_e(\theta_e,\gamma) = \frac{2E_e \sin\gamma}{\sin\gamma + \sin\theta_e - \sin(\gamma+\theta_e)}. \tag{5-26}$$

where γ is the angle of a massless object which balances the electron momentum and satisfies the four-momentum conservation in Eq. (5-25). The scattered electron energy can then be determined from the two scattering angles independent of the energy calibration of the detector. The kinematical variables can then be written in terms of θ_e and γ by substituting Eq. (5-26) for E'_e in Eq. (5-6)-Eq. (5-8),

$$Q^2(\theta_e,\gamma) = \frac{4E_e^2 \sin\gamma(1+\cos\theta_e)}{\sin\gamma + \sin\theta_e - \sin(\gamma+\theta_e)} \tag{5-27}$$

$$x(\theta_e,\gamma) = \frac{E_e}{E_p}\left[\frac{\sin\gamma + \sin\theta_e + \sin(\gamma+\theta_e)}{\sin\gamma + \sin\theta_e - \sin(\gamma+\theta_e)}\right] \tag{5-28}$$

$$y(\theta_e,\gamma) = \frac{\sin\theta_e(1-\cos\gamma)}{\sin\gamma + \sin\theta_e - \sin(\gamma+\theta_e)}. \tag{5-29}$$

The struck quark scattering angle, γ, is obtained from the hadronic flow measurement. From the above equations, γ can be written in terms of y and Q^2 as

$$\cos\gamma = \frac{Q^2(1-y) - 4E_e^2y^2}{Q^2(1-y) + 4E_e^2y^2}. \tag{5-30}$$

To obtain the cos γ measurement, the Jacquet-Blondel variables which are well suited to suppress the effect of the fragmentation particle losses are used, giving

$$\cos\gamma = \frac{(\sum p_x)^2 + (\sum p_y)^2 - (\sum E - p_z)^2}{(\sum p_x)^2 + (\sum p_y)^2 + (\sum E - p_z)^2}. \tag{5-31}$$

Although the determination of γ is based on hadronic energies, this dependence is small since it is a ratio of energies. A miscalibration of the hadronic energy scale will not be a big contribution, while the error in the electron energy scale can be ignored.

5.2 Smearing and migration effects

Measurement errors and detector smearing on the final state angles and energies introduces shifts in x, y and Q^2 compared to the true values. The effect of detector smearing on the reconstruction of the kinematical variables is illustrated in Figure 5-4. For the events shown, a reconstructed electron energy of at least 5 *GeV* was required. It can be seen that detector smearing effect on the measurement of Q^2 is relatively small, except in the Jacquet-Blondel method. The resolution for all methods degrades noticeably at the low Q^2 region. The performance of the different reconstruction methods is thus determined by the x resolution. The smearing effect on the reconstruction of x as well as y is worst for the electron method as expected.

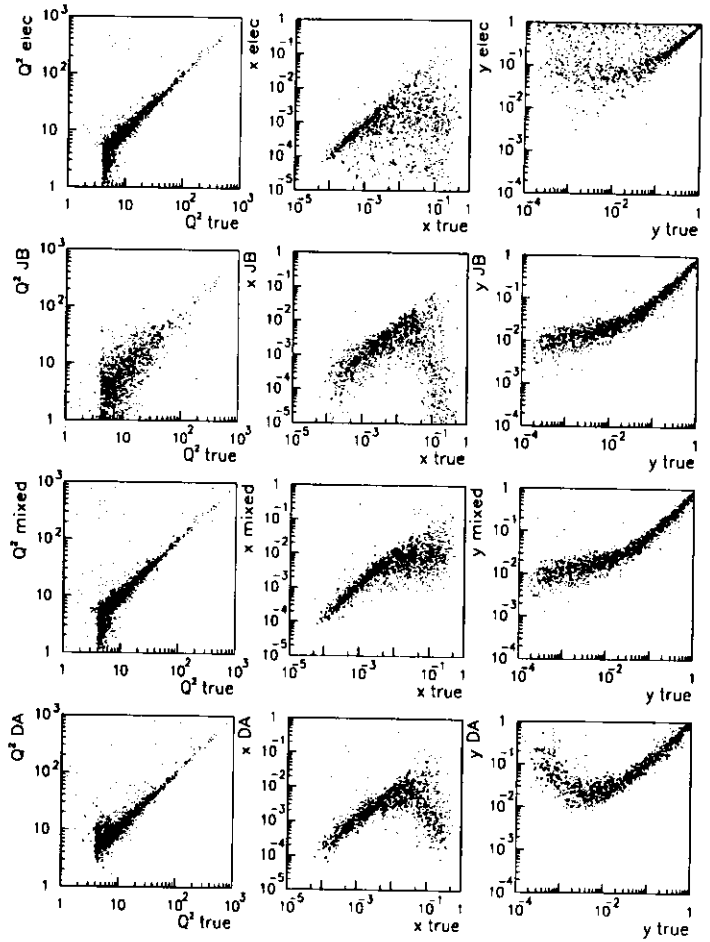

Figure 5-4 Smearing effects on the reconstruction of kinematical variables shown for the electron, Jacquet-Blondel, mixed, and DA methods.

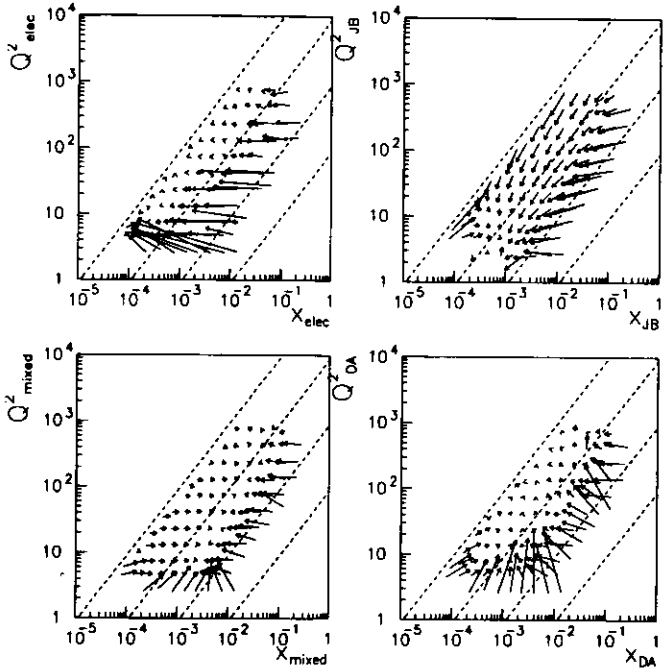

Figure 5-5 The migration of events due to measurement errors for different reconstruction methods is shown. The tail of the arrow is at the average value of the true x, Q^2 and the head of the arrow is at the average value of the reconstructed x, Q^2. A minimum of 20 events was required in each bin. The dashed lines are lines of constant y values 1.0, 0.1, 0.01 and 0.001.

Due to measurement errors, the observed event rate in a given x and Q^2 bin differs from the true event rate. A fraction of events have migrated into the bin from adjacent bins while another fraction has migrated out. In Figure 5-5, the x and Q^2 phase space was divided such that there were four bins per decade in x and Q^2. A cut ($y_{true} > 0.005$) to suppress calorimeter noise effects was applied in addition to the electron energy requirement. The event migration is shown for the four different reconstruction methods.

Figure 5-4 and Figure 5-5 show that the extent of the smearing and migration effects in the x and Q^2 bins varies with the choice of the reconstruction method. It is also dependent on the detector resolution and whether there is an additional photon in the final state as shown in the following section.

5.3 Radiative Effects

Radiative processes where a real photon is emitted from the lepton line shown in Figure 5-1 leads to a shift of the reconstructed kinematical variables. In the case of initial state radiation (ISR), the photon emitted collinear with the initial electron is lost in the beam pipe. The effective energy of the incident electron is lower than the nominal electron beam energy by E_γ, the energy of the emitted photon. In most cases, the photons in final state radiation (FSR) processes are emitted at small angles relative to the scattered electron. The final electron energy effectively includes the emitted photon energy. Hence, the measured variables x, Q^2 would be closer to the true x, Q^2. Denoting the nominal and true final electron energies by E_0 and E respectively, the square of the momentum transfer defined at the lepton vertex is

$$\text{ISR}: \quad Q^2_{rad} = 2(E_0 - E_\gamma) E (1 + \cos\theta_e) \tag{5-32}$$

$$\text{FSR}: \quad Q^2_{rad} = 2E_0 (E + E_\gamma) (1 + \cos\theta_e) \tag{5-33}$$

and similarly for y,

$$\text{ISR}: \quad y_{rad} = 1 - \frac{E}{2(E_0 - E_\gamma)} (1 - \cos\theta_e) \tag{5-34}$$

$$\text{FSR}: \quad y_{rad} = 1 - \frac{E + E_\gamma}{2E_0} (1 - \cos\theta_e) \tag{5-35}$$

While Q^2_{rad} can either be smaller or larger than Q^2_{elec} in Eq. (5-6), $y_{rad} < y_{elec}$ and it can be shown that $x_{rad} > x_{elec}$ for both initial and final state radiation processes. Radiative effects can get large if one reconstructs the kinematics using the electron variables (refer to Sec. 8.3 on radiative corrections to the Born cross section).

5.4 Noise Effects

The contribution of noise[1] to the measured energy is caused by the fluctuations of the uranium noise (UNO) signal in the calorimeter cells (see Sec. 3.8.6). In Table 5-1, the

FEMC	FHAC	BEMC	BHAC	REMC	RHAC
19.0	26.0	16.0	30.0	18.0	26.0

Table 5-1 Noise levels in *MeV*/cell for different calorimeter cell types [61].

noise levels for the different calorimeter cell types are listed. The noise level in the calorimeter, summed over all 11836 channels, is given by the average width of the distribution shown in Figure 5-6 and is about 2 *GeV*. Since this is not a negligible contribution, the effects of noise on the reconstruction of the kinematical variables was considered. Two Monte Carlo samples, which were identical except that one simulated noise, were used to study these effects.

The number of cells included in the measurement of angles is increased with the addition of noise. For the hadrons travelling in the forward direction, this increase in the number of cells is not symmetric due to the presence of the beam pipe in the center of the FCAL. Hence, one measures a larger scattering angle for the current jet. This is true also for the electrons, but since they are more localized, the measured scattering angle is only slightly affected. For the different methods, the effect of noise on reconstructing y can be seen by comparing the top and bottom scatter plots in Figure 5-7, for the sample without and with noise simulation respectively. Noise has a negligible effect on the measurements of the electron energy and angular position. The hadronic variables, on the other hand, are particularly sensitive to noise in the very small y region. The effect is seen in the migration

1. At ZEUS, the effects of calorimeter noise on the determination of the kinematic variables are minimized by applying an energy cut of 60 *MeV* for EMC cells and 110 *MeV* on HAC cells. The effect of calorimeter noise is simulated in the MC.

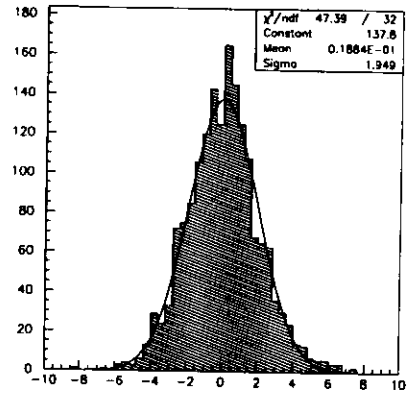

Figure 5-6 Noise contribution to the total calorimeter energy in *GeV* is shown without cell energy cuts applied. To minimize noise effects in the determination of the kinematic variables, an energy cut of 60 *MeV* on EMC cells and 100 *MeV* on HAC cells are applied in all physics analyses at ZEUS.

of the events at low y (high x) values to higher y for all the reconstruction schemes using hadronic information. The effect on the Q^2 measurements is negligibly small except for the Jacquet-Blondel method.

5.5 Choice of the reconstruction method

The preceding sections have shown that the *ep* kinematics can be determined from the electron and hadronic measurements. Combinations of the leptonic and hadronic energies and angles as in the mixed and double angle methods extend the measurable phase space and allow a more precise determination of the kinematical quantities x, Q^2. Given the present understanding of the electron energy calibration, the dependence of these kinematical quantities on the measurement errors of the scattered electron energies and angles does not favor the use of the electron and the mixed reconstruction methods. The dependence of the kinematical quantities on the measurement errors of the hadronic

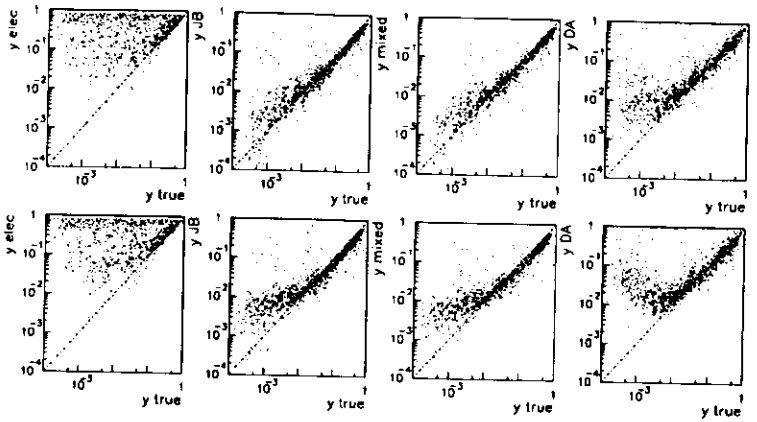

Figure 5-7 For the different methods, plots of the reconstructed y versus y_{true} for the MC sample without (top) and with noise simulation (bottom).

energies and angles also rule out the jet reconstruction and the Jacquet-Blondel methods. The double angle method derives the event variables x, Q^2 from the scattering angle of the outgoing electron and the angle of a massless object, obtained from the hadron flow measurement, which balances the electron momentum to satisfy four-momentum conservation. Although the DA variables are quite sensitive to noise effects at low values of y (as shown in Figure 5-7), the method is less sensitive to the scale errors in the measurement of the energies of the final state particles. Therefore, the reconstruction method used in this analysis is the double angle (DA) method.

CHAPTER 6

UNDERSTANDING THE HADRONIC ENERGY SCALE

Due to detector effects such as inactive material, beam hole, and calorimeter boundaries, the measured energies are in general lower than the true (generated) values in the Monte Carlo (MC). The loss in the hadronic transverse momentum as well as the hadronic E-pz is about 15-20% as shown in Figure 6-1. In order to understand where this deficiency is coming from, a study was done to estimate how much of the loss is due to the inactive material in front of the calorimeter and the energy leakage into the beam hole [62]. This will be discussed in the next section.

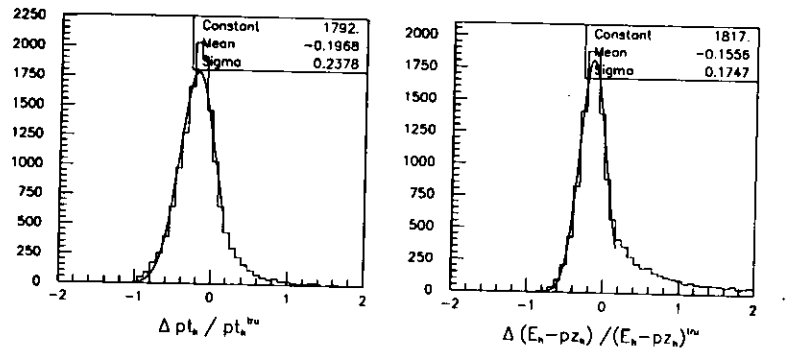

Figure 6-1 Plots of $(p_T^{rec}-p_T^{true})/(p_T^{true})$ and $(\delta_h^{rec}-\delta_h^{true})/(\delta_h^{true})$ for the DIS NC MC sample with inactive material after cuts. Note the tail in the δ_h plot which is due to the effect of noise.

In this study, the MC sample discussed in Sec. 4.1 was used. To select only the DIS events, the final selection criteria as discussed in Sec. 7.4.3 were applied to the MC

sample. An additional requirement that the scattered electron is correctly identified was used to ensure that there is no contamination from the misidentification of electrons in the reconstruction of the hadronic energies and momenta. From an initial sample of 50k events, 15k remain after the selection criteria are applied. These events were then used in determining the corrections to the hadronic variables.

Figure 6-2a shows the ratio of the hadronic *E-pz* to the total *E-pz* plotted for the data and the MC. In general, this ratio is lower in the data than the MC but they agree to within 10% for most of the phase space as shown in Figure 6-2b. The hadronic corrections do not correct for any disagreement between the data and the MC simulation.

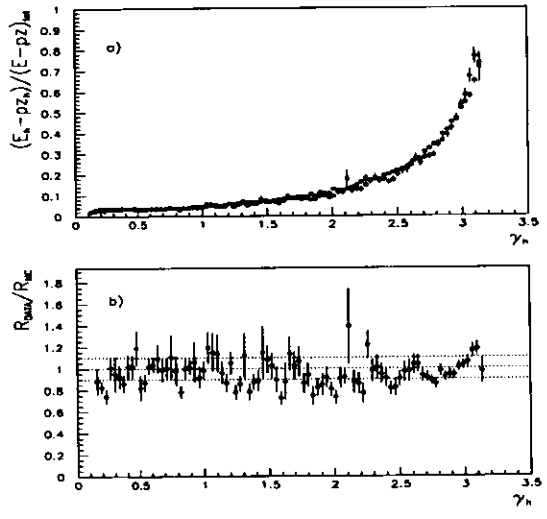

Figure 6-2 Comparison between Fall '92 data and DIS MC (open circles) with MTB1 parton parametrizations. The ratio of hadronic to total *E-pz* (plotted vs. γ_h in radians) is in general lower in the data than the MC. In b) the ratio for the data is divided by the ratio for the MC. The agreement is within 10% (dotted lines) for most of the phase space.

6.1 Hadronic Energy Losses from Various Effects

For hadrons close to the forward beam pipe, the quantity δ_h given by

$$\delta_h = \sum_{hadrons} E_i - pz_i = \sum_{hadrons} E_i(1-\cos\gamma_i) \tag{6-1}$$

is negligible for any given energy. In the rear region however, this contribution is approximately twice the energy of the particle. Energetic particles which escape undetected in the rear beam hole would thus lead to a large error in the measurement of δ_h. Figure 6-3 shows the difference between the measured and true δ_h in the MC as a function of the measured parton direction γ_h. Here, γ_h is the scattering angle of the struck quark given by (see Sec. 5.1.4)

$$\cos(\gamma_h) = \frac{\left(\sum_{hadrons} p_x\right)^2 + \left(\sum_{hadrons} p_y\right)^2 - (\delta_h)^2}{\left(\sum_{hadrons} p_x\right)^2 + \left(\sum_{hadrons} p_y\right)^2 + (\delta_h)^2}. \tag{6-2}$$

For events where the beam hole losses are not small, y_{JB} would be reconstructed lower than the true *y*. Q^2_{JB} is inversely proportional to (1-y_{JB}), hence its reconstruction is also affected. Since hadrons lost in the beam pipe do not contribute significantly to the transverse momentum p_T, the effect of the beam hole losses on p_T measurements should be negligible. At low values of *x*, γ_h is measured mostly towards the rear region as shown in Figure 6-4. It is in this region that it is important to correct for the hadronic energy losses.

The depth of the inactive material in radiation lengths (X_0) is shown in Figure 4-1 as simulated in the ZEUS MC as a function of the polar angle. It can be seen that in the region near the rear calorimeter (RCAL) beam pipe, there is up to 6 X_0 of dead material in front of the calorimeter. The effect of the inactive material in the RCAL region in the δ_h calculation is small compared to the loss of hadronic energy in the beam hole. To study the effect of the hadronic energy loss due to inactive material in the detector on the measurement of the hadronic p_T, a MC sample of 10k events was generated wherein the dead material was not simulated. A comparison was made with the same events with and without the inactive material in front of the calorimeter. After applying the same selection criteria, less than 3k events remain. Similar plots as shown previously in Figure 6-1 for the sample with the inactive material are now shown for the MC sample without the inactive

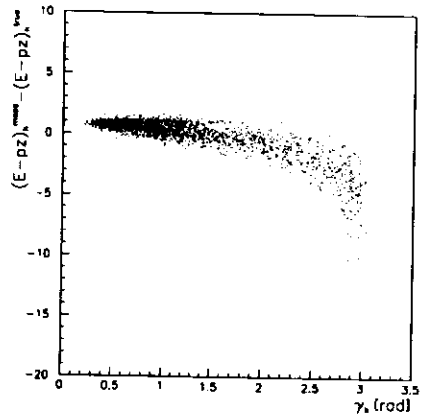

Figure 6-3 Scatter plot of the difference between the measured and true δ_h in *GeV* as a function of γ_h in radians.

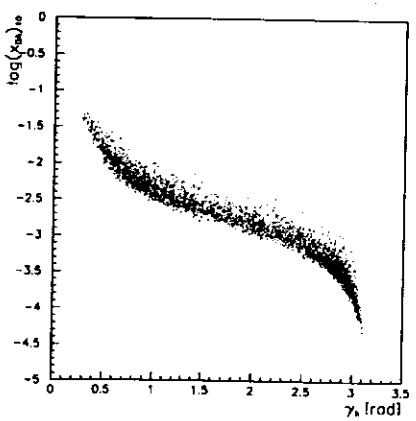

Figure 6-4 Scatter plot of the reconstructed x_{DA} as a function of γ_h. For small values of x, the hadronic activity due to the current jet is seen mostly in the rear (RCAL) region.

material in Figure 6-5. The first plot shows that the inactive material does not completely explain the error in the measurement of the hadronic transverse momentum p_T. The second plot shows that the mismeasurement in δ_h is not primarily due to the inactive material. Also note that there is no tail in the δ_h plot since this MC sample did not have simulated calorimeter noise.

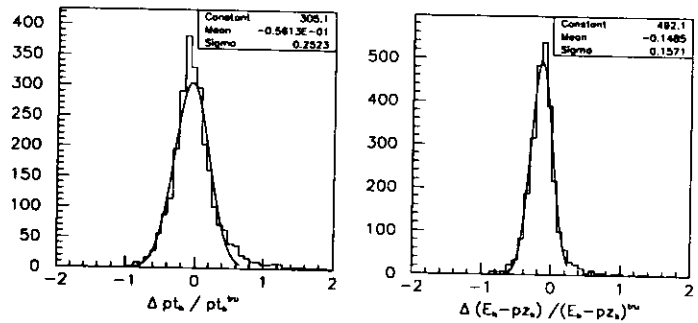

Figure 6-5 Plots of $(p_T^{rec}-p_T^{true})/p_T^{true}$ and $(\delta_h^{rec}-\delta_h^{true})/\delta_h^{true}$ for the NC MC sample without the inactive material. The noise was not simulated in the sample and thus there is no tail in δ_h seen in Figure 6-1.

6.2 Method of determining the hadronic corrections

Corrections to the hadronic variables p_T and δ_h were determined since they are used directly or indirectly in all kinematic reconstruction methods except the electron method. Thus, one ends up with only one set of corrections which would improve the x, y and Q^2 resolutions of the Jacquet-Blondel, mixed and double angle reconstruction methods. To obtain the true values of p_T and δ_h in the MC simulation, the following equations were used:

$$(p_T^2)^{true} = (Q^2)^{true}(1-y^{true})$$
$$\delta_h^{true} = 2E_e y^{true} \qquad (6\text{-}3)$$

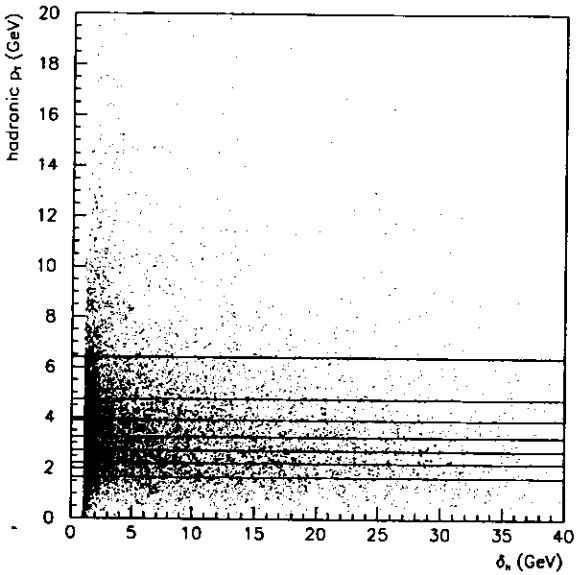

Figure 6-6 Scatter plot of the phase space defined by the hadronic variables p_T and δ_h. Selected events were binned so that each bin would have approximately the same number of events. The p_T bins shown here are at 1.65, 2.2, 2.7, 3.25, 3.9, 4.75, 6.4 *GeV*.

For events with initial state radiation, the electron beam energy $E_e = 26.7\ GeV$ is replaced by E_e-E'_γ, where E'_γ is the radiated photon energy. The events remaining after selection cuts are divided into 8 bins in p_T such that each bin would have roughly the same number of events. This is shown in Figure 6-6. The average values of the difference between the measured and true δ_h are plotted as a function of $log_{10}(\delta_h)$ in increasing p_T bins as shown in Figure 6-7. The average values of the difference between the measured and true p_T as a function of $log_{10}(p_T)$ in increasing δ_h bins are shown in Figure 6-8.

Figure 6-7 and Figure 6-8 show that it is not sufficient to scale hadronic energies by a constant factor. For large values of γ_h, the hadrons are going towards the RCAL

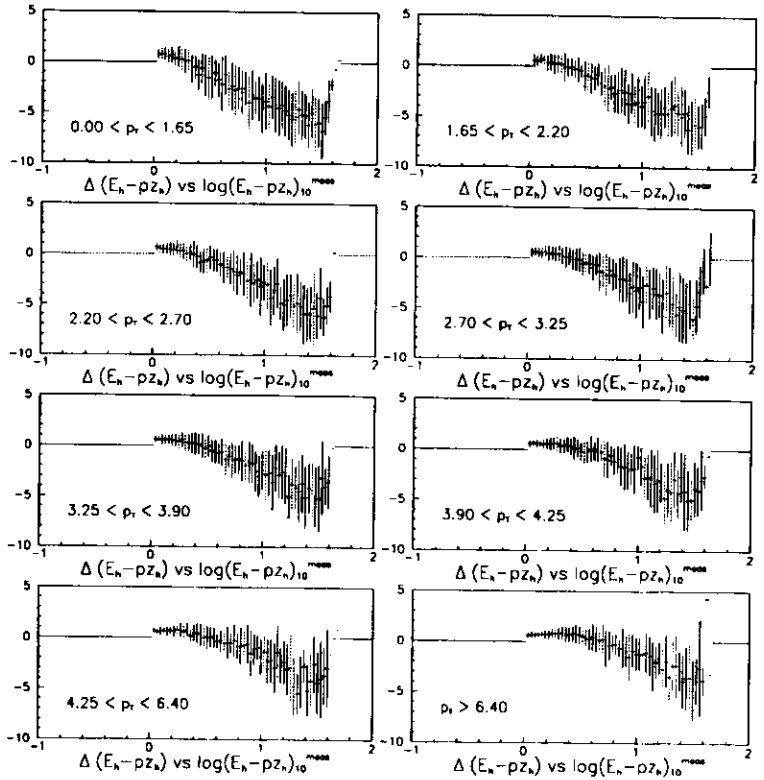

Figure 6-7 Profiles of the difference between the measured and true δ_h versus $log_{10}(\delta_h)$ in increasing bins of p_T.

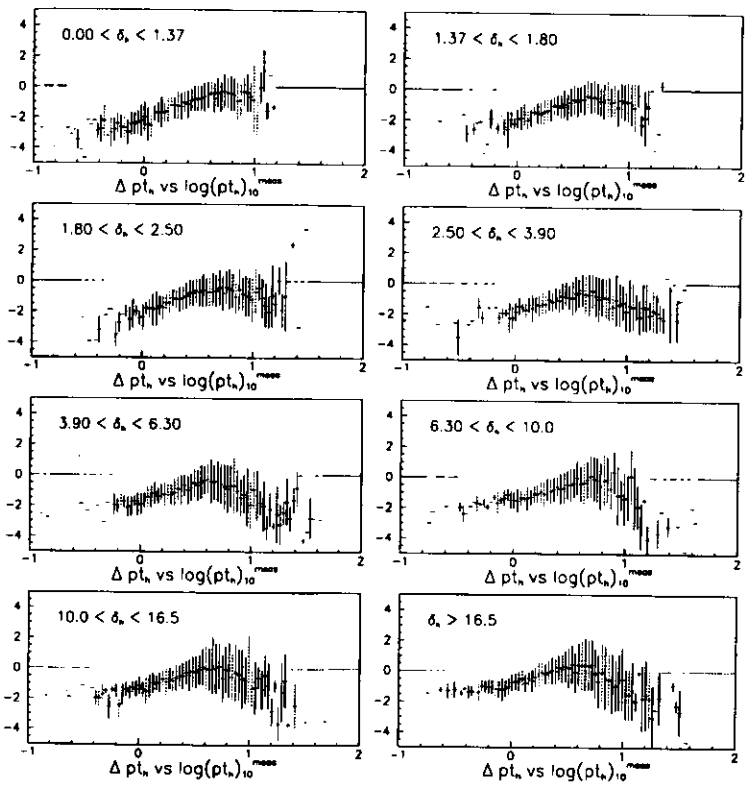

Figure 6-8 Profiles of the difference between measured and true hadronic p_T versus $log_{10}(p_T)$ in increasing bins of δ_h.

region where some of the hadrons might escape undetected down the rear beam pipe. For these events, the hadronic corrections are larger compared to those events where the hadrons are going in the forward direction. Note that δ_h is overestimated in the forward region. This is due to calorimeter noise which has been simulated in the sample with the inactive material simulated.

Each of the profile plots in Figure 6-7 was re-plotted: events which are outside one standard deviation from the mean were removed to make sure that averages are not pulled by badly reconstructed events. A minimum number of events was required for each point. To obtain the δ_h corrections, each of the new profile plots was fitted with a functional form

$$a_i \cos\left[b_i \log\left(\delta_h\right)_{10}\right] - c_i \tag{6-4}$$

where a_i, b_i, and c_i are the fit parameters for the ith p_T bin. The fit parameters are then parametrized as functions of p_T. For example, the parametrization of the fit parameters b_i is shown in Figure 6-9. An example of a fit to δ_h is shown in Figure 6-10 a.

The function chosen to fit the δ_h profiles does not work very well when δ_h is large. A smaller second correction is necessary for these events. This correction was obtained by fitting a second degree polynomial to a profile plot of $\Delta\delta_h$ versus the measured δ_h. The final corrected δ_h is given in Eq. below.

$$\delta_h^{COR} = P(\delta_h, p_T) - C_2(\delta_h, p_T) \tag{6-5}$$

where P and C_2 are given by

$$\begin{aligned} P &= \delta_h - C_1 \\ C_1 &= 2.25\cos\left(B\log\left(\delta_h\right)_{10}\right) - 1.5 \\ C_2 &= 0.06197 - 0.02296P - 0.002323P^2 \\ B &= 1.45 + 1.887exp\left(-0.251p_T\right) \end{aligned} \tag{6-6}$$

A similar procedure could be done to obtain the hadronic p_T corrections. However, another way to obtain corrections to p_T is to use the correlation between Δp_T and the measured δ_h. Using this correlation method, the final corrected p_T is given in Eq. (6-7). Again, a second smaller correction is performed by fitting a polynomial to a profile plot of Δp_T versus the measured p_T, resulting in

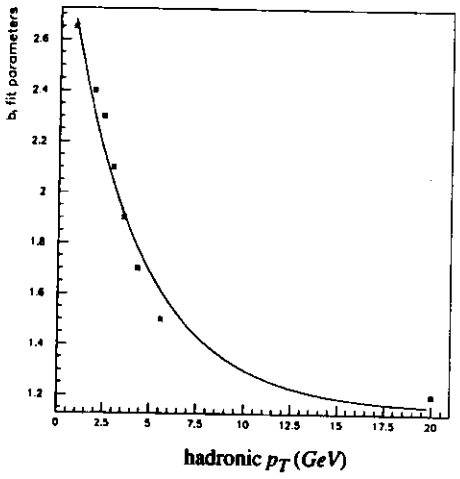

Figure 6-9 Parametrizing the fit parameters obtained from fitting the δ_h profile plots.

$$(p_T)^{COR} = G_1 - G_2$$
$$G_1 = p_T + 1.406 - 0.036\delta_h \qquad (6\text{-}7)$$

where G_2 is given by a sixth degree polynomial in p_T. The fit parameters are -8.221×10^{-1}, -1.087×10^{-1}, 3.413×10^{-1}, -8.474×10^{-2}, 8.39×10^{-3}, -3.768×10^{-4}, and 6.356×10^{-6} in increasing powers of p_T as shown in Figure 6-10b. The second corrections C_2 and G_2 are only valid for $\delta_h \leq 30\ GeV$ and $p_T \leq 20\ GeV$ respectively; very few events in the sample lie above these limits.

6.3 Discussion

In the forward region there is an overestimate in δ_h due to the effect of the calorimeter noise. The hadronic corrections will move these events back to the lower y_{JB} region. The results are shown in Figure 6-11 and Figure 6-12 after applying these corrections to events passing the selection criteria, and reapplying the y_{JB} requirement (see Sec. 7.4.3). Also shown are comparisons of the fractional resolutions $\Delta x/x$ versus

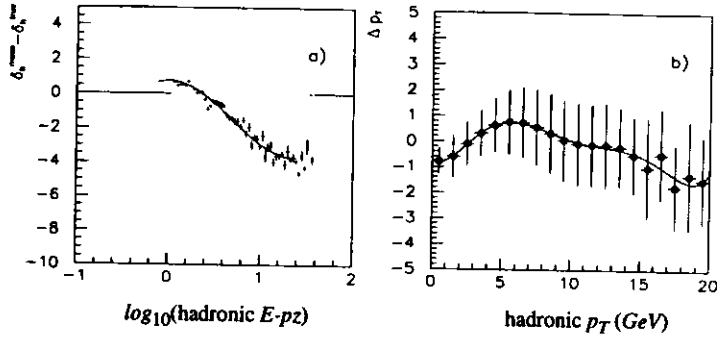

Figure 6-10 Hadronic energy corrections. a) An example of a fit with $a_i \cos[b_i \log_{10}(\delta_h)] - c_i$. For the δ_h fits, the parameters a_i and b_i are the same for all bins of p_T, given by 2.25 and -1.5 respectively. b) The second p_T correction using a polynomial fit.

$log_{10}(x)$ and $\Delta Q^2/Q^2$ versus $log_{10}(Q^2)$ in the Jacquet-Blondel, mixed, and double angle reconstruction methods. Although the statistics are limited in determining these corrections, the results are quite good. The event migration in the x and Q^2 phase space is reduced, and the purity in the bins is improved. The profile histograms in Figure 6-11 and Figure 6-12 are binned in p_T and δ_h respectively. In Figure 6-13, the systematic shifts in the resolutions of x and Q^2 have been corrected for all methods shown.

At HERA, it is important to understand the kinematics in the low x region. It is therefore necessary that the hadronic energy scale be understood and the hadronic energy measurements be corrected for any substantial loss due to the inactive material or detector acceptance (beam hole).

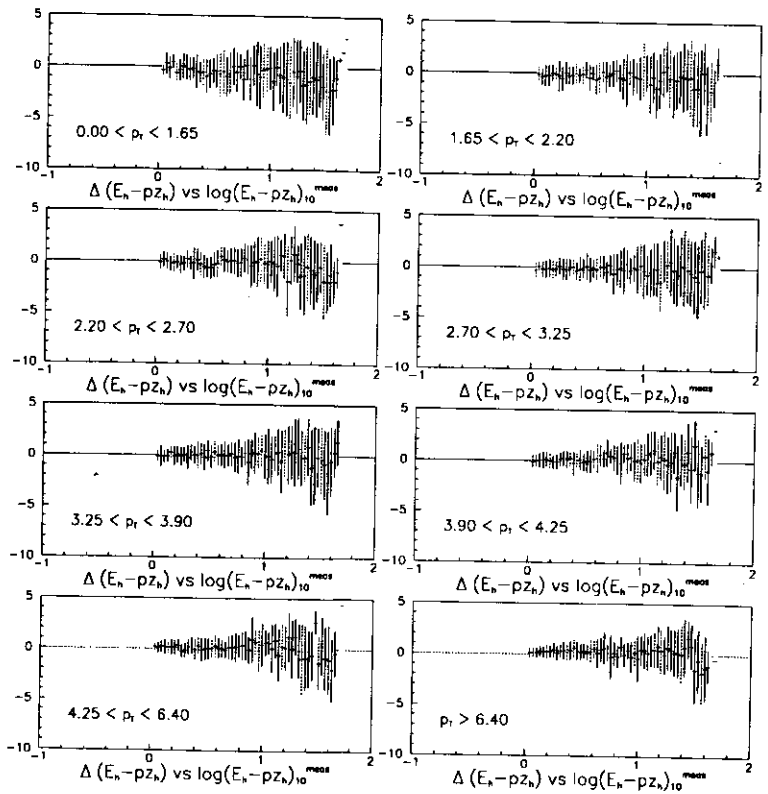

Figure 6-11 Profiles of the difference between the measured /corrected and true δ_h versus $log_{10}(\delta_h)$ in increasing bins of p_T after applying the corrections.

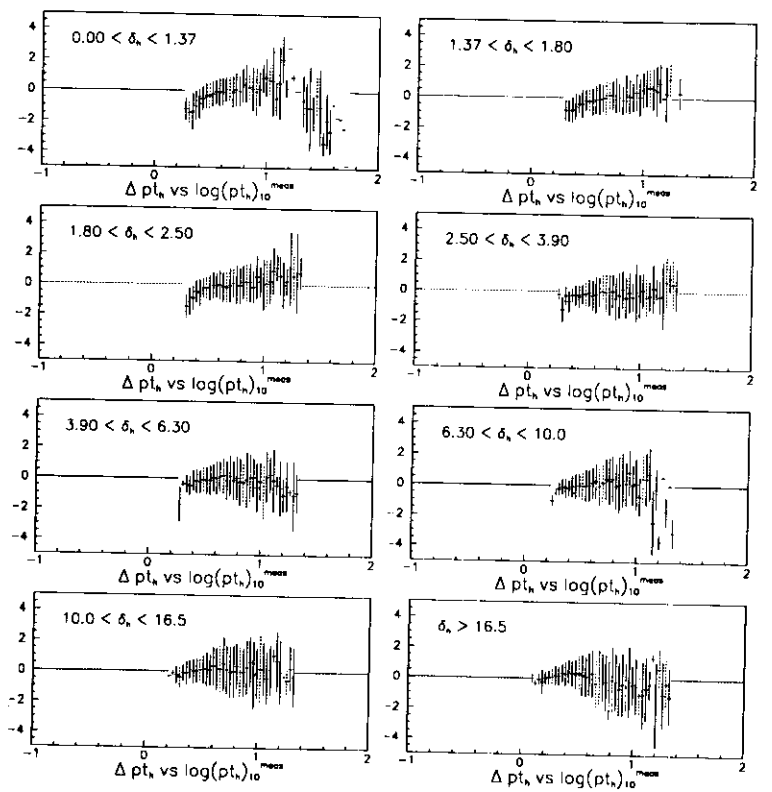

Figure 6-12 Profiles of the difference between the measured/corrected and true p_T versus $log_{10}(p_T)$ in increasing bins of δ_h after applying the corrections.

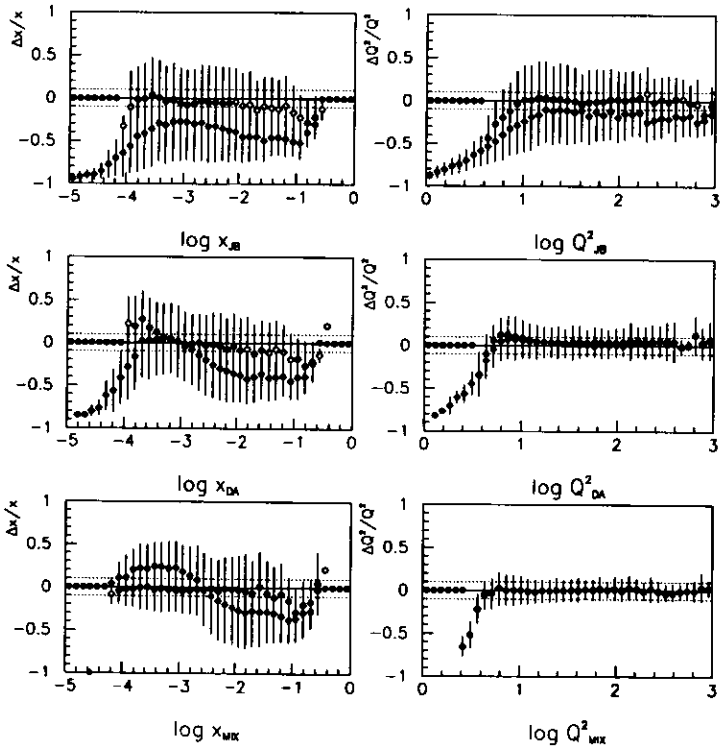

Figure 6-13 The fractional resolutions in x and Q^2 for the Jacquet-Blondel, mixed, and double angle reconstruction methods. The dark and open circles represent before and after hadronic corrections, respectively.

CHAPTER 7

THE DATA SAMPLE

This chapter begins with a discussion on the measurement of the luminosity and the systematic uncertainties involved. An essential tool in the identification of neutral current events is the electron finder. In Sec. 7.2 the electron finding and electron position reconstruction algorithms used in this analysis are described. Three finders are compared in terms of their efficiencies and purities. The simulation of the vertex distribution in the MC simulation is described in Sec. 7.3. This is necessary to understand the efficiencies and acceptances of the trigger and the event selection. In addition the vertex obtained using the calorimeter time and how it can be used to determine a z-vertex for events with no tracks in the CTD are also discussed. The next section describes the physics filter and the selection criteria used to separate the DIS events from background, and to obtain a fiducial sample of well measured neutral current candidates. About 4.2 million events were accumulated with the ZEUS detector in the Fall 1992 running period, of which a final sample consisting of 2365 events is retained after all the selection criteria are applied. The main source of background for DIS events after a preselection, is from photoproduction. These events are characterized by an electron scattered at very small angles down the beam hole. A photon or a charged pion may be mistakenly reconstructed as the outgoing electron and contaminate the DIS sample. Estimates of the remaining background events in the final sample due to photoproduction as well as cosmics, beam-gas and Compton events are addressed in Sec. 7.5. The final sample also contains a contribution from events with a large pseudorapidity gap in the final hadronic state. The observation of these events are discussed in Sec. 7.6. Finally the last section presents distributions of the final event sample and the comparison with the MC simulation.

7.1 Luminosity Measurement

For the luminosity measurement, the bremsstrahlung process $ep \rightarrow ep\gamma$ has been chosen because of its well defined experimental signature and the precise knowledge of its

cross section. The final state electron and the bremsstrahlung photon are emitted at small angles relative to the electron beam direction and have energies adding up to the electron beam energy. They are detected in the LUMI electromagnetic calorimeters (see Sec. 3.5.1) in coincidence. The integrated luminosity, $\mathcal{L}_{ep}$, is determined using the formula

$$\mathcal{L}_{ep} = \frac{R_{ep}}{\sigma_o} \tag{7-1}$$

where R_{ep} is the measured rate of ep bremsstrahlung and the expected cross section, σ_o is of the general form

$$\sigma_o = \int A_{LUMI}\, d\sigma_{theor} \tag{7-2}$$

integrated over the phase space of the LUMI detector acceptance, A_{LUMI}. The theoretical cross section, σ_{theor}, calculated using the Bethe-Heitler formula [63], is corrected for experimental effects such as limited detector acceptance and energy smearing.

At HERA, the bremsstrahlung of the beam electrons in the residual gas in the beam pipe, $eA \rightarrow eA\gamma$, gives rise to a significant background in the luminosity measurement. Its experimental signature is indistinguishable from the ep bremsstrahlung process $ep \rightarrow ep\gamma$ and its cross section 5-7 times larger [64]. The contribution due to this background, R_{egas}, can be obtained by measuring the bremsstrahlung rate from the electron pilot[1] bunch, R_{pilot}, as

$$R_{egas} = R_{pilot}\frac{I^e_{tot}}{I^e_{pilot}} \tag{7-3}$$

where I^e_{pilot} is the current in the pilot bunch, I^e_{tot} is the total electron current. In addition to the electron gas background, there is also a contribution[2] from the collisions of the secondary electron bunches, called satellite bunches, with the proton beam. These bunches

1. During the Fall 1992 running period, nine consecutive electron bunches collided with nine proton bunches. An additional electron bunch (pilot bunch) was used to estimate the background rate due to the bremsstrahlung of beam electrons on the residual gas.

2. The contribution of the electron satellite bunch was determined from the measurement of the timing distributions of the proton and electron bunches at HERA using the C5 collimator described in Sec. 3.6.

were observed trailing the primary electron bunch by 8 ns. The RCAL time distribution for the 1992 Fall data showing the contribution of beam-gas events as well as events with ep collisions coming from the satellite bunches can be seen in Figure 7-1. Since the selection criteria applied to remove beam-gas background on-line strongly suppresses

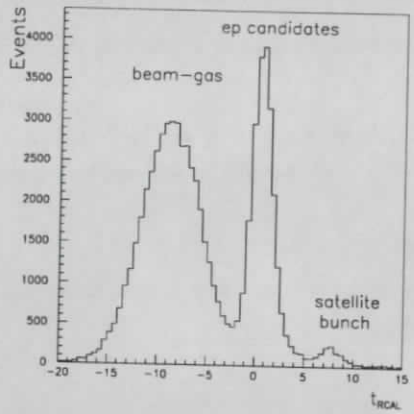

Figure 7-1 RCAL time distribution for the Fall 1992 data sample showing beam-gas, ep candidates and satellite bunch contributions.

these ep collisions coming from the satellite bunch, the contribution from these events must be properly taken into account in calculating the luminosity. The correction to the Fall 1992 integrated luminosity due to the contribution of the satellite electron bunch is determined to be ~ 6% [65]. To obtain the corrected ep bremsstrahlung rate, R_{ep}, the background due to electron gas bremsstrahlung and satellite bunch contributions, $R_{satellite}$, are subtracted from the measured total rate, R_{tot},

$$R_{ep} = R_{tot} - R_{egas} - R_{satellite}. \tag{7-4}$$

In the Fall 1992 running period the average total bremsstrahlung rate was about 5 KHz and the electron gas contribution was typically 30% of the total rate.

The estimates (in percentage of the integrated luminosity) for each source of systematic uncertainty in the determination of the ZEUS integrated luminosity are listed below [61]:

- a 1.5% uncertainty in the determination of the electron gas bremsstrahlung contribution
- a 1% uncertainty in the determination of the satellite bunch correction
- uncertainty on the energy scale calibration of the photon calorimeter is less than 2%
- event migration effects from calorimeter miscalibration is less than 1%
- a 1% uncertainty in the theoretical determination of the Bethe-Heitler cross section
- a 2-5% uncertainty on the γ-cal acceptance A_γ due to non zero beam crossing angles

A total systematic error of 5% on the ZEUS integrated luminosity is obtained when all these contributions are added in quadrature. After electron gas and satellite bunch corrections, the integrated luminosity obtained for the Fall 1992 running period is $24.73\ nb^{-1} \pm 5\%$.

7.2 Electron Finding and Position Reconstruction

The key signature of DIS neutral current events is the presence of the scattered electron in the detector. However, detecting it and determining its energy and position are non-trivial. Its identification is fairly efficient when the electron is reasonably isolated from the hadrons and other particles in the calorimeter as seen in Figure 7-2. This isolation is expected to some degree since the outgoing electron emerges opposite in the azimuthal direction to the current jet and balances its transverse momentum. The event kinematics determine the degree of isolation of the scattered electron. In particular, at small values of x, the hadrons from the current jet are in the vicinity of the scattered electron as illustrated in Figure 7-3.

A correct and sufficiently efficient algorithm is necessary to select a well measured sample of DIS events to be used in the structure function analysis. Three algorithms were chosen for comparison, denoted by A, B, and C. For all three algorithms, electron identification was based entirely on calorimeter information. B and C use different methods for identifying spatial energy depositions in the calorimeter. Finder A, based on

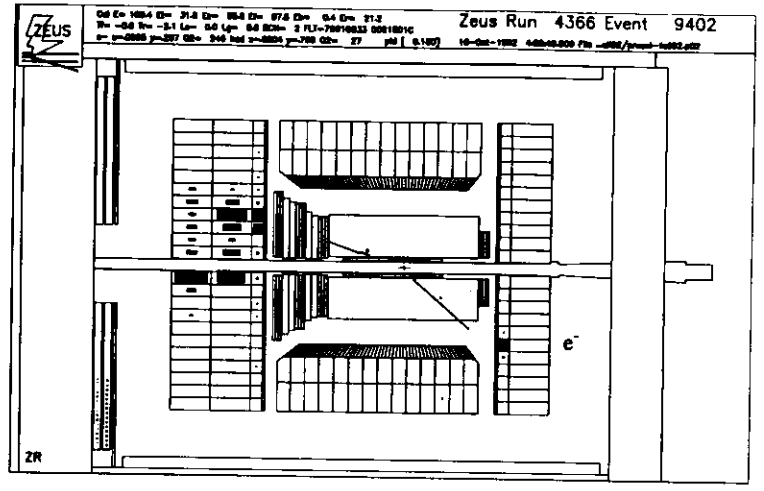

Figure 7-2 A neutral current event with an isolated scattered electron in the RCAL.

the same energy clustering algorithm as B, applies a cone search around electromagnetic cells with energies exceeding 1 *GeV*. For these cells, a quality factor is determined using the following quantities:

- energy imbalance between the signals from the two sides of the cell
- energy weighted radius of the EMC energy within a cone of half radius R_{inner}
- ratio of EMC energy in the region between R_{inner} and R_{outer} to EMC energy in R_{inner}
- HAC1 energy in the region between $R_{hacinner}$ and $R_{hacouter}$
- ratio of HAC1 energy within $R_{hacinner}$ to EMC energy within R_{inner}
- HAC2 energy in the region between $R_{hacinner}$ and $R_{hacouter}$
- ratio of HAC2 energy within $R_{hacinner}$ to EMC energy within R_{inner}

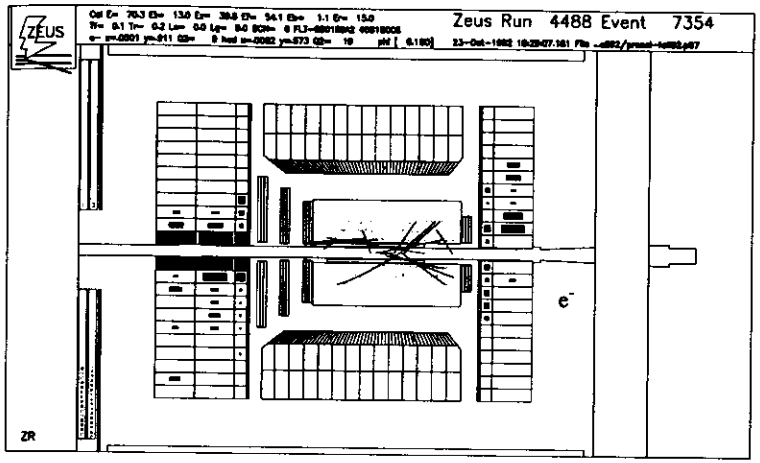

Figure 7-3 A low x event with hadronic activity from the current jet in the vicinity of the scattered electron.

where the cone half-angle sizes are defined as R_{inner}= 250 *mrad*, R_{outer}= 400 *mrad*, $R_{hacinner}$= 300 *mrad* and $R_{hacouter}$= 500 *mrad*. Cells which have quality factors exceeding some threshold value are considered as electron candidates. The separation of energy clusters arising from electromagnetic showers from those arising from hadronic showers is based on their distinct lateral and longitudinal energy distributions [45]. The criteria allows for larger lateral shower sizes for the electrons due to the amount of inactive material in front of the calorimeter. The criteria[1] are listed below:

- energy imbalance of the cell with the maximum energy is less than 0.2
- number of calorimeter cells comprising the electron candidate is less than 35
- the ratio of the HAC energy to the total energy of the electron candidate is less than 0.1
- the energy of the electron candidate is higher than 2 *GeV*.

1. The values given here are different for each of the electron finding algorithms discussed (Finders A, B, and C correspond to EEXOTIC, ELECT5, and LOCAL respectively.)

The energy of the candidate is given by the total calorimeter energy within $R_{hacinner}$. All of these criteria were determined by using various testbeam data and MC samples.

The percentage efficiencies and purities of the three electron finders A, B, and C are shown in Figure 7-4 as a function of the true electron scattering energy. The DIS neutral current MC sample described in Sec. 4.1 was used as input. Aside from a reconstructed electron in the event, the total energy minus the longitudinal energy in the calorimeter, $\delta = E_{tot}\text{-}P_z$, is within the range 35 $GeV \le \delta \le 60$ GeV was also required. This quantity, defined later in Sec. 7.4.2, is used to discriminate DIS events from backgrounds. Efficiency and purity are defined as follows:

$$Efficiency = \frac{\text{number of electrons correctly identified}}{\text{number of generated electrons}} \tag{7-5}$$

$$Purity = \frac{\text{number of electrons correctly identified}}{\text{number of electrons identified}}. \tag{7-6}$$

In terms of these two quantities, the ideal electron finder would have a high efficiency as well as purity. However, finder A which has the lowest efficiency is able to obtain a purer electron sample.

Photoproduction events often produce final state particles with electromagnetic showers which can be falsely identified as electrons. A sample consisting of MC photoproduction events generated using PYTHIA (discussed earlier in Sec. 4.2) was used in order to determine which electron finder has a lower background from photoproduction. The events which passed the δ requirement were assigned a weight to correspond to the total integrated luminosity. Figure 7-5 shows the cross section of the photoproduction background, picked up by finders A and B as a function of the cut on the reconstructed electron energy. For electron energies ~ 5 *GeV*, finder B picks up a factor of three more events in this sample. In order to minimize the uncertainties in the determination of the photoproduction background in the DIS event sample, finder A was used for electron identification in the measurement of the proton structure function.

For the reconstruction of the impact position of the scattered electron, a separate routine using energy sharing between the two sides of a calorimeter cell was used. The x-

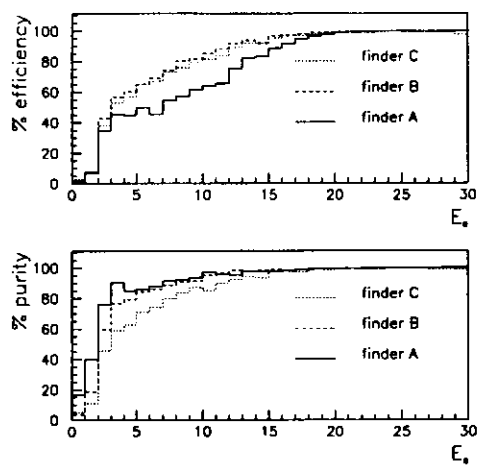

Figure 7-4 A plot showing comparison of the efficiencies and purities of three different electron finding algorithms plotted versus the generated electron energy.

position of the electron is determined from the energy imbalance of the calorimeter cell having the maximum energy. The energy imbalance is defined as the difference between the energies of the individual phototubes of the cell normalized by the total cell energy

$$imbalance = \frac{E_{left} - E_{right}}{E_{left} + E_{right}}. \qquad (7\text{-}7)$$

The electron impact position in x as a function of the cell energy imbalance was extracted using information from the HES silicon diodes installed in RCAL modules 12-14 during the Fall 1992 running period. For the central part of the cell ($\pm$ 7.5 *cm* from the center) with the maximum energy, this function has a linear dependence on the energy imbalance with a small polynomial correction. In the outer region, a quadratic dependence is chosen. The position in y is determined using the energy ratio $E_{vert} / (E_{vert} + E_{max})$, where E_{max} is the energy of the cell with maximum energy, and E_{vert} is the energy of the vertically adjacent cell having the second highest energy. Assuming an electron lateral

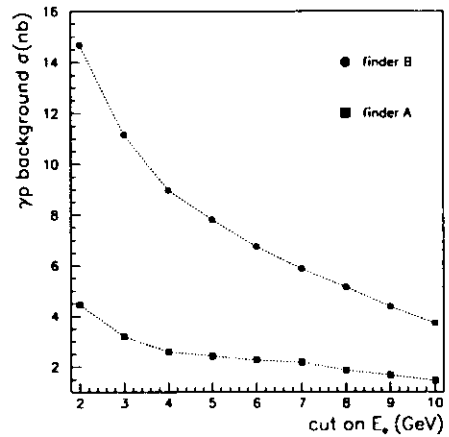

Figure 7-5 Comparison of the amount of photoproduction background picked up by two different electron finders as a function of the electron energy cut.

shower profile which consists of a hard core surrounded by a softer halo, the dependence of the y-position on this ratio was parametrized as a sum of two exponential terms. Due to a large amount of inactive material in the region close to the beam pipe, different parametrizations were chosen for the beam pipe region and for the outer part of the RCAL. The cells directly above and below the beam pipe have only one vertically adjacent neighbor. In this case, the relative energy ratio may become too small and the y-position is set to the center of the cell with the maximum energy. Figure 7-6 shows the difference between the reconstructed impact x and y-positions obtained using the calorimeter and from the HES. The resolution in x is seen to be ~ 1.2 *cm*, and ~ 1.0 *cm* in y. Figure 7-7 shows the resolutions for the corresponding electron scattering angle measurements. The resolution in θ is ~ 5 *mrad*. An expected shift in φ of ~ 13 *mrad* from the effect of a 1.43 *T* magnetic field is seen.

7.3 Vertex Reconstruction

In the structure function analysis, the calculation of the kinematical quantities require a z-vertex position. The precision of the vertex reconstruction depends on the

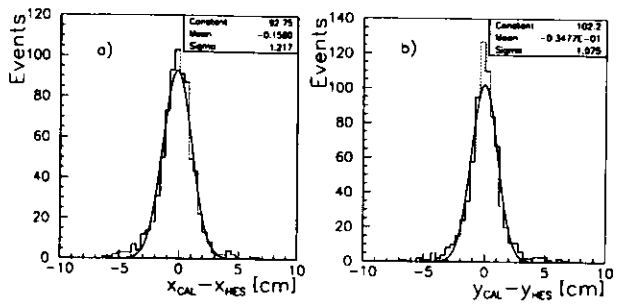

Figure 7-6 Electron position resolution in x and y. a) Plot showing the difference between the reconstructed impact position in x of the scattered electron obtained using the calorimeter and from the HES silicon diodes. b) Same as a) for the y-position.

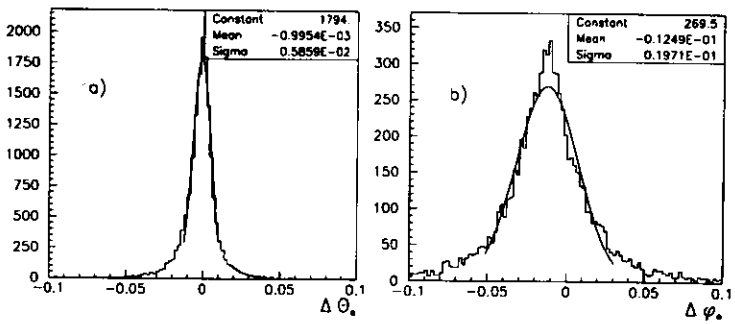

Figure 7-7 The θ and φ resolutions for the scattered electron are shown as determined from calorimeter information only.

number and quality of the tracks in the CTD. Due to the limited tracking information available during the Fall 1992 running period[1], only the primary vertex was determined

1. Only 3 of the 9 CTD superlayers were operational during this running period.

for the event[1]. The resolution of the vertex position in z is ~ 4 *cm*. The nominal beam position of 0.0 was used for the x and y coordinates.

As will be shown in the following section, the acceptance is strongly dependent on the z-vertex position. It is therefore important to reproduce the true vertex distribution in the MC simulation. A parametrization of the vertex distribution for the simulation of DIS events was obtained using the photoproduction data sample. This sample was chosen because the acceptance of these events does not have a strong z dependence.

A vertex can also be determined for events without any tracks in the CTD using the calorimeter timing information. A resolution of better than 12 *cm* was obtained by comparing the vertex reconstructed from tracking and from calorimeter information.

The same vertex prescription was used by the different structure function analyses. The procedure for the MC differs from that of the data since there is no calorimeter time simulation in the MC. This is described in Sec. 7.3.3.

7.3.1 Efficiencies and Acceptances

In Table 7-1 the efficiencies for reconstructing a vertex using the CTD for both data and MC are listed. It should be noted that the MC sample used in this analysis was generated with $Q^2 > 4\ GeV^2$ and one cannot expect identical results in a direct comparison with the data. The biggest discrepancy between the two samples can be seen in the number of events which have FCAL energy less than 5 *GeV*. A vertex requirement would then reject a larger number of these events in the data than in the MC. These events lie mostly in the low x and low Q^2 region as seen in Figure 7-8.

The acceptance of DIS events is strongly dependent on the z-vertex as illustrated in Figure 7-9. For a given scattering angle, the probability that an electron would be scattered down the beam pipe increases as the interaction point moves towards the RCAL. This leads to the decreasing calorimeter first level trigger (CFLT) acceptance as the z-vertex approaches the RCAL. After applying the final selection criteria, the variation of

1. The number of tracks in the CTD used in the vertex fit ≥ 2 with a χ^2 per degree of freedom < 10.

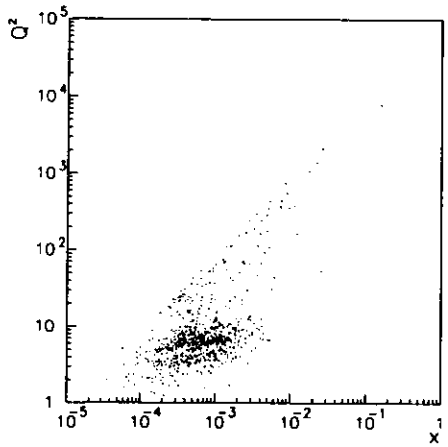

Figure 7-8 The distribution of events with $E_{FCAL} < 5\ GeV$ and no vertex from tracking.

the acceptance with z is even more pronounced. This is largely due to the effect of the 'box cut', a selection requirement which removes events wherein the impact position of the scattered electron is inside a region defined by a square with dimension 32 *cm* in *x* and *y* centered on the beam axis (see Sec. 7.4.3).

7.3.2 Vertex using calorimeter timing

The strong correlation in Figure 7-10 between the calorimeter time (Sec. 3.8.5) and the z position of the vertex from tracking provided an alternate method of obtaining an event vertex using calorimeter timing. For the Fall 1992 data, the efficiency of reconstructing a vertex using calorimeter time for those events which have energy deposits of at least 5 *GeV* in the FCAL is close to 100%, and the resolution compared is better than 12 *cm*, as illustrated in Figure 7-11.

Since the length of the electron bunch is small compared to that of the proton bunch, the *z* vertex position is determined from the timing of the particles arriving at the

requirements	MC $E_{FCAL} > 5$ *GeV*	MC $E_{FCAL} < 5$ *GeV*	Data $E_{FCAL} > 5$ *GeV*	Data $E_{FCAL} < 5$ *GeV*
none +GV[a]	52.63	0.52	67.12	7.18
std + GV	81.76	0.80	71.19	5.68
std + BV[b]	17.28	0.15	20.36	2.77
stdQ^2>[c] + GV	81.94	0.82	70.72	5.84
stdQ^2> + BV	17.08	0.16	20.76	2.68

a. A good vertex has at least two tracks used in the vertex fit and a χ^2/ndf < 10.

b. A bad vertex has one track used in the vertex fit or a χ^2/ndf > 10.

c. Final selection criteria (Sec. 7.4.3) including a $Q^2 > 7\ GeV^2$ cut.

Table 7-1 A comparison of the vertex efficiencies from tracking information for the data and the MC simulation.

FCAL near $\theta = 0$ by $t = -2z/c$, where c is the speed of light. In the MC, there is no simulation of calorimeter timing, however, one can use the true event vertex smeared by the resolution to simulate a vertex determined from the calorimeter time information. The amount of smearing was obtained by parametrizing the rms of the difference between the vertex obtained from tracking and from the calorimeter time as a function of the energy in the FCAL. The result is shown in Figure 7-12. The calorimeter vertex smearing in the MC simulation is given by

$$\sigma_z^{MC} = 9.53 + \frac{49.0}{(E_{FCAL})^{0.8851}}\ [cm]. \qquad (7\text{-}8)$$

7.3.3 Vertex Prescription

If there are at least two tracks used to reconstruct the vertex and the χ^2 per degree of freedom < 10, the vertex from tracking is used. For the data, in the absence of a good

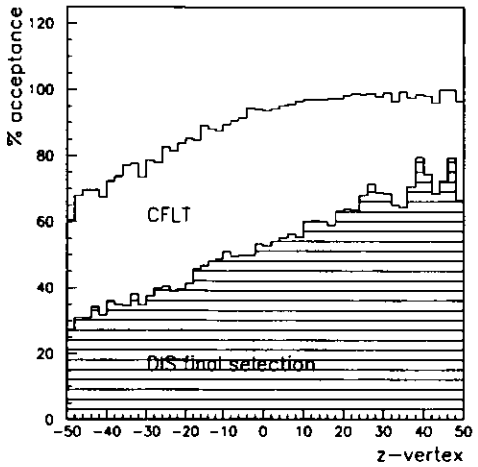

Figure 7-9 The calorimeter first level trigger (CFLT, see Sec. 3.10) and DIS final selection percentage acceptances are shown as a function of the vertex z position.

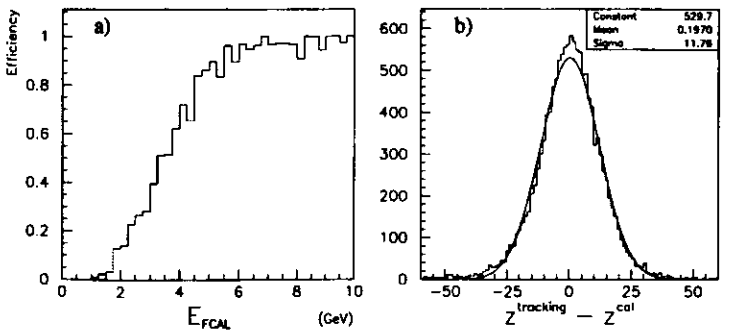

Figure 7-11 Vertex obtained from the calorimeter timing information. a) The efficiency of obtaining a vertex using calorimeter timing plotted as a function of the FCAL energy. For energies greater than 5 *GeV*, the acceptance is nearly 100%. b) The resolution of the vertex obtained using calorimeter time.

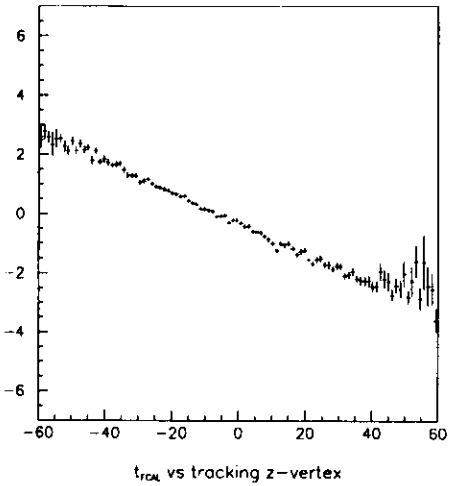

Figure 7-10 The vertex from tracking and FCAL time correlation.

reconstructed vertex from tracking, the vertex determined from calorimeter timing information is used for events with least 5 *GeV* in the FCAL. For the MC simulation, the generated vertex was smeared by the parametrization given in Eq. (7-8). A vertex requirement was not imposed, in view of the large discrepancy between the number of events in the data and in the MC sample with less than 5 *GeV* energy in the FCAL and a bad vertex from tracking. For these MC events as well as the data which did not satisfy the χ^2 requirement, the vertex with at least two tracks is used regardless of the value of χ^2. Otherwise, the vertex is set to zero.

7.4 Neutral Current Event Selection

During the Fall 1992 ZEUS running period, a sample consisting of about 4.2 million triggered events was collected. This sample was subjected to a series of selection criteria to isolate the DIS events from backgrounds and obtain a fiducial sample of well measured neutral current candidates to be used in the extraction of the proton structure function. The selection of DIS events was done in three stages, namely the off-

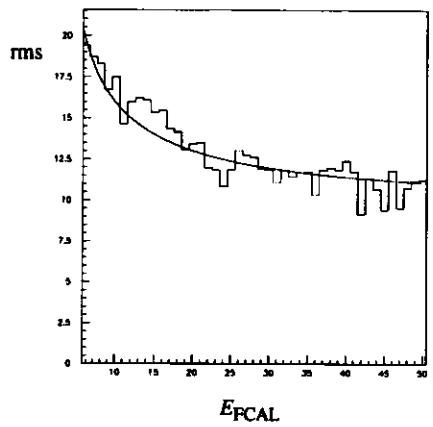

Figure 7-12 The rms of the difference between the vertex from tracking and the vertex from calorimeter time plotted as a function of the FCAL energy. The resolution improves with increasing energy.

line filtering, the preselection and the final selection. The first two stages rely only on the observation of an electromagnetic energy deposit in the calorimeter above some threshold value and do not use any electron finding algorithm. For background rejection, care was exercised not lo lose any DIS physics events. In the final selection, the criteria used are more stringent in order to remove poorly measured events as well as background events.

7.4.1 DST Filter

The first level of event selection was performed during the off-line reconstruction of the raw data. At ZEUS, each physics group has proposed an algorithm designed to filter and to select the physics events of interest. The selected events are then written to data summary tapes (DST). Neutral current events are characterized by the presence of a scattered electron in the calorimeter. Hence, an event is considered a DIS candidate if it was triggered by a total energy deposit in either the rear or the barrel electromagnetic calorimeter (REMC or BEMC) which is above a typical threshold value of 1 *GeV*.

There was a minimum energy requirement for either REMC or BEMC of 2 or 5 *GeV*, respectively. For events wherein an electron signature is mimicked by randomly sparking BEMC cells, one can use the energy imbalance between the left and right phototubes of the cell. The energy imbalance, defined in Eq. (7-7), is set to zero if one of the phototubes of the cell is not operational. The event was rejected if the misidentified electron consists of only one BEMC cell which has an imbalance of zero, and there was no other energy deposit in the calorimeter; the trigger being caused by a sparking PMT in the EMC. In addition, the filter includes a calorimeter timing requirement. This cut removes beam induced background from proton interactions outside the main detector region. A more refined timing requirement was used in the preselection stage discussed in the next section.

Of the total sample of 4.2 million recorded triggers taken during the Fall 1992 running period, there were about 2.3 x 10^5 events remaining after the DIS neutral current DST filter.

7.4.2 Preselection

The preselection of *ep* candidates was driven by two main objectives. First, one has to ensure that the status of the major detector components was reliable during the data taking period. Some runs or parts of runs were excluded because the magnet, the central tracking detector or the luminosity monitor was not operational. The second objective was to enrich the event sample by rejecting background while retaining DIS events.

At the preselection stage, the background rejection criteria are quite conservative. The background consists primarily of beam-gas events, cosmic muons and events from photoproduction. The interaction of protons with the residual gas in the beam pipe or with the beam pipe itself is primarily responsible for the beam-gas background. Events with measured times in the calorimeter or in the C5 monitor (Sec. 3.6) consistent with interactions upstream of the detector were rejected on-line to reduce this rate. In the preselection, these events are removed by a set of stricter calorimeter timing requirements. As shown in Figure 7-13, one can clearly separate the beam-gas background from *ep* candidates by plotting the measured time difference between the FCAL and RCAL versus the RCAL time. The calorimeter timing requirements to remove beam-gas events were then chosen as follows:

$$
\begin{aligned}
&|t_{RCAL}| \text{ or } |t_{FCAL}| > 6\ ns \\
&(t_{FCAL} - t_{RCAL}) < -6\ ns \\
&(t_{FCAL} - t_{RCAL}) > 0.5 t_{RCAL} + 6.
\end{aligned}
\tag{7-9}
$$

Events were also rejected if there was activity in the vetowall. The vetowall (Sec. 3.7), situated 7.5 m upstream of the interaction point, is sensitive to upstream proton interactions. A trigger coincidence on both sides of the vetowall is considered a beam-gas event.

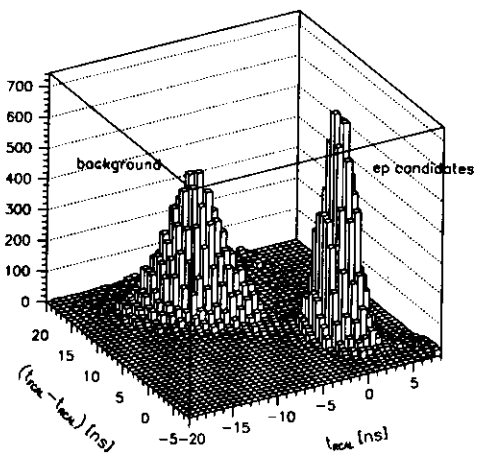

Figure 7-13 A clear separation between beam-gas background and *ep* candidates is shown by the lego distribution of the measured time difference between the FCAL and RCAL plotted versus the RCAL time.

The quantity

$$
\delta = \sum_i E_i (1 - \cos\theta_i)\,, \tag{7-10}
$$

discriminates between background and DIS events; the sum is over all measured calorimeter cell energies E_i and angles θ_i. Ignoring detector resolution and initial state radiation effects, this quantity should be nearly twice the electron beam energy for fully

contained DIS events. Photoproduction events, wherein the final state electron remains in the beam pipe, give significantly lower values of δ. The δ distribution for the Fall 1992 photoproduction sample is shown in Figure 7-14. The preselection for DIS events required that $\delta + 2L_\gamma \geq 25\ GeV$, where the quantity L_γ is the energy of the photon tagged in the luminosity monitor.

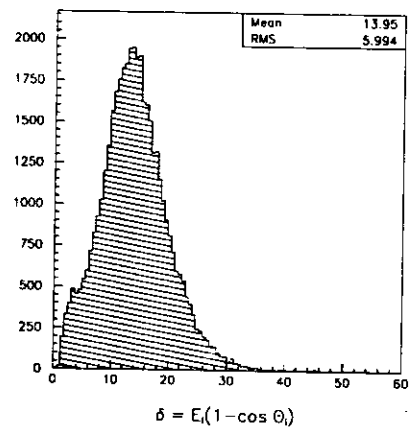

Figure 7-14 The δ distribution for the Fall 1992 tagged photoproduction event sample.

A more refined algorithm, extended to the FCAL and RCAL, was also applied for spark rejection. The events were checked for cells with dead channels or energy imbalance greater than 0.9 and energies greater than 2.5 GeV.

Cosmic background was rejected using an algorithm based on calorimeter timing, tracking information, hits in the barrel muon chambers, and the correlation between the positions of the calorimeter cell hits and their corresponding times. Based on a sample of cosmic muon events, the efficiency of this muon finding algorithm is about 80%.

Applying the preselection criteria discussed above, the preselected sample was reduced to 19850 DIS neutral current event candidates.

7.4.3 Final selection

Additional requirements were imposed on the preselected sample to eliminate background and ensure that only well measured events are used in the proton structure function measurement. Four main considerations are addressed by the final selection criteria namely:

- the contamination from the photoproduction background,
- electron finding efficiency and purity,
- electron energy containment and position reconstruction,
- and calorimeter noise effects.

First, the cut on δ to eliminate the photoproduction background was increased from $\delta \geq 25\ GeV$ in the preselection to $35\ GeV \leq \delta \leq 60\ GeV$. In Figure 7-14, it can be seen that the lower limit is well outside the tail of the δ distribution for photoproduction events. The upper limit from energy and momentum conservation, δ should not exceed twice the electron beam energy, 53.4 *GeV*. However, due to detector smearing effects and measurement errors, δ might exceed this value.

Second, an electron energy requirement of at least 5 *GeV* was imposed to ensure high efficiency and purity of the electron finding algorithm, and also to reject background from photoproduction. As discussed in Sec. 7.2, the choice of the electron finder was based mainly on the power of discrimination against the photoproduction background it picks up. For the chosen algorithm, finder A, the photoproduction background cross section, using only the δ requirement mentioned above, was estimated as a function of the electron energy cut; this is plotted in Figure 7-15 (also shown in Figure 7-5 for two finders). Figure 7-16 illustrates the effect of the 5 *GeV* electron energy requirement on the DIS MC events, as well as its effect on the photoproduction MC sample. The electron energy requirement, combined with the δ criterion, significantly suppresses the background from photoproduction.

Third, the impact position of the scattered electron on the calorimeter was required to be outside a region defined by a square with dimension 32 *cm* in x and y centered on the beam axis, the 'box cut' ($|x|, |y| > 16$ *cm*). Due to partial shower losses of electrons which hit the calorimeter near the edge of the beam hole, the energy and the angle

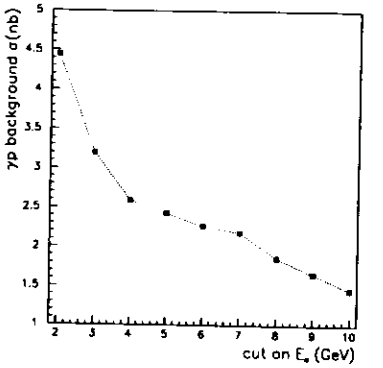

Figure 7-15 The estimated photoproduction background cross section of the electron finder chosen (Sec. 7.2) for the proton structure function measurement as simulated in the MC.

measurements become degraded. This requirement allows a precise measurement of the position and energy of the electron. In Figure 7-17, the resolution of the electron position measurement is plotted as a function of R, defined as the perpendicular distance between the beam axis and the impact position on the RCAL.

And finally, the requirement $y_{JB} > 0.02$ was applied to ensure a reasonable resolution of the quark scattering angle γ and to reduce any bias from calorimeter noise effects. In Sec. 5.4, the effects of noise for different methods of reconstruction was discussed, and it was shown that the methods using the hadronic variables are quite sensitive to noise in the small y region. Figure 7-18 illustrates how the resolution of the measurement of γ, given in Eq. (5-31), improves as the y_{JB} requirement is increased. The γ resolution is shown before (Figure 7-18a) and after (Figure 7-18b) hadronic energy corrections are applied.

Table 7-2 summarizes the effects of the final selection criteria. Some of the events which survived the above selection criteria were scanned visually to remove any remaining cosmic muons and elastic QED Compton events. An estimate of each type of background remaining after final selection is discussed in the following section.

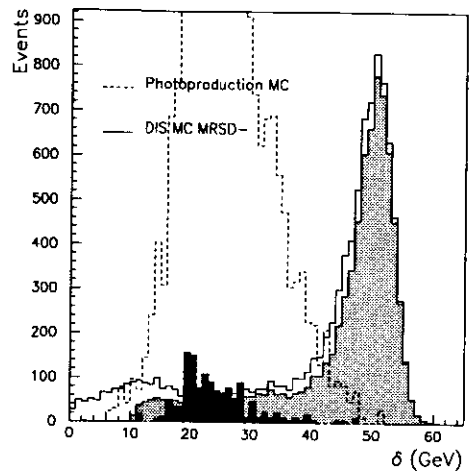

Figure 7-16 The δ distribution for both DIS and photoproduction MC samples (solid and dashed) are shown. The shaded histograms show the events which survive the 5 *GeV* electron energy requirement.

7.5 Background in the Final Selection

After preselection, the bulk of the background consists of events from photoproduction. For these events, the electron is scattered at small angles and goes down the rear beam hole. However, the presence of another electromagnetic energy deposit from a photon or a low energy pion in the calorimeter may be mistakenly reconstructed as an electron. In addition to the photoproduction background, there is also contamination from cosmic and halo muons, QED Compton, and beam-gas events. In the following sections each type of background is discussed in more detail.

7.5.1 Photoproduction Background

The major source of background after selection cuts is due to processes wherein the scattered electron remains in the beam pipe. At HERA, this background is more pronounced in the high y region where the scattered electrons have small energies and

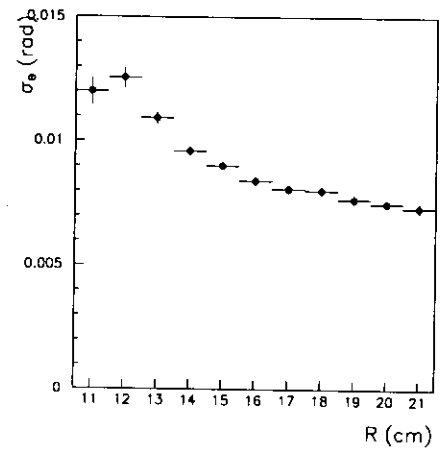

Figure 7-17 Plot of the resolution of the electron position measurement as a function of the perpendicular distance from the beam axis and the impact position on the RCAL as simulated in the MC.

Selection	Remaining events
Preselection	19850
$35\ GeV \leq \delta \leq 60\ GeV$	9304
$E_e > 5\ GeV$	6237
box cut	3528
$y_{JB} > 0.02$	2365

Table 7-2 Remaining events in the preselected sample after each selection requirement is applied successively.

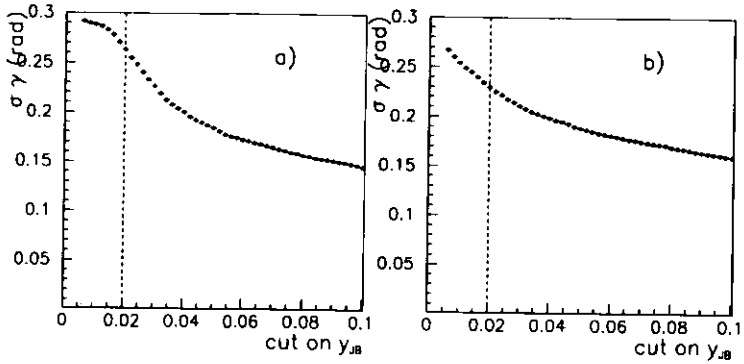

Figure 7-18 The resolution of the measurement of the angle of the struck quark, γ, improves as the cut on y_{JB} is increased. a) Before and b) after hadronic energy corrections are applied.

electron detection becomes difficult. A MC event which passes the final selection criteria with $\delta = 36.7$ *GeV* and a misidentified electron in the RCAL from the photoproduction MC sample is shown in Figure 7-19.

The remaining background from photoproduction in the final sample was estimated using two sets of MC event samples. The first set consisted of 36k PYTHIA [55] photoproduction events with the generated Q^2 range extending up to 2 GeV^2. The second set consisted of photoproduction events generated using HERWIG [66]. In the PYTHIA sample (see Sec. 4.2), the spectrum of the scattered electron was generated using a parametrization of the total photoproduction cross section down to $Q^2 \sim 0$. Hadrons were generated using the γp interaction scheme of PYTHIA, after taking properly into account the kinematics of the virtual photon.

In order to achieve a better statistical probing of the available photoproduction phase space, the PYTHIA sample was divided into three overlapping *y* regions. The cross sections integrated over kinematical limits (in μb), the corresponding cross sections per event for each of the *y* regions (in *nb*), and the event weights corresponding to the DIS Fall 1992 luminosity of 24.7 nb^{-1} are listed in Table 7-3 below.

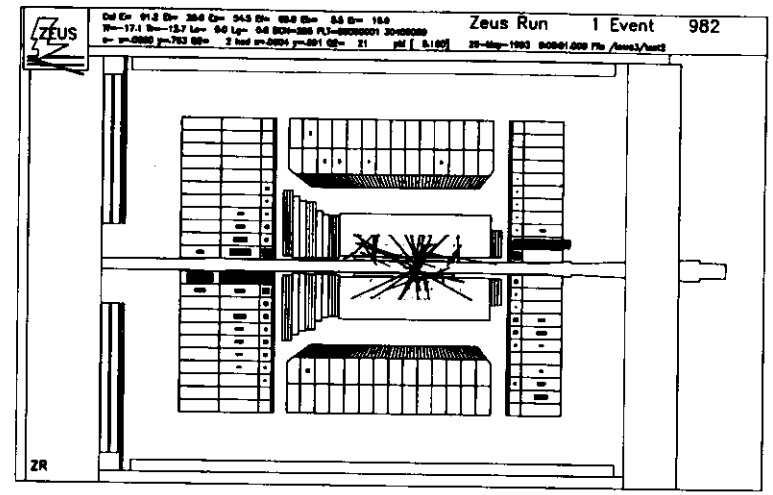

Figure 7-19 An event from the photoproduction MC sample using PYTHIA passing the final selection. A misidentified electron is shown in the RCAL.

y range	$0.60 < y < 0.75$	$0.73 < y < 0.88$	$0.85 < y < 1.00$
integrated σ *(μb)*	0.549	0.403	0.296
σ *(nb)* per event	0.046	0.035	0.025
event weight	1.132	0.857	0.628

Table 7-3 The PYTHIA sample used to estimate the background due to photoproduction. The cross sections integrated over the kinematical limit (in μb), the corresponding cross sections per event (in *nb*), and the event weights corresponding to the Fall 1992 data luminosity of 24.7 nb^{-1} are given for three different *y* ranges.

A study was performed using the three electron finders described in Sec. 7.2 and in cases where more than one electron candidate was found, the candidate with the highest energy was chosen. Those events which satisfied the DIS on-line trigger requirement (an OR of the on-line trigger bits FEMC, BEMC, REMC, FHAC) are then passed through the final selection criteria discussed previously in Sec. 7.4.3. Table 7-4 lists the visible cross sections from the photoproduction background and the number of unweighted events which satisfied the selection criteria in each of y range for the three electron finders. The events in the overlapping y region for the file with the lower y range were not used.

The electron finder A has the lowest efficiency but the highest purity among the three finders. Figure 7-20 shows the distribution in x and Q^2 of the 51 unweighted events wherein finder A found an electron. To get the cross section for any x and Q^2 bin, one can sum the event weights in that bin and divide it by the corresponding luminosity in the data.

e-finder	$0.60 < y < 0.73$	$0.73 < y < 0.85$	$0.85 < y < 1.00$	$\sigma_{visible}(nb)$
A	0	16	35	1.435 ± 0.206
B	5	45	87	4.002 ± 0.348
C	8	77	175	7.486 ± 0.472

Table 7-4 The visible cross sections from the photoproduction background for three electron finding algorithms.

The analysis was repeated using the HERWIG photoproduction sample. This sample was generated over the entire kinematic y range. The results obtained using HERWIG agree with those using PYTHIA within statistical errors. The visible photoproduction background cross section for the electron finder A is $2.333 \pm 0.916\ nb$ which agrees with the PYTHIA results within the statistical error.

It is clear that the photoproduction background depends very much on the electron finder one uses as shown in Table 7-4. In the structure function analysis, the electron finder A was used mainly because it gives the least amount of background, although it is less efficient than B or C. The estimate of the photoproduction background in the final sample is small and is about 1.44 nb.

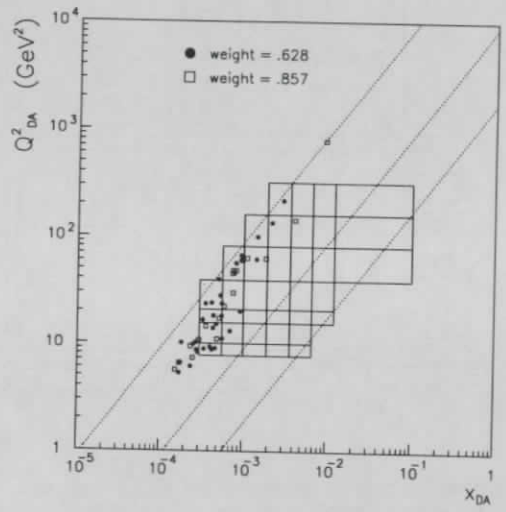

Figure 7-20 Photoproduction background for electron finder A in bins of x_{DA} and Q^2_{DA}.

7.5.2 Beam Induced Background

Another large source of background comes from the interaction of the proton or electron beam with the residual gas. To estimate beam related background, one can count the number of events coming from the unpaired proton or electron (pilot) bunches. The bunch crossing number distribution is shown in Figure 7-21. For most of the runs, the electron pilot bunch was either at bunch number 18 or 19. The proton pilot bunch is always at the ninth bunch. In the preselected sample, there were 47 and 109 events from the proton and electron pilot bunch respectively. This represents a background of about 2.4% from the proton gas and 5.5% from the electron gas in the preselected sample.

No events from the proton pilot bunch remained in the final DIS sample; however, it contained three events from the electron pilot bunch representing 0.1% of the sample. Two of these e-gas events are inside the selected x,Q^2 bins. About 94% of the proton

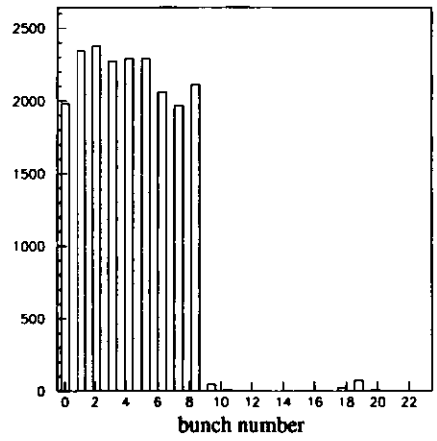

Figure 7-21 The bunch crossing number distribution for the Fall 1992 DIS data. Typically the unpaired proton and electron bunch is at bunch number 9 and 19 respectively. These pilot bunches were used to estimate the beam-gas background in the sample.

beam-gas background is rejected by the electron energy requirement. This also removes about 80% of the electron beam-gas. The remaining electron beam-gas events were weighted by 9.73 when doing background subtraction. This factor was obtained from the ratio of the luminosity weighted electron current in the paired *ep* bunches to the current in the unpaired electron pilot bunch. The distribution to determine this ratio is shown in Figure 7-22. A typical electron beam-gas event is shown in Figure 7-23.

7.5.3 Other Sources of Background

In the final sample, events with $Q^2 > 50\ GeV^2$ were scanned to remove events triggered by cosmic muons which were not found by the muon finder. A typical cosmic event in the detector is shown in Figure 7-24. In addition to cosmic muons, there was also a background due to muons produced from the interaction of the proton beam with the residual gas in the beam pipe. Such events are referred to as beam halo muons.

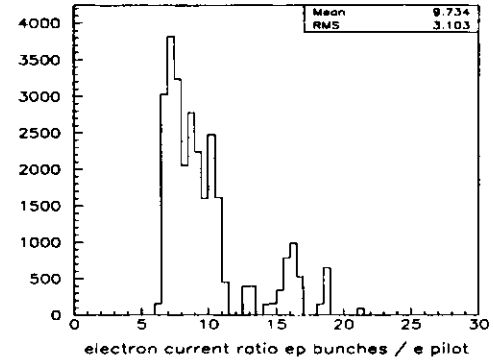

Figure 7-22 The ratio of the luminosity weighted electron current in the paired *ep* bunches to the current in the unpaired electron bunch for the DIS data.

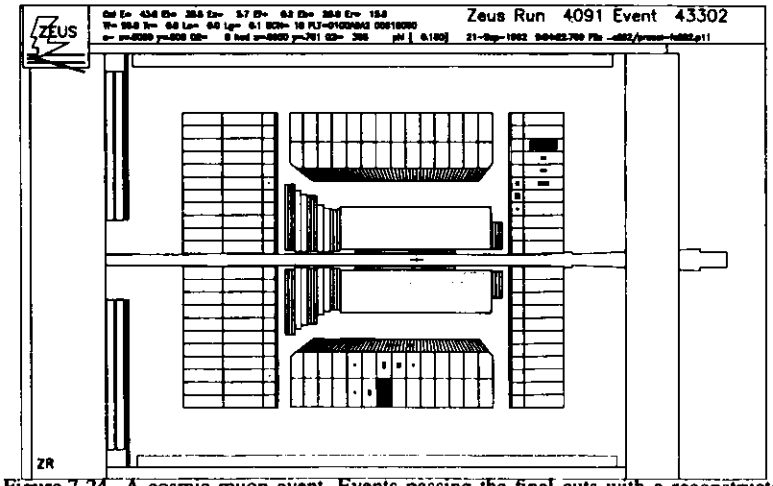

Figure 7-24 A cosmic muon event. Events passing the final cuts with a reconstructed $Q^2 > 50\ GeV^2$ were visually scanned to remove the remaining cosmic background events.

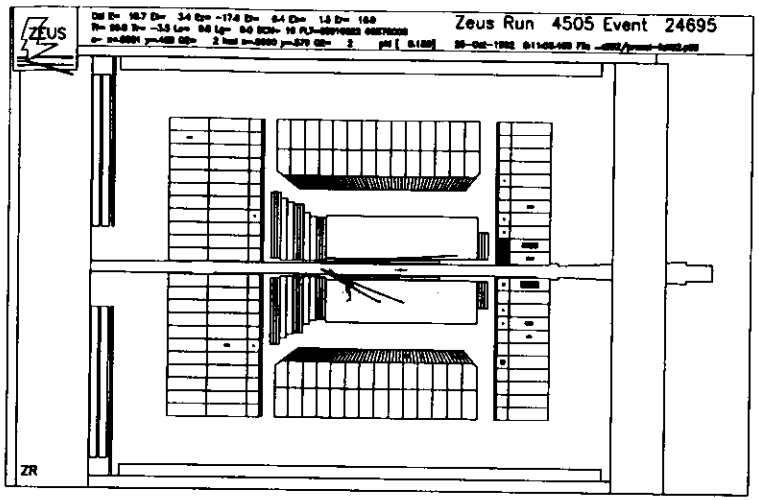

Figure 7-23 One of the electron gas events where the interaction occurs between the FCAL and RCAL. Calorimeter timing cuts are not able to remove beam-gas events which occur within the calorimeter region.

The MC simulation used in this analysis did not include the elastic QED Compton events ($ep \rightarrow ep\gamma$); a few of which were observed in the data. To tag the elastic QED Compton events, all events in the final sample with less than 1 GeV in the FCAL were scanned. Another check done was to scan all events where an electron finder found exactly two electron candidates in the calorimeter. These two methods gave a consistent number of QED Compton events. These events were then removed from the final sample. A typical elastic QED Compton event is shown in Figure 7-25. All the muon and QED Compton tagged events were written in a scan list and were removed in the final analysis. The background due to any remaining cosmic or beam halo muons and the elastic QED Compton events is negligible.

7.6 Events with a Large Rapidity Gap

A previous measurement of the neutral current differential cross section using the Summer 1992 ZEUS data [4] required events to have an energy deposit of at least 1 GeV

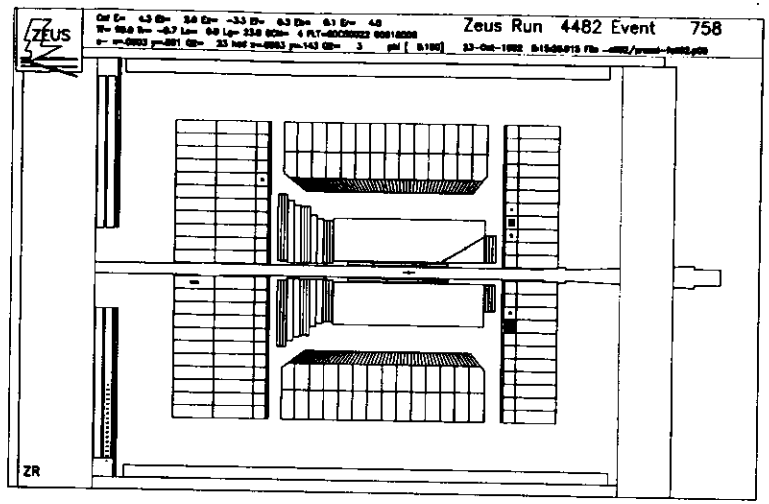

Figure 7-25 An elastic QED Compton event with a single track pointing to the electron. Events with two electron candidates or energy in the FCAL less than 1 GeV were visually scanned to remove these events.

in the FCAL. This effectively rejected cosmic as well as beam-gas background events. However, it was observed that the number of events failing this requirement in the data sample was in disagreement with MC expectations. A visual scan revealed that although a large number of those events which failed this requirement was background, some were clearly deep inelastic events. Due to the very limited amount of statistics available then (corresponding to a luminosity of $\sim 2\ nb^{-1}$), an extensive study was not possible. In the analysis of the Fall 1992 data, this requirement was reviewed. The result of the comparison between the MC simulation and a larger data sample (corresponding to a luminosity of $\sim 24.7\ nb^{-1}$) led to the observance of a new class of DIS events.

In Figure 7-26 the FCAL energy distribution is plotted versus y_{JB} for both the data and MC events which satisfy the final selection criteria (y_{JB} requirement was not applied). Events with small energy deposits in the FCAL occur predominantly at low y_{JB}. A clear excess of events with low FCAL energies and relatively large values of y_{JB} is observed in the data, in disagreement with MC expectations. Large y values correspond to events

where the struck quark is emitted at a large polar angle relative to the incident proton beam direction.

For these excess events observed in the data, the pseudorapidity defined by

$$\eta = -ln\left(\tan\frac{\theta}{2}\right) \qquad (7\text{-}11)$$

for the cluster closest to the proton beam direction with a minimum energy of 0.4 *GeV*, is sizably different compared to the pseudorapidity of the smallest detector angle[1]. Events typical of those with a large pseudorapidity gap are shown in Figure 7-27.

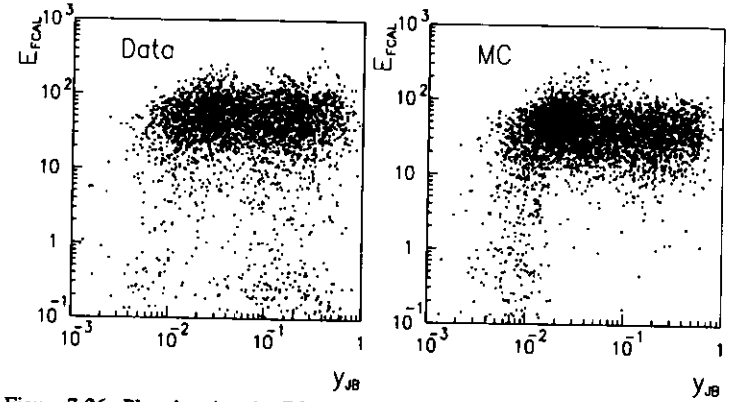

Figure 7-26 Plot showing the FCAL energy as a function of y_{JB} for the data and MC samples. A clear excess of events with low FCAL energies but with relatively large values of y_{JB} is observed in the data, in disagreement with MC expectations.

A useful quantity used to classify these events is η_{max}, which is defined as the pseudorapidity of the calorimeter hadronic cluster with energy greater than 0.4 *GeV*,

1. The pseudorapidity ranges from 4.3 to -3.8 corresponding to the smallest and largest measurable polar angles in the ZEUS detector, defined by the inner edge of the forward and rear calorimeter respectively (see Figure 7-27).

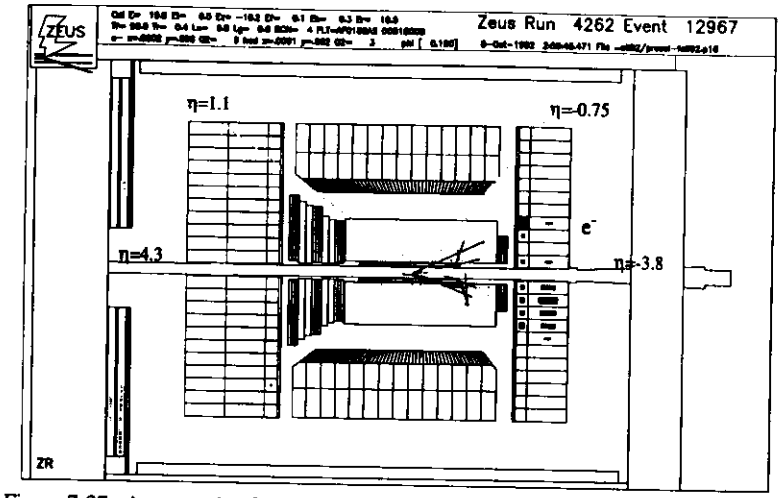

Figure 7-27 An example of an event with a large rapidity gap. These events are characterized by a very low energy in the forward region, but with a high y_{JB}.

closest to the proton beam direction. The η_{max} distribution is shown for both the data and MC samples in Figure 7-28. Values of $\eta_{max} > 4.3$ are obtained when a number of cells are clustered immediately around the forward beam hole and the clustering algorithm measures an angle within the beam hole. A clear excess of events are observed in the data for values of $\eta_{max} < 1.5$. This requirement separates events which have a rapidity gap of at least 2.8 units. After applying the final selection cuts the number of events with η_{max} below this value is 158, corresponding to 5.8% of the final DIS sample. This is a lower limit since the requirement of a gap in pseudorapidity of at least 2.8 units limits the acceptance of these events, and acceptance corrections were not applied.

An interesting feature of these events is illustrated in Figure 7-29 showing the correlation between the invariant mass of the measured hadronic system, M_x, and the total energy available in the $\gamma^* p$ system, W. For events with $\eta_{max} < 1.5$, M_x is relatively small, typically smaller than 10 *GeV*. For values of $W > 120$ *GeV* these events are well separated from the rest of the DIS sample.

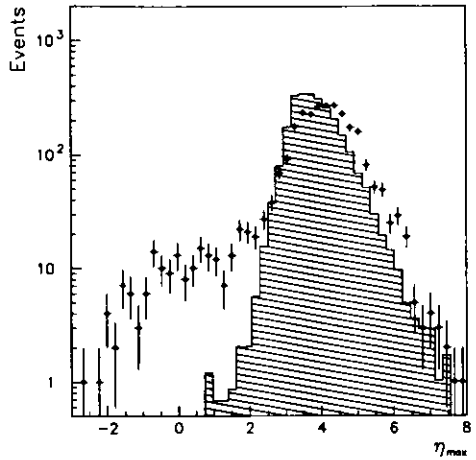

Figure 7-28 Maximum pseudorapidity distribution of hadronic clusters with calorimeter energy greater than 400 *MeV*. In the data events which exhibit a large pseudorapidity gap with values of $\eta_{max} < 1.5$ are observed in excess compared to MC expectations.

In Figure 7-30 the fraction of events with a large pseudorapidity gap is plotted as a function of the square of the momentum transfer, Q^2, for two selected x bins, $x < 0.0008$ and $0.0008 < x < 0.003$. Due to acceptance[1], this ratio decreases with increasing x. Within statistical errors, this fraction is independent of Q^2 [67].

7.7 MC and Final Data Event Sample Distributions

The vertex distribution and the distributions of the events which satisfy the final selection criteria in both the data and MC sample in Q^2, x and y are shown in Figure 7-31a for the double angle reconstruction method. The dots represent the data and the full lines

1. Events in which the hadronic final states are boosted in the forward direction would lead to large values of x (shown in Figure 6-4). These events will not be classified as having a large pseudorapidity gap since the acceptance for these events is limited by the definition of the η_{max} cut.

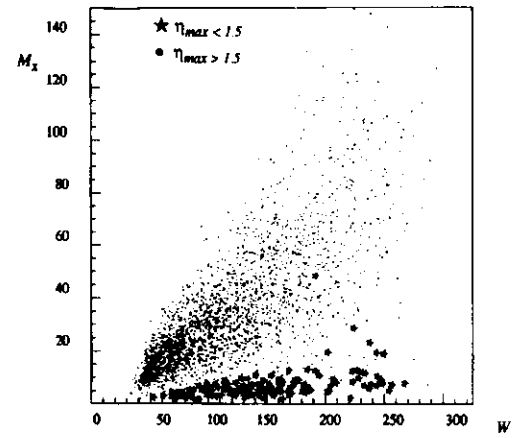

Figure 7-29 The invariant mass of the measured hadronic system M_x is plotted as a function of the total energy available in the $\gamma^* p$ system. Events with a large pseudorapidity gap have typical M_x values smaller than 10 *GeV* and are well separated from the rest of the DIS sample for $W > 120$ *GeV*.

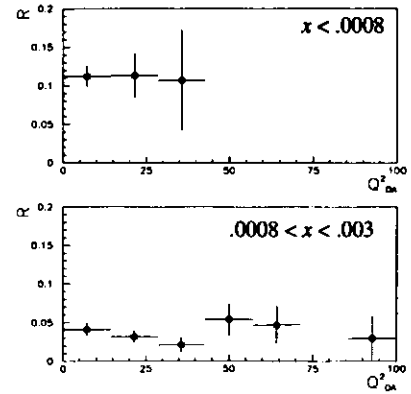

Figure 7-30 The fraction of events with a large pseudorapidity gap, R, is plotted as a function of Q^2 for two selected x bins. Within errors, this fraction is not dependent on Q^2.

represent the MC simulation for the MRS D_' parametrization[1] (described in Sec. 1.5). The number of events in the MC has been normalized to the number of events in the data. In Figure 7-31a there is a good agreement between the vertex distribution in the data and

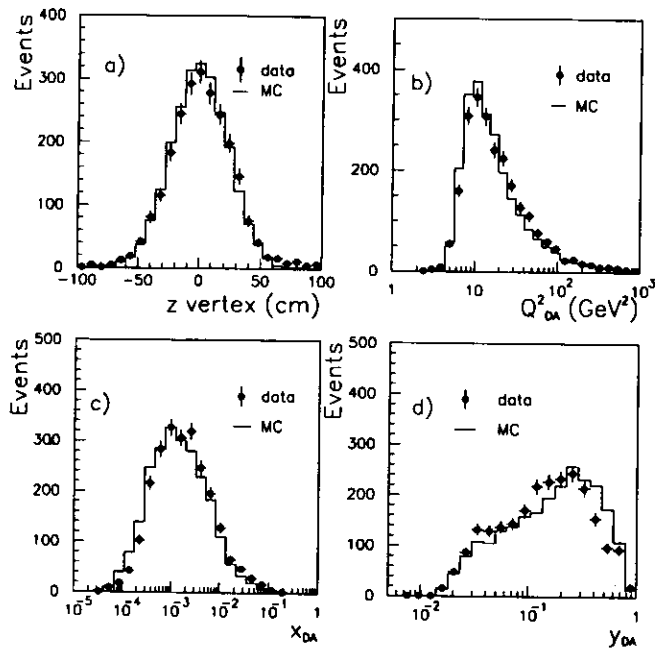

Figure 7-31 MC simulation (full lines) and final data event sample (dots) distributions. a) The reconstructed vertex distribution, b) Q^2_{DA} c) x_{DA} and d) y_{DA} event distributions. The number of events in the MC is normalized to the number of events in the data.

the MC simulation. For the distributions in Q^2, x and y shown in Figure 7-31b-d there is an overall agreement between the shapes of the distributions in the MC simulation and the data.

1. It has been observed that the data are in better agreement with the MRS D-' and GRV parton parametrizations.

CHAPTER 8

DETERMINATION OF THE PROTON STRUCTURE FUNCTION

This section presents the results of an independent measurement of the proton structure function $F_2(x,Q^2)$ using the data collected in the Fall 1992 running period with the ZEUS detector at HERA.

8.1 Overview

A sufficiently accurate measurement of the cross section for the inclusive electron-proton scattering process shown in Figure 5-1 is required for the determination of the proton structure function structure function F_2. The inelastic cross section in bins of x,Q^2 for neutral and charged current scattering in terms of the generalized structure functions $\mathcal{F}_i$ is given by

$$\frac{d^2\sigma}{dxdQ^2} = \frac{4\pi\alpha^2}{xQ^4}\left[y^2 x\mathcal{F}_1(x,Q^2) + (1-y)\,\mathcal{F}_2(x,Q^2) + (y-\frac{y^2}{2})\,x\mathcal{F}_3(x,Q^2)\right] \quad (8\text{-}1)$$

where α is the electromagnetic coupling constant.

$\mathcal{F}_1$ is related to $\mathcal{F}_2$ through the Callan-Gross relation [12], $2x\mathcal{F}_1 = \mathcal{F}_2$. The structure functions $\mathcal{F}_2$ and $x\mathcal{F}_3$ are expressed as linear combinations of the quark[1] and antiquark density distributions, $q_f(x,Q^2)$ and $\bar{q}_f(x,Q^2)$ [68],

$$\mathcal{F}_2(x,Q^2) = \sum_f A_f(Q^2)\,[xq_f(x,Q^2) + x\bar{q}_f(x,Q^2)] \quad (8\text{-}2)$$

$$x\mathcal{F}_3(x,Q^2) = \sum_f B_f(Q^2)\,[xq_f(x,Q^2) - x\bar{q}_f(x,Q^2)] \quad (8\text{-}3)$$

1. The functions $q_f(x,Q^2)$ ($\bar{q}_f(x,Q^2)$) may be interpreted as the probability for finding a spin 1/2 point-like constituent quark (antiquark) carrying a fraction of the nucleon momentum x.

summed over the quark flavors f in the proton. The flavor and Q^2 dependent coefficients, A_f and B_f, contain contributions from pure photon exchange, γ-Z° interference, and pure Z° exchange. They are given by [68]

$$A_f(Q^2) = e_f^2 - 2e_f v_f (v_e \pm \lambda a_e) P_Z + (v_f^2 + a_f^2)(v_e^2 + a_e^2 \pm 2\lambda v_e a_e) P_Z^2 \qquad (8\text{-}4)$$

$$B_f(Q^2) = -2e_f a_f (a_e \pm \lambda v_e) P_Z + 2v_f a_f (2v_e a_e \pm \lambda (v_e^2 + a_e^2)) P_Z^2 \qquad (8\text{-}5)$$

which involve the lepton polarization λ ($+\lambda$ for electron and $-\lambda$ for positron scattering), the fractional quark electric charges e_f (e_u = 2/3, e_d = -1/3, etc.), the NC vector and axial couplings of the electron where $v_e = -1 + 4\sin^2\theta_w$, and $a_e = -1$, and similarly for the quarks $v_f = 2T_{3f} - 4e_f \sin^2\theta_w$ and $a_f = 2T_{3f}$ where T_{3f} is the third component of the weak isospin (T_{3u} = 1/2, T_{3d} =-1/2, etc.). The Z propagator ratio is given by

$$P_Z(Q^2) = \frac{1}{(2\sin\theta_w)^2}\left[\frac{Q^2}{Q^2 + M_Z^2}\right], \qquad (8\text{-}6)$$

where θ_w is the Weinberg angle. Hence, $\mathcal{F}_2(x,Q^2)$ can be explicitly written as a sum of the three contributions:

$$\mathcal{F}_2(x, Q^2) = F_2^{EM}(x, Q^2) + F_2^{\gamma - Z^\circ}(x, Q^2) + F_2^{Z^\circ}(x, Q^2). \qquad (8\text{-}7)$$

For unpolarized ($\lambda = 0$) NC scattering where $Q^2 << M_Z^2 \sim 10^4\ GeV^2$, P_Z can be neglected. The contributions from $x\mathcal{F}_3$ as well as from the second and third terms in Eq. (8-7) can then be neglected. In this case $\mathcal{F}_1$, $\mathcal{F}_2$, $\mathcal{F}_3$, and $\mathcal{F}_L$ are equal to the conventional electromagnetic structure functions F_1, F_2, F_3, and F_L. Figure 8-1 shows that the single photon approximation is valid for the current kinematic range over which F_2 is to be determined. This is a good approximation for low x and medium Q^2, as shown by the values of F_2 obtained using the MRSD_' parton density parametrizations plotted as a function of Q^2 for the values of x at which F_2 will be measured. For the accessible kinematic range at HERA (shown as the solid lines in Figure 8-1) the dominant contribution to the neutral current cross section comes from a pure virtual photon exchange and the contribution arising from Z° exchange (dotted lines) is negligible.

The structure functions given in Eq. (8-4) and Eq. (8-5) were obtained by assuming that the quark constituents of the nucleon are entirely free and stationary, and

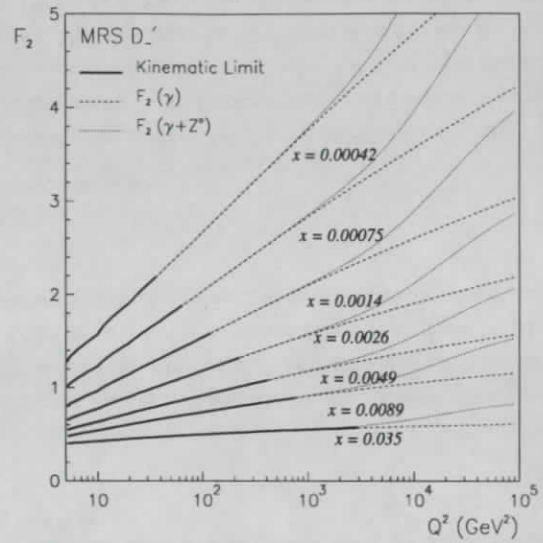

Figure 8-1 Using the MRSD_' parton density parametrizations, this plot shows the contribution of Z° exchange in the determination of $F_2(x,Q^2)$ as a function of Q^2 obtained assuming the exchange of a single virtual photon, while the dotted lines include both the γ-Z° interference and a single Z° exchange contributions. The solid lines represent the values of F_2 for the accessible kinematic range at HERA.

thus neglecting the binding forces between them. In the improved parton model, the Callan-Gross relation [12] for massless spin 1/2 partons with zero transverse momenta is no longer valid such that

$$F_2(x, Q^2) - 2xF_1(x, Q^2) = F_L(x, Q^2) \qquad (8\text{-}8)$$

is non zero and proportional to the quark-gluon coupling constant, α_s. To a good approximation F_L can be neglected except in the very low x region where the contribution from gluons become significant. Its measurement can then be used to extract the gluon distribution function [69]. In the single photon approximation assuming negligible contribution from Z° exchange, the NC differential cross section reduces to

$$\frac{d^2\sigma_{NC}}{dxdQ^2} = \frac{2\pi\alpha^2 Y_+}{xQ^4}\left[F_2(x,Q^2) - \frac{y^2}{Y_+}F_L(x,Q^2)\right], \qquad (8\text{-}9)$$

where $Y_+ = 1 + (1\text{-}y)^2$.

8.2 The $F_L(x,Q^2)$ Contribution

The longitudinal structure function has not yet been measured at HERA. In order to determine $F_2(x,Q^2)$ from Eq. (8-9) an assumption using the QCD prediction in [70] was made to estimate F_L using the MRSD_' parton parametrizations. The longitudinal structure function is given by [70]

$$F_L^{QCD}(x,Q^2) = \frac{\alpha_s(Q^2)}{2\pi}x^2\left[\int_x^1 \frac{dz}{z^3}\left[\frac{8}{3}F_2(z,Q^2) + 4\left(\sum_{i=q} e_i^2\right)zG(z,Q^2)\,(1-\frac{x}{z})\right]\right] \qquad (8\text{-}10)$$

The lowest order processes leading to a non zero F_L are shown in Figure 8-2. The integral over F_2 in the first term of Eq. arises from the quark emission of a gluon prior to interaction as shown in Figure 8-2a, while the integral over the gluon distribution, $G(z,Q^2)$, results from the quark pair production from the gluon shown in Figure 8-2b. At small x the second term dominates due to the increasing gluon distribution. The measurement of F_L therefore gives an indirect estimate of the gluon distribution [69].

For each of the x,Q^2 bins the measured cross section is corrected for F_L^{QCD} [71] to obtain the contribution arising only from F_2:

$$\sigma(F_L(x,Q^2)) = \iint\left[\frac{2\pi\alpha^2 Y_+}{xQ^4}\left(\frac{y^2}{Y_+}F_L\right)(x,Q^2)\right]dxdQ^2 \qquad (8\text{-}11)$$

$$\sigma(F_2(x,Q^2)) = \iint\left[\frac{2\pi\alpha^2 Y_+}{xQ^4}F_2(x,Q^2)\right]dxdQ^2. \qquad (8\text{-}12)$$

$\sigma(F_L)$ becomes more significant at large y values. This correction factor, given by

$$corr(x,Q^2) = \left[1 - \frac{\sigma(F_L(x,Q^2))}{\sigma(F_2(x,Q^2))}\right]^{-1}, \qquad (8\text{-}13)$$

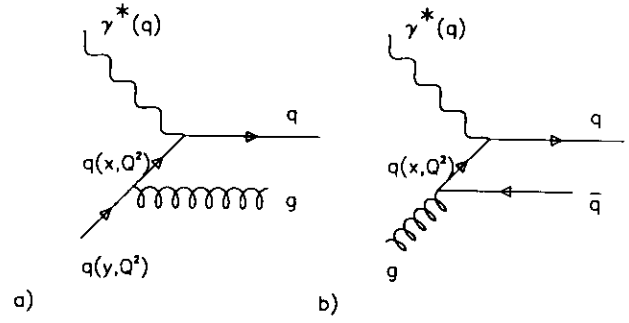

Figure 8-2 Lowest order processes resulting in a non zero F_L. a) Gluon bremsstrahlung before interaction with the photon probe. b) Gluon produces a quark-anti-quark pair.

reduces the bin cross section with respect to assuming F_L=0. Figure 8-3 illustrates the effect of F_L^{QCD} on the measurement of F_2. The dashed lines give the (measured) values of $F_2 - y^2F_L^{QCD}/Y_+$. The measured cross section should be corrected for this effect to obtain the true F_2 (shown by the solid curves). At large y (small x values) the F_L contribution becomes significant.

8.3 Radiative Corrections

QED radiative corrections are known to significantly affect distributions of observed physical quantities in high energy physics. The pioneer work done by Mo and Tsai [72] played a major role in the earlier analysis of fixed target elastic and inelastic *ep* and μp scattering. The corresponding QED corrections for neutral and charged current interactions at HERA have been calculated complete in $O(\alpha)$ by several independent groups in the references listed in [73] [74] [75].

The first order electroweak radiative corrections at HERA are dominated by QED effects. For deep inelastic neutral current events, these corrections were shown to be large

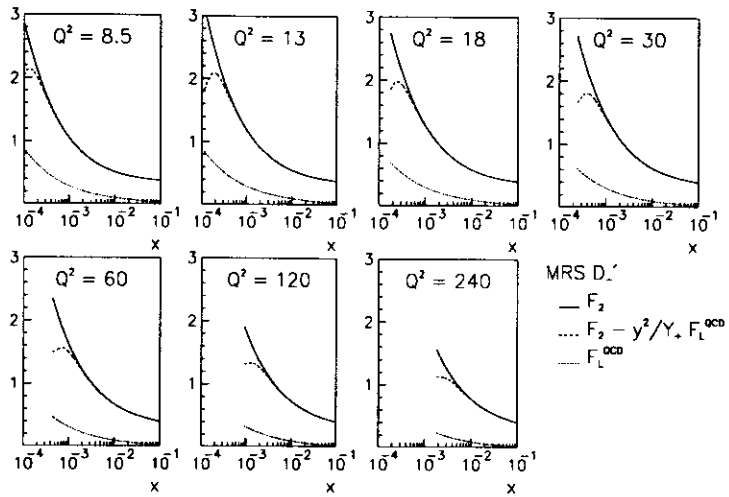

Figure 8-3 Plot showing the F_L^{QCD} contribution to the proton structure function F_2 for each of the selected x,Q^2 bins.

particularly in the low x and high y region [75]. They are dominated by contributions arising from the radiation of real and virtual photons from the lepton line and self energy corrections to the photon propagator [76]. The first order diagrams describing the leptonic corrections as well as the fermionic contributions to the photon self energy (vacuum polarization) are shown in Figure 8-4. The bremsstrahlung processes with an additional photon in the final state are represented by the diagrams Figure 8-4a and Figure 8-4b. The virtual loop correction as well as the fermion loop dominated self energy correction are also significant.

The emission of energy via photon bremsstrahlung from the lepton line can shift the effective momentum transfer at the hadronic vertex to values much smaller than the momentum transfer measured from the momentum of the scattered electron. This leads to a miscalculation of the kinematical quantities discussed in Sec. 5.3, and consequently the

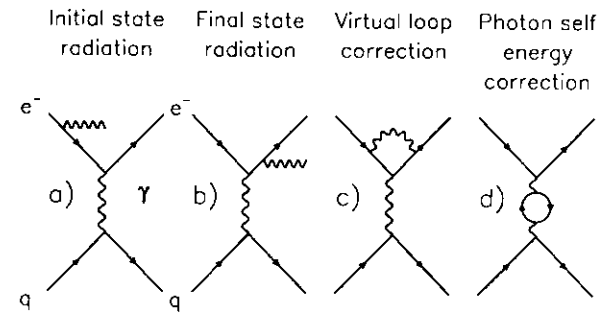

Figure 8-4 First order QED diagrams contributing to the radiative corrections in deep inelastic neutral current interactions with a single virtual photon exchanged.

measured cross section is different from the Born cross section,

$$\frac{d^2\sigma^{measured}}{dxdQ^2} = \frac{d^2\sigma^{Born}}{dxdQ^2}\left[1+\delta^{rad}(x,Q^2)\right]. \qquad (8\text{-}14)$$

The Born cross section contains the information on the internal structure of the particle being probed, and thus it is necessary to separate it from the radiative effects.

The effect of QED radiation on the measured distributions depends on the method used to reconstruct the kinematic variables x and y as shown in Figure 8-5. The size of the QED leptonic corrections, $\delta^{rad}(x,Q^2)$, are shown in Figure 8-5a for different x values as a function of y when cross sections are evaluated from the scattered electron. These corrections are in general much smaller when reconstructing the kinematics using the hadronic, mixed or double angle variables. Using hadronic information with the Jacquet-Blondel variables, the corrections are of the order of -10% with only a slight dependence on x and y as seen in Figure 8-5b). They reach about -20% only at very large y.

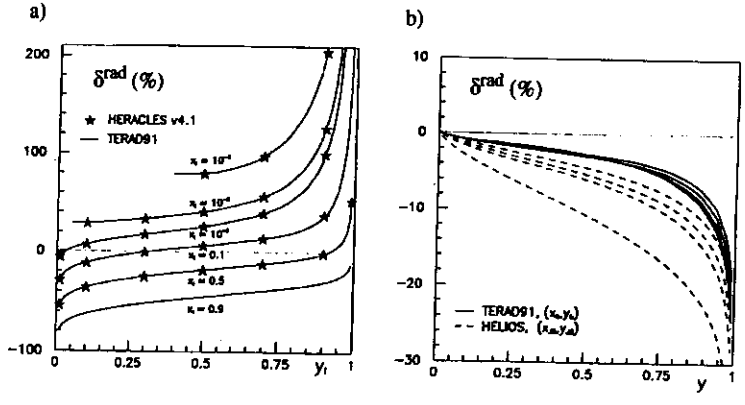

Figure 8-5 As presented in [76] the O(α) leptonic corrections to the Born differential cross section evaluated using a) the electron momenta only (the stars are from the MC simulation program HERACLES [49] discussed in Sec. 4). b) Jacquet-Blondel variables. The full and dashed lines (from top to bottom x = .001, .01, .1 and .5) represent the calculations obtained from the analytical programs TERAD91 [77] and HELIOS [78].

8.4 Selection of x, Q^2 Bins

Measurement resolutions in x and Q^2 determine the bin sizes one can use in the extraction of F_2. The bin sizes were chosen such that

$$\Delta x \geq \sigma_x(x, Q^2)$$
$$\Delta Q^2 \geq \sigma_{Q^2}(x, Q^2) \qquad (8\text{-}15)$$

where σ_x and σ_{Q^2} are the measurement resolutions in x and Q^2 respectively. For higher values of Q^2, larger bin sizes are needed because of the limited statistics in the data. Due to the systematic shift in the (DA) reconstructed x, Q^2 values arising from hadronic energy losses, as shown in Figure 8-6, it was necessary to choose larger bin widths in a previous F_2 measurement presented in [32]. Applying the hadronic energy corrections discussed in Sec. 6 greatly reduces this systematic shift in x for the region in which the structure function measurement is made (denoted by regions B and E for Q^2 and x respectively in

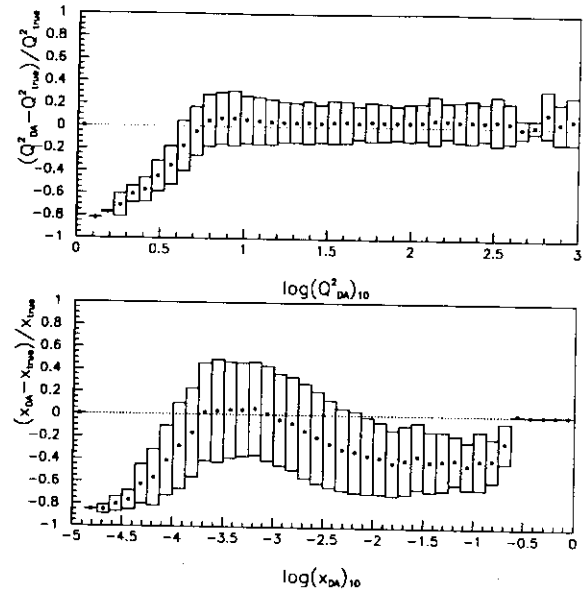

Figure 8-6 The fractional difference between the reconstructed and true x,Q^2 values plotted as a function of the reconstructed value using DA method before applying the hadronic energy corrections. The mean values are shown as the dots and the RMS are given by the lengths of the rectangles.

Figure 8-7). In addition, the resolutions in x and Q^2 are also slightly improved for most of the phase space. The relative resolution is better than 30% in Q^2 and better than 50% in x.

The kinematic region in which F_2 can be measured is confined to a region in x and Q^2 where the systematic errors, smearing and migration effects are reasonably small. The lower limit in x was chosen to be 3×10^{-4}. In addition measurements cannot go beyond $x > 0.1$ due to limited statistics. In Figure 8-8 the trigger efficiency for NC events is shown as a function of Q^2 using the MC sample described in Sec. 4. For events with Q^2 values greater than ~ 6 GeV^2 the efficiency is greater than 95%. However to ensure that the sample does not have large acceptance effects a lower limit of $Q^2 = 7.75$ GeV^2 was used.

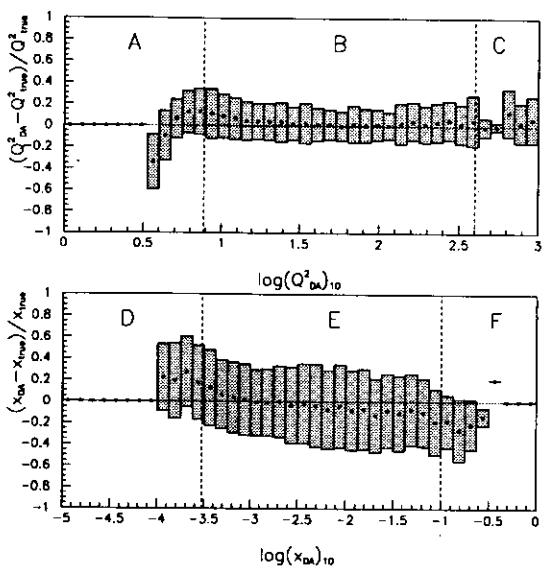

Figure 8-7 The fractional difference between the reconstructed and true x,Q^2 values plotted as a function of the reconstructed value using double angle method after applying the hadronic energy corrections. The mean values are shown as the dots and the rms are given by the lengths of the rectangles.

The distribution of the data events passing the DIS selection criteria (described in Sec. 7.4) is shown Figure 8-9 together with the bins used in this analysis. There are seven different Q^2 bins centered at 8.5, 13, 18, 30, 60, 120 and 240 GeV^2.

Using the DIS MC sample, the quality of the measurement in each of the x and Q^2 bins can be determined by the degree of smearing and the size of the bin correction. For the (x,Q^2) bin denoted by (j,k) the smearing is defined as

$$smearing\ (j,k) = \frac{\text{Number of events in bin } (j,k) \text{ which originated in } (j,k)}{\text{Number of events generated in } (j,k)} \quad (8\text{-}16)$$

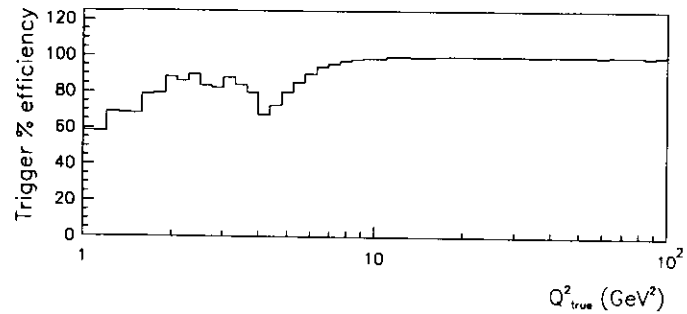

Figure 8-8 Trigger efficiency as a function of Q^2 for neutral current events using the DIS MC sample.

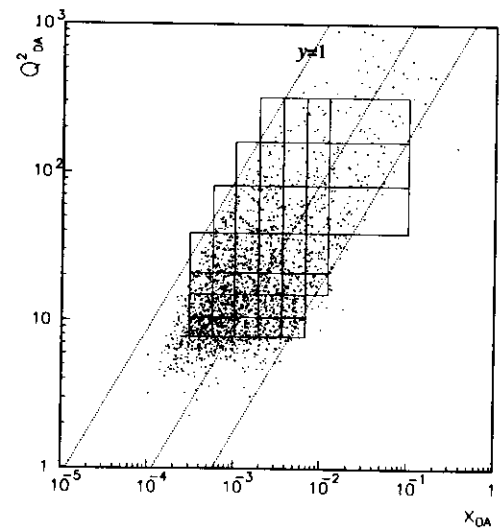

Figure 8-9 The (x,Q^2) distribution of the events from the data satisfying the final selection criteria using the DA method are shown with the bins used in this analysis. The bin sizes are determined by resolutions in x and Q^2 as well as the statistics. Lines of constant y values 1, 0.1, and 0.02 are shown.

and the bin correction is defined as

$$correction\,(j,k) = \frac{\text{Number of events generated in bin } (j,k)}{\text{Number of events measured in } (j,k)}. \qquad (8\text{-}17)$$

Ideally these quantities would have values equal to 1. However as discussed previously in Sec. 5.2, detector effects, measurement errors on the final state energies and angles and event losses due to the selection criteria give rise to smearing effects and event migration. A quality requirement is imposed on each of the bins such that the smearing is greater than 0.14 and the correction factor is between 0.4 and 2.0. The smearing and correction factors for the bins passing these requirements are shown in Figure 8-10. Smearing values lower than 1 indicate event losses through migration or selection criteria. By definition the smearing cannot be greater than 1. Correction factors lower than 1 indicate a net migration of events into the bin while values greater than 1 correspond to a net migration of events out of the bin. For the selected bins a value of F_2 is then determined using the unfolding method described in the next section.

8.5 Description of the Unfolding Method

The distributions of experimentally measured quantities differ from their corresponding "true" distributions due to various physics and detector effects. These effects include the limited detector acceptance and resolution, trigger and reconstruction efficiencies, selection cuts, QED radiative corrections, and QCD effects. All these effects combine such that: a) the probability of observing a given event is less than one varying over the kinematical region, and b) a quantity can only be determined within measurement errors. Hence the objective is to unfold the distorted measured quantities from these effects to determine their true distributions.

The method used in this analysis [79] uses the following quantities for a given bin centered around (x,Q^2) denoted by (j,k):

- $N(j,k)$ is the number of events generated in the MC
- $M(j,k)$ is the number of events measured after smearing and selection cuts in the MC
- $m(l,m,j,k)$ is the number of events generated in (l,m) measured in (j,k) in the MC

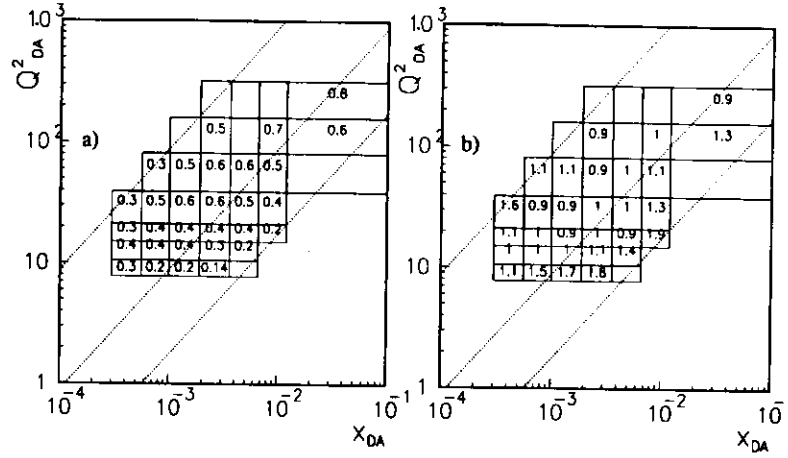

Figure 8-10 Size of the smearing and corrections factors in the bins. The a) smearing and b) correction factors for the bins containing at least 10 events and passing the quality requirement. Smearing values lower than 1 indicate event losses through migration or selection cuts. Correction factors lower than 1 indicate a net migration of events into the bin while values greater than 1 correspond to a net migration of events out of the bin.

- $D(j,k)$ is the number of events measured after smearing and selection cuts in the data.

Using the MC simulation the quantity defined by

$$f(l,m,j,k) = \frac{m(l,m,j,k)}{N(l,m)} \qquad (8\text{-}18)$$

can be determined. This quantity gives a measure of the probability that an event generated in bin (l,m) will be reconstructed in bin (j,k). It describes the detector response as well as the acceptance, smearing and migration of the events in the bins. The bin correction factor defined in the previous section is obtained by the ratio

$$correction\,(j,k) = \frac{N(j,k)}{M(j,k)} = R(j,k). \qquad (8\text{-}19)$$

This factor is an overall acceptance correction for the bin (j,k) and is used to determine the true distribution from the measured distribution. As shown in Figure 8-10b) these factors are close to 1 for most bins except those with the lowest y and lowest Q^2 values.

An iterative procedure is used to unfold the measured distributions. The MC simulation is normalized to the number of events in the data within the well measured region as

$$[T(j,k)]_{i+1} = [T(j,k)]_i \frac{\sum_{\Omega} D(j,k)}{\sum_{\Omega} [M(j,k)]_i} \tag{8-20}$$

where

$$\begin{aligned} [T(j,k)]_0 &= N(j,k) \\ [M(j,k)]_0 &= M(j,k) \\ [M(j,k)]_{i+1} &= \sum_{l,m} [T(j,k)]_{i+1} f(l,m,j,k) \end{aligned} \tag{8-21}$$

and Ω is summed over the bin (j,k). For the ith iteration a χ^2 is determined from

$$\chi_i^2 = \frac{1}{N_{bins}} \left[\frac{D(j,k) - [M(j,k)]_{i+1}}{Err(j,k)} \right]^2 \tag{8-22}$$

where $Err(j,k)$ is calculated from

$$Err(j,k) = \sqrt{\frac{1}{D(j,k)} + \left[\frac{\delta R(j,k)}{R(j,k)} \right]^2}, \tag{8-23}$$

and

$$R(j,k) = \frac{N(j,k)}{M(j,k)} = \frac{N_{out} + M_{in}}{M_{out} + M_{in}}. \tag{8-24}$$

The iteration continues as long as the condition

$$\frac{|\chi_i^2 - \chi_{i-1}^2|}{\chi_{i-1}^2} > cutoff \tag{8-25}$$

is true. In the analysis the cutoff was chosen at 10, requiring only one iteration. The expected distribution from the data is then given by $[T(j,k)]_{final}$ such that

$$\int_k \int_j \left[\frac{d^2\sigma^{measured}}{dxdQ^2} \right] dxdQ^2 = \frac{[T(j,k)]_{final}}{\mathcal{L}_{data}} \tag{8-26}$$

where the integration is performed over the limits of bin (j,k). The ratio R which is the correction factor for bin (j,k) can be expressed in terms of the quantities N_{out}, M_{out}, M_{in} defined as the number of events generated but not measured in (j,k), the number of events measured in (j,k) which originated from the surrounding bins and the number of events generated and measured in (j,k) respectively. These quantities should be uncorrelated and the error on R obtained is

$$\delta^2 R(j,k) = \frac{\delta^2 N_{out}}{(M_{out} + M_{in})^2} + \frac{(M_{out} - N_{out})^2}{(M_{out} + M_{in})^4} \delta^2 M_{in} + \frac{(N_{out} + M_{in})^2}{(M_{out} + M_{in})^4} \delta^2 M_{out}. \tag{8-27}$$

The measured differential cross section given in Eq. (8-14) including the QED radiative corrections is

$$\frac{d^2\sigma^{measured}}{dxdQ^2} = \frac{2\pi\alpha^2}{xQ^4} [1 + (1-y^2)] F_2(x,Q^2) (1 + \delta^{rad}(x,Q^2)). \tag{8-28}$$

Although the radiative corrections strongly depend on the way the kinematic variables are defined they are independent of the true x,Q^2. The approximation

$$\frac{d^2\sigma_1^{measured}/dxdQ^2}{d^2\sigma_2^{measured}/dxdQ^2} = \frac{F_2^1(x,Q^2)}{F_2^2(x,Q^2)} \tag{8-29}$$

relating the values of F_2 obtained from two different parametrizations (in this case, the data and MC) is then be valid. Finally value of F_2 for the bin (j,k) is obtained from

$$F_2^{data}(x,Q^2) = \frac{[T(j,k)]_{final}/\mathcal{L}_{data}}{(N(j,k))/\mathcal{L}_{MC}} F_2^{MC}(x,Q^2) \quad . \tag{8-30}$$

8.6 Systematic Checks

Several categories were identified which could lead to systematic errors in the proton structure function measurement:

- SC1 - Electron energy scale
- SC2 - Hadronic energy scale
- SC3 - Electron position determination
- SC4 - Calorimeter noise effects
- SC5 - F_L^{QCD} dependence on the input structure function
- SC6 - Backgrounds
- SC7 - Radiative Effects
- Luminosity determination
- Event selection

The first two categories address the present understanding of the electron and hadronic energy scales (see Sec. 4.1 and Sec. 6.1). To understand the energy scales to within a few percent requires that the calorimeter response to both electron and hadrons be well simulated in the MC. This also requires the proper description of the inactive material between the interaction point and the calorimeter over the entire solid angle. An inaccurate simulation of the shower profiles and the dead material would lead to different efficiencies in the data and MC. These categories were checked by assuming a generously large disagreement for the electron (SC1) and hadronic (SC2) scales. Energies were shifted by $\pm 10\%$ in the MC. The sensitivity of the DA reconstruction method to the electron energy scale is negligible for most bins but reached up to 12% in the lowest x bins. For the hadronic scale the effect is small in most bins but reached 15% in the high Q^2 bins.

The determination of the impact position of the electron (SC3) on the calorimeter (described in Sec. 7.2) would also contribute to the systematic error. This was checked by shifting the z vertex in the Monte Carlo by ± 5 *cm*. This corresponds to the resolution of the electron scattering angle of about 5 *mrad*. The angles, particle momenta, and the kinematic variables were recalculated, after which the selection criteria in Sec. 7.4 were reapplied. The larger of the two errors was taken. Systematic effects of up to 14% were observed in the lowest x and Q^2 bins.

There is also the effect of calorimeter noise (SC4) on the reconstruction of the kinematic variables (described in Sec. 5.4). The hadronic variables are particularly sensitive to calorimeter noise in the very small-y region. Thus, the systematics due to noise was checked by changing the y_{JB} cut. In both the data and the MC the y_{JB} cut was lowered to 0.01, affecting the migration, smearing and acceptance of the events only in the bins with lowest y values up to 30%.

Another source of systematic error is the dependence of F_L^{QCD} on the input structure function (SC5). This was checked by using MRSD_0' to obtain the F_L corrections for each x and Q^2 bin. MRSD_0' assumes a flat gluon distribution compared to the $x^{-0.5}$ behavior in the MRSD_-' parametrization. The largest systematic error of up to 15% were observed in the lowest x and large y bins.

The remaining background in the data sample (SC6) could also affect the F_2 measurement. In general, the background consisting of cosmic and halo muons, elastic QED Comptons and electron beam-gas events do not have a reconstructed vertex. To estimate the systematic error due to this category, events which did not have at least 2 reconstructed tracks or a $\chi^2/\text{ndf} < 10$ were rejected. In most bins this effect is small but reached up to 10% in some bins. The systematic uncertainties arising from the photoproduction background was studied by using two different electron finding algorithms (see Sec. 7.5.1). The differences in the extracted F_2 were, in general, small for most of the bins except the lowest x bins where effects oup to 8% were seen.

Radiative effects (SC7) were simulated in the MC using the HERACLES program described in Sec. 4. The corrections to the measured cross section from radiative effects would also contribute to the systematic errors. This category was checked by adjusting the weights of radiative events, particularly initial state radiation events, in the MC by $\pm 10\%$. An average change in F_2 of about 7% was observed in all the bins.

Finally the systematics due to the errors in the luminosity determination (Sec. 7.1) and event losses due to the detector acceptance, trigger efficiency, and the NC selection criteria (Sec. 7.4) result in an overall normalization uncertainty of 7%.

Table 8-1 summarizes the results of the systematic checks. The errors in each bin were added in quadrature to obtain the total systematic error listed in the last column. These do not include the 7% global normalization uncertainty.

8.7 Presentation of the Results

The measured proton structure function, $F_2(x,Q^2)$, as a function of x for different Q^2 values is presented in Figure 8-11, and as a function of Q^2 for the different x values in Figure 8-12. The statistical are shown as the inner error bars, while the systematic errors added in quadrature to the statistical errors, are shown as the outer error bars. The overall normalization uncertainty of 7% due to the errors in the luminosity measurement and event losses is not included.

The final results are summarized in Table 8-2. For each x and Q^2 bin, the estimated number of background events as well as the F_L values used in the F_2 measurement are also given. A total of 1820 events are measured in the bins with an estimated total background of 44 events. The bin with the largest background occurs for the lowest x bin at $Q^2 = 120\ GeV^2$. In this bins the background from photoproduction is estimated to be about 26%. The background events were subtracted from the bins in the analysis. The values used to correct for F_L were obtained using the expectation from QCD as discussed in Sec. 8.2. These F_L corrections reduce the cross section by at most 13% relative to assuming F_L=0 in Eq. (8-9).

8.8 Measurement of $G(x)$ at Low x Using F_2 Scaling Violation

The gluon distribution cannot be directly measured in deep inelastic lepton-hadron scattering since gluons do not carry weak or electric charge. However, there are methods to indirectly measure the gluons in the nucleon [69] [80] [81]. The method used in this analysis was proposed in [81]. It assumes that at small values[1] of the Bjorken scaling variable x, the QCD predicted F_2 scaling violation arises mainly from the gluon density. This method will be discussed in more detail in the following section.

1. Small x is taken to be $x < 0.01$ [81].

Q^2 (GeV^2)	x	F_2 Nom.	SC1 (%)	SC2 (%)	SC3 (%)	SC4 (%)	SC5 (%)	SC6 (%)	SC7 (%)	Total (%)
8.5	4.1×10^{-4}	1.13	0.0	2.7	12.4	0.0	14.2	2.7	7.1	20
	7.5×10^{-4}	1.06	0.0	1.9	6.6	0.9	11.3	1.9	6.6	15
	1.4×10^{-3}	0.93	0.0	2.2	12.9	1.1	3.2	10.8	6.5	19
	2.6×10^{-3}	0.73	0.0	11.0	13.7	13.7	1.4	2.7	6.8	24
13	4.2×10^{-4}	1.23	0.0	0.8	4.9	0.0	8.9	1.6	6.5	12
	7.5×10^{-4}	1.04	0.0	3.8	7.7	0.0	6.7	5.8	6.7	14
	1.4×10^{-3}	0.86	1.2	1.2	2.3	0.0	5.8	2.3	7.0	10
	2.6×10^{-3}	0.77	0.0	0.0	3.9	3.9	1.3	5.2	6.5	10
	4.9×10^{-3}	0.67	0.0	4.5	6.0	28.4	6.0	1.5	6.0	31
18	4.2×10^{-4}	1.32	3.8	1.5	12.9	0.0	4.5	3.8	6.1	16
	7.5×10^{-4}	1.24	0.0	1.6	12.1	0.8	3.2	4.8	6.5	15
	1.4×10^{-3}	0.96	0.0	0.0	14.6	0.0	5.2	1.0	6.3	17
	2.6×10^{-3}	0.68	0.0	1.5	5.9	0.0	0.0	1.5	5.9	9
	4.9×10^{-3}	0.57	0.0	5.3	12.3	15.8	1.8	3.5	7.0	22
	8.9×10^{-3}	0.50	0.0	4.0	4.0	0.0	4.0	0.0	6.0	9
30	4.2×10^{-4}	1.41	8.5	9.2	5.7	0.0	2.1	2.8	6.4	16
	7.5×10^{-4}	1.69	0.6	3.6	7.1	0.0	0.0	3.6	6.5	11
	1.4×10^{-3}	1.25	0.0	1.6	8.8	0.0	2.4	0.8	7.2	12
	2.6×10^{-3}	0.96	0.0	0.0	9.4	0.0	1.0	0.0	6.3	11
	4.9×10^{-3}	0.65	0.0	7.7	1.5	4.6	0.0	0.0	6.2	11
	8.9×10^{-3}	0.58	0.0	1.7	10.3	22.4	1.7	1.7	6.9	26
60	7.5×10^{-4}	1.61	11.8	1.9	6.8	0.0	7.5	8.1	6.2	19
	1.4×10^{-3}	1.44	0.7	2.8	9.0	0.0	2.1	2.1	6.2	12
	2.6×10^{-3}	1.21	0.0	1.7	7.4	0.8	0.0	1.7	5.8	10
	4.9×10^{-3}	0.78	0.0	2.6	9.0	0.0	1.3	0.0	6.4	11
	8.9×10^{-3}	0.75	0.0	4.0	5.3	1.3	1.3	0.0	6.7	10
120	2.6×10^{-3}	1.26	0.0	1.6	12.7	0.0	4.0	0.0	5.6	14
	8.9×10^{-3}	0.73	0.0	1.4	8.2	0.0	1.4	0.0	5.5	10
	3.5×10^{-2}	0.48	0.0	14.6	6.3	4.2	2.1	0.0	8.3	19
240	3.5×10^{-2}	0.50	0.0	8.0	10.0	4.0	2.0	0.0	8.0	16

Table 8-1 Summary of the results of the systematic checks SC1-SC7 (in percent). The total systematic error listed in the last column is obtained by adding each error in quadrature. The given nominal value for F_2 is corrected for F_L and the photoproduction background.

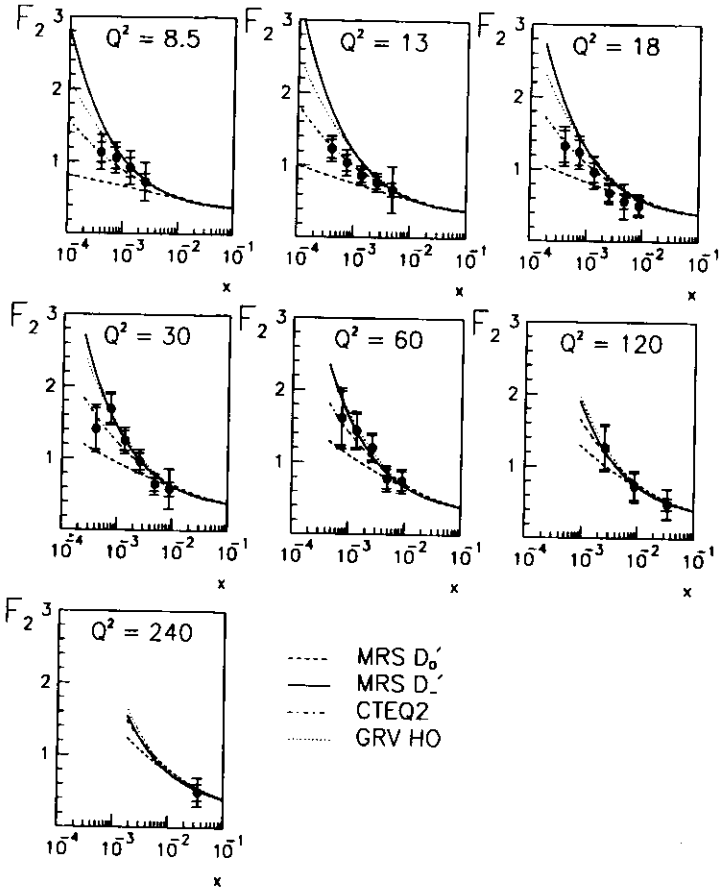

Figure 8-11 The measured values of the proton structure function F_2 as a function of x for Q^2 values at 8.5, 13, 18, 30, 60, 120 and 240 GeV^2. Also shown are the expectations obtained from the parametrizations discussed in Sec. 1.5. The statistical and systematic errors represented by the inner and outer error bars are added in quadrature. The 7% global normalization uncertainty due to the errors in the luminosity measurement and event losses is not included.

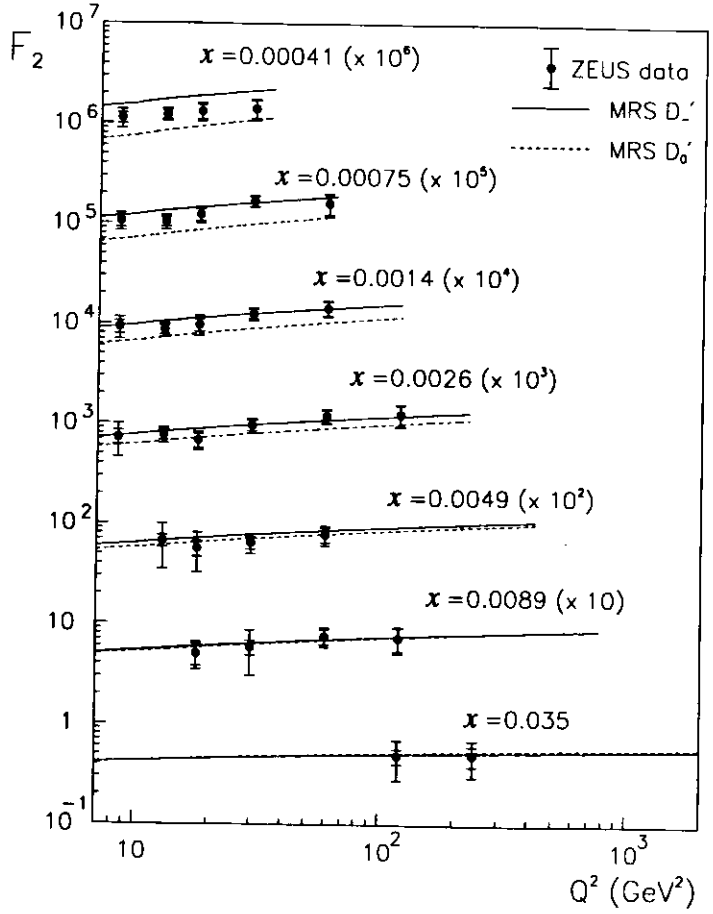

Figure 8-12 The values of the proton structure function F_2 as a function of Q^2 for different x values at .00041, .00075, .0014, .0026, .0049, .0089 and .035 are shown with the expectations from MRS D_0' and MRS D_-' parametrizations. Shown are the statistical errors (inner error bars) and the systematic errors added in quadrature (outer error bars). The 7% global uncertainty due to the errors in the luminosity measurement and event losses has not been included.

Q^2 (GeV^2)	x	# Events	Back-ground	F_L corr.	σ^{meas} ± stat	Measured F_2 ± stat ± sys
8.5	4.1×10^{-4}	101	2±1	1.012	4.33 ± 0.54	1.13 ± 12% ± 20%
	7.5×10^{-4}	82	10±10	1.003	4.37 ± 0.62	1.06 ± 14% ± 15%
	1.4×10^{-3}	63	0	1.001	4.22 ± 0.62	0.93 ± 15% ± 19%
	2.6×10^{-3}	50	0	1.000	3.68 ± 0.59	0.73 ± 16% ± 24%
13	4.2×10^{-4}	125	3±2	1.026	4.89 ± 0.52	1.23 ± 11% ± 12%
	7.5×10^{-4}	129	10±10	1.006	4.69 ± 0.49	1.04 ± 11% ± 14%
	1.4×10^{-3}	117	0	1.002	4.81 ± 0.50	0.86 ± 10% ± 10%
	2.6×10^{-3}	102	0	1.000	4.64 ± 0.51	0.77 ± 12% ± 10%
	4.9×10^{-3}	67	0	1.000	3.91 ± 0.53	0.67 ± 13% ± 31%
18	4.2×10^{-4}	50	3±2	1.059	2.11 ± 0.35	1.32 ± 17% ± 16%
	7.5×10^{-4}	64	1±1	1.013	2.58 ± 0.37	1.24 ± 14% ± 15%
	1.4×10^{-3}	63	0	1.003	2.36 ± 0.34	0.96 ± 15% ± 17%
	2.6×10^{-3}	44	0	1.001	1.78 ± 0.29	0.68 ± 16% ± 9%
	4.9×10^{-3}	37	0	1.000	1.38 ± 0.25	0.57 ± 18% ± 22%
	8.9×10^{-3}	19	0	1.000	1.47 ± 0.36	0.50 ± 24% ± 9%
30	4.2×10^{-4}	32	3±2	1.133	1.85 ± 0.38	1.41 ± 21% ± 16%
	7.5×10^{-4}	93	2±1	1.036	3.32 ± 0.40	1.69 ± 12% ± 11%
	1.4×10^{-3}	99	0	1.008	3.69 ± 0.41	1.25 ± 11% ± 12%
	2.6×10^{-3}	80	0	1.002	3.18 ± 0.38	0.96 ± 12% ± 11%
	4.9×10^{-3}	54	0	1.000	2.13 ± 0.31	0.65 ± 14% ± 11%
	8.9×10^{-3}	41	0	1.000	2.09 ± 0.35	0.58 ± 17% ± 26%
60	7.5×10^{-4}	31	2±1	1.121	1.13 ± 0.26	1.61 ± 23% ± 19%
	1.4×10^{-3}	49	2±1	1.037	2.08 ± 0.34	1.44 ± 16% ± 12%
	2.6×10^{-3}	56	0	1.008	2.11 ± 0.30	1.21 ± 14% ± 10%
	4.9×10^{-3}	39	0	1.002	1.64 ± 0.28	0.78 ± 17% ± 11%
	8.9×10^{-3}	37	0	1.000	1.69 ± 0.29	0.75 ± 17% ± 10%
120	2.6×10^{-3}	23	6±2	1.036	0.84 ± 0.32	1.26 ± 24% ± 14%
	8.9×10^{-3}	16	0	1.002	0.64 ± 0.17	0.73 ± 26% ± 10%
	3.5×10^{-2}	36	0	1.000	1.84 ± 0.32	0.48 ± 17% ± 19%
240	3.5×10^{-2}	21	0	1.001	0.74 ± 0.17	0.50 ± 22% ± 16%

Table 8-2 Summary of the proton structure function measurement. The measured cross sections with the statistical errors and the values of F_2 after correcting for F_L and the photoproduction background, are given with the statistical and systematic errors. For each bin the event distribution, the number of events for the estimated background, and the values for the F_L corrections are given.

Scale breaking in deep inelastic scattering gives rise to measured structure functions which have a Q^2 dependence at fixed x. The lowest order diagrams in deep inelastic lepton-hadron scattering which contribute to $dF_2(x,Q^2) / dlnQ^2$ as predicted by the Altarelli-Parisi evolution equation are shown below. In Figure 8-2a, a quark with momentum fraction x interacts with the current $\gamma^*(q)$ and is shown as originating from a quark with momentum fraction y. The gluon radiated carries momentum fraction y-x. In Figure 8-2b, an initial state gluon produces a quark and antiquark pair, one of which interacts with the virtual photon.

The Q^2 evolution of the flavor singlet quark densities is given by the DGLAP equation. To leading order, this is given by

$$\frac{dq_i(x,Q^2)}{dlnQ^2} = \frac{\alpha_s(Q^2)}{2\pi}\int_x^1 \frac{dy}{y}\left[P_{qq}\left(\frac{x}{y}\right) q_i(y,Q^2) + P_{qg}\left(\frac{x}{y}\right) g(y,Q^2)\right]. \qquad (8\text{-}31)$$

The gluon bremsstrahlung diagram illustrated in Figure 8-2a contributes to the first term in Eq. (8-31). The quantity $\alpha_s P_{qq}(x/y)$ gives the probability that a quark with momentum fraction x could have come from an initial state quark with momentum fraction y which has radiated a gluon. The second term in Eq. (8-31) arises from the $q\bar{q}$ pair production diagram in Figure 8-2b. The quantity $\alpha_s P_{qg}(x/y)$ gives the probability of finding a quark with momentum fraction x could have come from a $q\bar{q}$ pair created by a gluon. In leading order, the QCD coupling constant is given by

$$\alpha_s(Q^2) = \frac{12\pi}{(33-2N_f)\,ln\,(Q^2/\Lambda^2)} \qquad (8\text{-}32)$$

where N_f is the number of quark flavors and Λ is the QCD parameter.

8.9 Extraction of the Gluon Density using F_2 Scaling Violation

At low x, the lowest order diagram shown in Figure 8-2b) is the dominant source of the scaling violation of the structure function F_2. In terms of F_2, where

$$F_2(x,Q^2) = x\sum_i e_i^2 q_i(x,Q^2), \qquad (8\text{-}33)$$

the Altarelli-Parisi evolution will then consist only of the term involving the gluon density,

$$\frac{dF_2(x,Q^2)}{dlnQ^2} \approx \sum_i e_i^2 \frac{\alpha_s(Q^2)}{2\pi} x \int_x^1 \frac{dy}{y} P_{qg}(\frac{x}{y})\, g(y,Q^2) \qquad (8\text{-}34)$$

where e_i is the charge of the ith quark and i is summed over all quarks and antiquarks. One can make the variable substitution $y=x/(1-z)$ in Eq. (8-34) and get

$$\frac{dF_2(x,Q^2)}{dlnQ^2} \approx \sum_i e_i^2 \frac{\alpha_s(Q^2)}{2\pi} \int_0^{(1-x)} P_{qg}(1-z)\,(\frac{x}{1-z})\, g(\frac{x}{1-z},Q^2)\, dz. \qquad (8\text{-}35)$$

In leading order,

$$P_{qg}(u) = \frac{1}{2}\left[(1-u)^2+u^2\right] \qquad (8\text{-}36)$$

and therefore

$$P_{qg}(u) = P_{qg}(1-u) \qquad (8\text{-}37)$$

so that P_{qg} is symmetric around $u = 1/2$ in lowest order. In Eq. (8-35) the gluon distribution G, can be written in terms of the gluon density $g(x/(1-z),Q^2)$.

$$(\frac{x}{1-z})\, g(\frac{x}{1-z},Q^2) = G(\frac{x}{1-z},Q^2) \qquad (8\text{-}38)$$

Hence, Eq. (8-35) becomes

$$\frac{dF_2(x,Q^2)}{dlnQ^2} \approx \sum_i e_i^2 \frac{\alpha_s(Q^2)}{2\pi} \int_0^{(1-x)} P_{qg}(z)\, G(\frac{x}{1-z},Q^2)\, dz. \qquad (8\text{-}39)$$

The gluon distribution can be expanded around $z = 1/2$ in a Taylor series,

$$G(\frac{x}{1-z}) \approx G(z=\frac{1}{2}) + (z-\frac{1}{2})\, G'(z=\frac{1}{2}) + \frac{(z-1/2)^2}{2} G''(z=\frac{1}{2}) + \ldots. \qquad (8\text{-}40)$$

Inserting this expression in Eq. (8-39) and approximating the upper limit of the integral to be 1 for small x, the second term in this series vanishes since the splitting function $P_{qg}(z)$ is symmetric around $z = 1/2$. Using a trial function of the general form $G(w) = w^d(1-w)^a$ for the gluon distribution, the third and higher ordered terms in this expansion are small and can be neglected [81]. The integral equation in Eq. (8-39) then becomes

$$\frac{dF_2(x,Q^2)}{dlnQ^2} \approx \sum_i e_i^2 \frac{\alpha_s(Q^2)}{2\pi} \frac{1}{3} G(2x,Q^2). \qquad (8\text{-}41)$$

This equation relates the gluon distribution at $2x$ to the slope of the proton structure function $F_2(x,Q^2)$ at x. Finally, the gluon distribution in terms of the measurable quantity $dF_2(x,Q^2) / dlnQ^2$ for the number of quark flavors $N_f=4$ in leading order is

$$G(2x,Q^2) \approx \frac{27\pi}{10\alpha_s(Q^2)} \left(\frac{dF_2(x,Q^2)}{dlnQ^2}\right). \qquad (8\text{-}42)$$

The accuracy of approximating Eq. (8-34) with Eq. (8-42) can be checked for possible values of d, using the trial function of the form $G(w) = w^d(1-w)^a$. For a reasonable range of δ, $-1.2<\delta<0.2$, it can be shown that the approximation in Eq. (8-41) is better than 10%.

8.9.1 The Gluon Distribution using the F_2 Results

The final results of this F_2 analysis has been presented in the previous section. In Figure 8-12 the proton structure function is plotted as a function of Q^2 for different values of the scaling variable x. For each x, the value of F_2 is multiplied by the factor shown in parenthesis. The observed dependence of F_2 on Q^2 is in accord with the scaling violation predicted by QCD.

The measurement was done to maximize the number of x bins without performing any extrapolation. The bins in x,Q^2 chosen are given by $13\ GeV^2 \le Q^2 \le 60\ GeV^2$ and $0.00075 \le x \le 0.0049$. The logarithmic mean in Q^2 of the F_2 data points in this region is $28\ GeV^2$. For each x bin, the slope $dF_2(x,Q^2) / dlnQ^2$ was determined using a straight line fit in lnQ^2 (Figure 8-13).

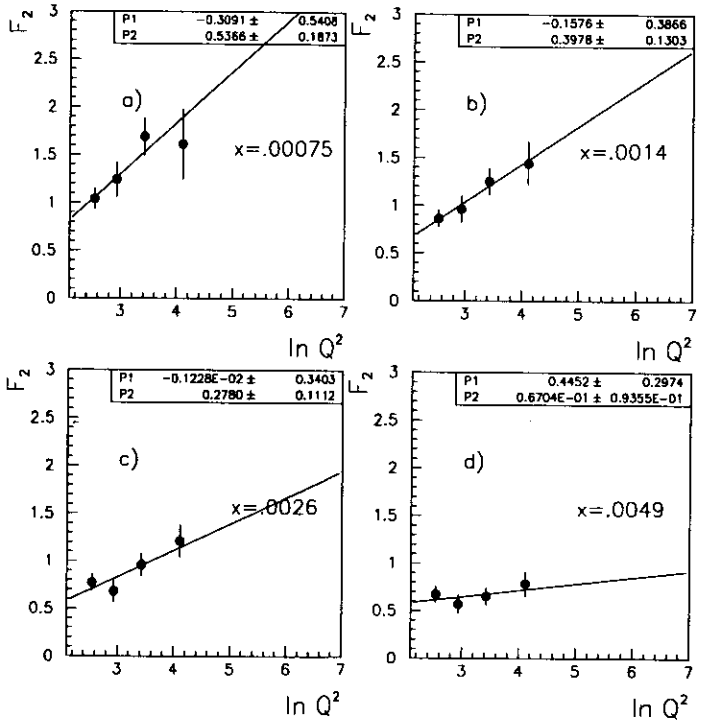

Figure 8-13 The slope $dF_2(x,Q^2) / dlnQ^2$ is determined for each x bin for the nominal F_2 values corrected for F_L and the photoproduction background. The errors shown are the statistical errors.

8.9.2 Systematic Checks

The slope $dF_2(x,Q^2) / dlnQ^2$ was determined separately for each of the systematic checks SC1-SC7 discussed previously in Sec. 8.6. The absolute systematic error for each of these checks, denoted by $(error)_i$, was calculated as

$$(error)_i = \left| \left(\frac{dF_2(x,Q^2)}{dlnQ^2} \right)_{nominal} - \left(\frac{dF_2(x,Q^2)}{dlnQ^2} \right)_i \right| \qquad (8\text{-}43)$$

where the nominal values were obtained using the standard DIS NC event selection discussed in Sec. 7.4, with F_L^{QCD} correction and photoproduction background subtraction. The slopes $dF_2(x,Q^2) / dlnQ^2$ are insensitive to any F_2 systematic shift due to the errors arising from the luminosity measurement. The nominal values of the slopes for each x bin and the results of the systematic checks SC1-SC7 are summarized in Table 8-3. Each of the $(error)_i$ tabulated was added in quadrature to obtain the total systematic error.

8.9.3 Results

The resulting gluon distribution G at $Q^2 = 28\ GeV^2$ is shown in Figure 8-14 with the statistical errors, represented by the inner error bars, and the systematic errors whish were added in quadrature to the statistical errors, represented by the outer error bars. The curves show G the MRS D_0', MRS D_-' and GRV parametrizations. The results are summarized in Table 8-4.

x	$dF_2/dlnQ^2$ nominal	SC1 (%)	SC2 (%)	SC3 (%)	SC4 (%)	SC5 (%)	SC6 (%)	SC7 (%)	Total (%)
7.5×10^{-4}	0.54	15	2	11	0	4	28	6	34
1.4×10^{-3}	0.40	2	8	28	0	5	0	8	38
2.6×10^{-3}	0.28	0	7	18	7	4	7	7	22
4.9×10^{-3}	0.07	0	0	43	17	29	14	14	54

Table 8-3 The summary of the results of the systematic checks SC1-SC7 in the determination of the slope $dF_2/dlnQ^2$ are given for each x bin. The mean Q^2 is 28 GeV^2. The nominal slope for each bin is determined using the final values for F_2 in Table 8-2. Each systematic error was added in quadrature to obtain the total error listed in the last column.

x	$dF_2/dlnQ^2$ nominal	statistical (%)	systematic (%)
7.5×10^{-4}	0.54	35	34
1.4×10^{-3}	0.40	33	38
2.6×10^{-3}	0.28	40	22
4.9×10^{-3}	0.07	140	54

Table 8-4 The nominal slopes $dF_2/dlnQ^2$ at Q^2 = 28 GeV^2 for four different x bins are given with their corresponding statistical and systematic errors.

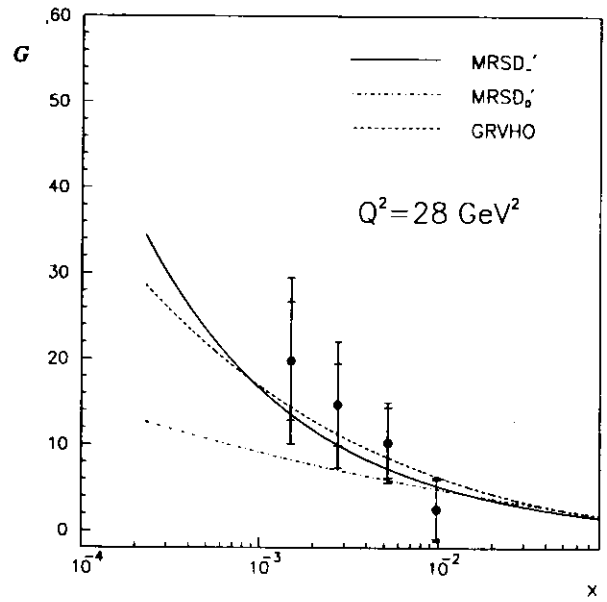

Figure 8-14 The extracted gluon distribution from the scaling violation of the proton structure function at small x using the method presented in [81] for N_f=4 and Λ_{QCD}= 200 *MeV*. Shown are the statistical errors (inner error bars) and the systematic errors added in quadrature (outer error bars) [82].

CHAPTER 9

SUMMARY AND OUTLOOK

This thesis has presented an independent measurement of the proton structure function F_2 and a first determination of the gluon distribution at HERA using the data collected with the ZEUS detector in its first year of data taking in 1992. A careful treatment of the hadronic energy losses (see Sec. 6), which become significantly large at low x, has allowed an improved F_2 measurement with finer bins in x and Q^2.

The F_2 measurement as a function of x are presented in Figure 8-11 for seven different Q^2 bins, with central values of 8.5, 13, 18, 30, 60, 120 and 240 GeV^2 with $0.00042 \leq x \leq 0.035$. The statistical errors, shown as the inner error bars. The systematic errors, added in quadrature to the statistical errors, are shown as the outer error bars. The 7% normalization uncertainty in the luminosity measurement is not included. The final results are summarized in Table 8-2. The systematic errors vary from bin to bin, ranging from 10% to 30%. A strong rise of the proton structure function F_2 is observed with decreasing values of x. The data points lie above the MRS D_0' parametrization which assumes a constant gluon density in the low x region. For the three lower Q^2 bins the points lie below the MRS D_-' extrapolation which assumes a singular Lipatov behavior for the gluon density.

The hadronic final state of deep inelastic events were shown to have a significant energy flow at small angles close to the proton direction [83]. However, a substantial fraction of the events in the data were observed in which there was no significant hadronic energy outside of the current jet region [67] (see discussion in Sec. 7.6). These events comprised ~6% of the final DIS neutral current sample and are included in the measurement of the proton structure function. It was shown in [67] that the fraction of these large rapidity gap events has no significant dependence on x and Q^2 within the errors as shown in Figure 7-30. This suggests that these events play no special role in the strong rise of F_2 in the low x region.

Figure 8-12 shows the F_2 values as a function of Q^2. The observed dependence of F_2 on Q^2 is in accord with the QCD predicted scaling violation. The first determination of the gluon distribution at HERA using the method proposed in [81] is presented [82] in Figure 8-14. There is a strong indication of a rising gluon distribution with decreasing values of x.

A number of additional components to the ZEUS detector has been approved including a preshower detector (presampler) which will be of critical importance in the understanding of the energy scales, and the leading proton spectrometer which will allow the identification of those events in which the proton remnant was undetected in the calorimeter.

Deep inelastic scattering at HERA provides an excellent opportunity to explore the structure of the proton in a completely new kinematic domain. With an improved understanding of the detector and hence the experimental systematic errors involved, the structure function measurement at HERA would allow stringent tests of perturbative QCD in the small x region.

REFERENCES

[1] R. Taylor, *Inelastic Electron-Nucleon Experiments*, Proc. Int'l. Symposium on Lepton and Photon Interactions at High Energy (1975) 679.

[2] HERA, *A Proposal for a large Electron-Proton Colliding Beam Facility at DESY*, Hamburg, (1981).

[3] H1 Collaboration: T. Ahmed et. al., *Observation of Deep Inelastic Scattering at Low x*, Phys. Lett. B 299 (1993) 385.

[4] ZEUS Collaboration: M. Derrick et al., *Initial Study of Deep Inelastic Scattering with ZEUS at HERA*, Phys. Lett. B 303 (1993) 183.

[5] R. Hofstadter and R. W. Mc Allister, *Elastic Scattering of 188-MeV Electrons from the Proton and the Alpha Particle*, Phys. Rev. 102 (1956) 851.
R. Hofstadter and M. R. Yearian, *Magnetic Form Factor of the Neutron*, Phys. Rev. 110 (1958) 552.

[6] G. F. Chew, M. Gell-Mann and A. Rosenfeld, *Strongly Interacting Particles*, Scientific American February 1964.

[7] M. Gell-Mann, *Symmetries of Baryons and Mesons*, Phys. Rev. 125 (1962) 1067.

[8] M. Gell-Mann, *A Schematic Model of Baryon and Mesons*, Phys. Lett. 8 (1964) 214.
G. Zweig, *An SU(3) Model for Strong Interaction Symmetry and Its Breaking*, CERN Report TH 412, Geneva (1964).

[9] O. W. Greenberg, *Spin and Unitary-Spin Independence in a Paraquark Model of Baryons and Mesons*, Phys. Rev. Lett. 13 (1964) 598.

[10] W. K. H. Panofsky, *Low q^2 Electrodynamics, Elastic and Inelastic Electron (and Muon) Scattering*, Proc. of the 14th Int'l. Conference on High Energy Physics, (1968) 23, Ed. J. Prentki and J. Steinberger.

[11] J. D. Bjorken and E. A. Paschos, *Inelastic Electron-Proton and γ-Proton Scattering and the Structure of the Nucleon*, Phys. Rev. 185 (1969) 1975.

[12] C.G. Callan and D.J. Gross, *High Energy Electroproduction and the Constitution of the Electric Current*, Phys. Rev. Lett. 22, (1969) 156.

[13] Y. L. Dokshitzer, JETP 73 (1971) 1216.
Gribov, V. N. and Lipatov, L. N., *Deep Inelastic Scattering in Perturbation Theory*, Sov. J. Nucl. Phys. 15 (1972) 78.
Altarelli, G. and Parisi, G., *Asymptotic Freedom in Parton Language*, Nucl. Phys. B 216 (1977) 298.

[14] B. Badelek et. al., *Small x Physics in Deep Inelastic Lepton-Hadron Scattering*, Rev. Mod. Phys. 64 (1992) 927.

[15] L. V. Gribov, E. M. Levin, M. G. Ryskin, *Semihard Processes in QCD*, Phys. Rep. 100 (1983)1.

[16] A.H. Mueller, *Parton Distributions at very Small x-values*, Nucl. Phys. B (Proc. Suppl.) 18 C (1990) 125.

[17] Y. Balitskij and L.N. Lipatov, *The Pomeranchuk Singularity in Quantum Chromodynamics*, Sov. J. Nucl. Phys. 28 (1978) 822.
E. Kuraev, L.N. Lipatov and V.S. Fadin, *Multiregge Processes in the Yang-Mills Theory*, Sov. Phys. JETP 44 (1976) 443.

[18] J. Bartels, *Structure Functions at Small x: New Physics at HERA*, Particle World, Vol. 2, 2 (1991) 46.
A.D. Martin, *Structure Functions and Small x Physics*, DTP 93-66 (1993).

[19] A.J. Askew et. al., *QCD Predictions for Deep Inelastic Structure Functions at HERA*, Phys. Rev. D 47 (1993) 3775.

[20] E. M. Levin and M. G. Ryskin, *Low x Structure Function and Saturation of the Parton Density*, Nucl. Phys. B (Proc. Suppl.) 18 C (1990) 92.

[21] A. D. Martin, R. G. Roberts and W. J. Stirling, *Parton Distributions Updated*, Phys. Lett. B 306 (1993) 145.

[22] NMC Collaboration: P. Amaudruz et. al, *Proton and Deuteron F_2 Structure Functions in Deep Inelastic Muon Scattering*, Phys. Lett. B 295 (1992) 159.

[23] CCFR Collaboration: Structure Function and QCD Results from the CCFR Experiment at the Fermilab Tevatron, presented at Recontres de Physique de la Vallee d'Aoste, La Thuile, March 1992.

[24] BCDMS Collaboration: A. C. Buenvenuti et. al., *A High Statistics Measurement of the Deuteron Structure Functions $F_2(x,Q^2)$ and R from Deep Inelastic Scattering at High Q^2*, Phys. Lett. B 237 (1990) 592.

[25] WA70 Collaboration: M. Bonesini et. al., *Production of High Transverse Prompt Photons And Neutral Pions in Proton-Proton Interactions at 280 GeV/c*, Z. Phys. C 38 (1988) 371.

[26] E605 Collaboration: C. N. Brown et. al., Phys. Rev. Lett. 63 (1989) 2637.

[27] NMC Collaboration: P. Amaudruz et. al., *Gottfried Sum from the Ratio of F_2^n/F_2^p*, Phys. Rev. Lett. 66 (1991) 2712.

[28] A.D. Martin R. G. Roberts and W. J.Stirling, *Present Status of Parton Distributions*, RAL 93-027 (1993).

[29] CCFR Collaboration: C. Foudas et. al., *Neutrino Production of Opposite-Sign Dimuons at Fermilab Tevatron Energies*, Phys. Rev. Lett. 64 (1990) 1207.

[30] CTEQ Collaboration: J. Botts et. al., *CTEQ Parton Distributions and Flavor Dependence of Sea Quarks*, Phys. Lett. B 304 (1993) 159.

[31] H1 Collaboration: I. Abt et. al., *Measurement of the Proton Structure Function $F_2(x,Q^2)$ in the Low x Region at HERA*, Nucl. Phys. B 407 (1993) 515.

[32] ZEUS Collaboration: M. Derrick et al., *Measurement of the Proton Structure Function F_2 in ep Scattering at HERA*, Phys. Lett. B 316 (1993) 412.

[33] M. Glück, E. Reya, and A. Vogt, *Radiatively Generated Parton Distributions for High Energy Collisions*, Z. Phys. C 48 (1990) 471.

[34] J. Kwiecinski, A.D. Martin, R. Roberts and W. J. Stirling, *Parton Distributions at Small x*, Phys. Rev. D 42 (1990) 3645.

[35] M. Glück, E. Reya, and A. Vogt, *Parton Distributions for High Energy Collisions*, Z. Phys. C 53 (1992) 127.

[36] M. Glück, E. Reya, and A. Vogt, *Comparing Radiatively Generated Parton Distributions with Recent Measurements of $F_2(x,Q^2)$ in the Small x Region*, Phys. Lett. B 306 (1993) 391.

[37] G. Wolf, DESY 86-089 (1986).
B.H. Wiik, *HERA Status*, Proc. of the Workshop on Physics at HERA Vol. 1 (1991) 1, Ed. W. Buchmüller and G. Ingelman.

[38] ZEUS Collaboration, *The Design and Implementation of the ZEUS Central Tracking Detector*, OUNP-93-16 (1993).

[39] R. Brinkmann, *Chromatic Corrections and Dynamic Aperture in the HERA Electron Ring*, DESY HERA 87-037 (1987).

[40] T. Ferbel, *Experimental Techniques in High Energy Physics*, (Addison-Wesley Publishing Company, 1987).

[41] W. Lohmann, R. Kopp, R. Voss, *Energy Loss of Muons in the Energy Range 1-10000 GeV*, CERN 85-54 (1985).

[42] Particle Data Group, *Review of Particle Properties*, Phys. Rev. D 45 (1992).

[43] J. Krüger, *The Uranium Scintillator Calorimeter for the ZEUS Detector at the Electron-Proton Collider HERA*, DESY F35-92-02 (1992).

[44] ZEUS Collaboration, *The ZEUS Detector, Status Report*, (1989).

[45] A. Andersen et al., *Construction and Beam Tests of the ZEUS Forward and Rear Calorimeter*, Nucl. Inst. and Meth. A 309 (1991) 101.
A. Bernstein et al., *Beam Tests of the ZEUS Barrel Calorimeter*, Nucl. Inst. and Meth. A 336 (1993) 23.

[46] A description of the ZEUS calorimeter readout is given in
A. Caldwell et. al, *Design and Implementation of a High Precision Readout System for the ZEUS Calorimeter*, Nucl. Inst. and Meth. A 321 (1992) 356.

[47] F. Chlebana, *First Measurement of the Proton Structure Function F_2 With the ZEUS Detector*, Ph. D. Thesis (1994).

[48] J. Morfin, W. Tung, *Parton Distributions from a Global QCD Analysis of Deep Inelastic Scattering and Lepton Pair Production*, Z Phys. C 52 (1991) 13.

[49] A. Kwiatkowski, H. Spiesberger and H. J. Möhring, *HERACLES 4.1*, Proc. of the Workshop on Physics at HERA Vol. 3 (1991) 1294, Ed. W. Buchmüller and G. Ingelman.

[50] L. Lönnblad, *ARIADNE 3.1*, Comput. Phys. Commun. 71 (1992) 15.

[51] B. Andersson et. al., *Coherence Effects in Deep Inelastic Scattering*, Z. Phys. C 43 (1989) 625.

[52] T. Sjöstrand, Comput. Phys. Commun. 39 (1986) 347.
T. Sjöstrand and M. Bengtsson, Comput. Phys. Commun. 43 (1987) 367.

[53] B. Anderson et al, *Parton Fragmentation and String Dynamics*, Phys. Rep. 97 (1983) 31.

[54] R. Brun et. al, *GEANT 3.13*, CERN DD/EE/84-1 (1987).

[55] H.U. Bengtsson and T. Sjöstrand, *PYTHIA 5.6*, Comput. Phys. Commun. 46 (1987) 43.
T. Sjöstrand, *PYTHIA 5.6*, Proc. of the Workshop on Physics at HERA Vol. 3 (1991) 1294, Ed. W. Buchmüller and G. Ingelman.

[56] H. Abramowicz et. al., *A Parametrization of $\sigma T(\gamma^* p)$ above the Resonance Region for Q2 0*, Phys. Lett. B 269 (1991) 465.

[57] ZEUS Collaboration: M. Derrick et al., *A Measurement of $\sigma_{tot}(\gamma p)$ at $\sqrt{s} = 210$ GeV*, Phys. Lett. B 293 (1992) 465.

[58] F. Jacquet and A. Blondel, Proc. of the Study for an ep Facility for Europe (1979) 393, Ed. U. Amaldi.

[59] K. C. Hoeger, *Measurement of x, y, Q^2 in Neutral Current Events*, Proc. of the Workshop on Physics at HERA Vol. 1 (1991) 45, Ed. W. Buchmüller and G. Ingelman.

[60] S. Bentvelsen, J. Engelen, and P. Kooijman, *Reconstruction of (x,Q^2) and Extraction of Structure Functions in Neutral Current Scattering at HERA*, Proc. of the Workshop on Physics at HERA Vol. 1 (1991) 23, Ed. W. Buchmüller and G. Ingelman.

[61] H. Abramowicz et. al., *A Determination of F_2 with the 1992 Data*, ZEUS-Note 93-078 (1993).

[62] M. Roco, *Corrections to Hadronic Variables*, ZEUS-Note 93-064.

[63] H. Bethe and W. Heitler, *On the Stopping of Fast Particles and on the Creation of Positive Electrons*, Proc. Roy. Soc. A 146 (1934) 83.

[64] J. Andruszkow et. al., *First Measurement of HERA luminosity by ZEUS LUMI Monitor*, DESY 92-066 (1992).

[65] J. Crittenden et. al., *Results of the Analysis of the C5 Detector Time Distributions for the Fall 1992 Running Period*, ZEUS-Note 93-041 (1993).

[66] G. Marchesini et al., *HERWIG:5.6*, Comp. Phys. Comm. 67 (1992) 465.

[67] ZEUS Collaboration: M. Derrick et al., *Observation of Events with a Large Rapidity Gap in Deep Inelastic Scattering at HERA*, Phys. Lett. B 315 (1993) 481.

[68] R.G. Roberts, *The Structure of the Proton*, Cambridge University Press (1990)

[69] A.M. Cooper-Sarkar et. al., *Measurement of the Longitudinal Structure Function and the Small x Gluon Density of the Proton*, Z. Phys. C 39 (1988) 281.

[70] G. Altarelli and G. Martinelli, *Transverse Momentum of Jets in Electroproduction from Quantum Chromodynamics*, Phys. Lett. B 76 (1978) 89.

[71] K. Charchula, *The Package PAKPDF1.1 of Parametrizations of Parton Distributions in the Proton*, Comp. Phys. Comm. 69 (1992) 360.

[72] L. Mo and Y.S. Tsai, *Radiative Corrections to Inelastic ep and μp Scattering*, Rev. Mod. Phys. 41 (1969) 205.

[73] M. Consoli et. al., DESY HERA 80-01

[74] D. Yu Bardin et. al., *Electroweak Radiative Corrections to Deep Inelastic Scattering at HERA*, Z. Phys. C 42 (1989) 679.

[75] M. Böhm and H. Spiesberger, *Radiative Corrections to Neutral Current Deep Inelastic Lepton Nucleon Scattering at HERA Energies*, Nucl. Phys. B 294 (1987) 749.

[76] H. Spiesberger et. al., *Radiative Corrections at HERA*, Proc. of the Workshop on Physics at HERA Vol. 2 (1991) 798, Ed. W. Buchmüller and G. Ingelman.

[77] A. Akhundov et. al., *TERAD91*, Proc. of the Workshop on Physics at HERA Vol. 3 (1991) 1285, Ed. W. Buchmüller and G. Ingelman.

[78] J. Blümlein, *HELIOS*, Proc. of the Workshop on Physics at HERA Vol. 3 (1991) 1270, Ed. W. Buchmüller and G. Ingelman.

[79] The unfolding method was proposed by Dr. Halina Abramowicz.

[80] H. Jung, G. Schuler, J. Terron, *J/ψ Production Mechanisms and Determination of the Gluon Density at HERA*, Int. J. Mod. Phys. A 7 (1992) 7955.

[81] K. Prytz, *Approximate determination of the gluon density at low-x from the F_2 Scaling Violations*, Phys. Lett. B 311 (1993) 286.

[82] M. Roco, *A Measurement of the Gluon Distribution at Low x using $F_{2(x,Q2)}$ Scaling Violations*, ZEUS-Note 93-088.
Preliminary results for the first measurement of the gluon distribution at HERA using the ZEUS detector was presented at the 1993 Int'l. Lepton Photon Conference at Cornell.

[83] ZEUS Collaboration: M. Derrick et al., *Hadronic Energy Distributions in Deep Inelastic Electron-Proton Scattering*, Z. Phys. C 59 (1993) 231.